

DETECTION OF MANUFACTURING ERRORS IN COMPOSITE PRESSURE  
VESSEL STRUCTURES

A THESIS SUBMITTED TO  
THE GRADUATE SCHOOL OF NATURAL AND APPLIED SCIENCES  
OF  
MIDDLE EAST TECHNICAL UNIVERSITY

BY

CİHAN TALEBİ

IN PARTIAL FULFILLMENT OF THE REQUIREMENTS  
FOR  
THE DEGREE OF MASTER OF SCIENCE  
IN  
MECHANICAL ENGINEERING

SEPTEMBER 2022



Approval of the thesis:

**DETECTION OF MANUFACTURING ERRORS IN COMPOSITE  
PRESSURE VESSEL STRUCTURES**

submitted by **CİHAN TALEBİ** in partial fulfillment of the requirements for the degree of **Master of Science in Mechanical Engineering, Middle East Technical University** by,

Prof. Dr. Halil Kalıpçılar  
Dean, Graduate School of **Natural and Applied Sciences**

Prof. Dr. Sahir Arıkan  
Head of the Department, **Mechanical Engineering**

Assist. Prof. Dr. Gökhan Özgen  
Supervisor, **Mechanical Engineering, METU**

**Examining Committee Members:**

Prof. Dr. Fevzi Suat Kadioğlu  
Mechanical Engineering, METU

Assist. Prof. Dr. Gökhan Osman Özgen  
Mechanical Engineering, METU

Assist. Prof. Dr. Orkun Özşahin  
Mechanical Engineering, METU

Assoc. Prof. Dr. Melin Şahin  
Aerospace Engineering, METU

Assoc. Prof. Dr. Bülent Özkan  
Mechanical Engineering, Gazi University

Date: 01.09.2022

**I hereby declare that all information in this document has been obtained and presented in accordance with academic rules and ethical conduct. I also declare that, as required by these rules and conduct, I have fully cited and referenced all material and results that are not original to this work.**

Name Last name: Cihan Talebi

Signature:

## **ABSTRACT**

### **DETECTION OF MANUFACTURING ERRORS IN COMPOSITE PRESSURE VESSEL STRUCTURES**

Talebi, Cihan  
Master of Science, Mechanical Engineering  
Supervisor: Assist. Prof. Dr. Gökhan Osman Özgen

September 2022, 164 pages

Usage of composite materials in engineering structures has been increasing for the past few decades, which required an increase in complexity and delicacy in the manufacturing techniques. Unlike their metal counterparts, composite structures require a vast and thorough testing process to ensure the performance of the product. Any error in the manufacturing process will affect the quality of the produced composite part, which in return may not satisfy the required performance of the design. Therefore, it is required for composite parts to contain as little error as possible, both in types, number, and extent.

In this study, most commonly encountered error types for filament wound composite structures: ply orientation mix-ups, alteration in volume fraction, and delamination are considered and assessed. Each error type was considered for plate, cylindrical, and pressure vessel structures. Non-destructive evaluation methods based on principals of dynamics and vibration are either proposed or employed. Proposed or employed methods were validated through finite element analysis and modal test data.

A novel method was proposed to assess the ply orientation mix-ups. This method uses the experimentally measured natural frequencies, and then converts them into a range of parameters that will be used to identify ply orientations later. An optimization based on the physicality of the manufacturing process is then used to reduce this range into a single quantity. This quantity is then employed with an artificial neural network to assess the ply orientations in the laminate. To validate the model, several finite element analysis and modal tests were conducted that include the effects of total plies, geometry, size, and boundary condition.

Previously proposed novel method described in the previous paragraph was extended to cover the effects of volume fraction and average thickness of the laminate on stiffness and mass characteristics of the structure. By including these effects, the method was weakened and was shown that it may no longer obtain the ply orientations. The proposed method for this effect instead finds pseudo-orientations, which cannot be employed in aid to find the ply orientations anymore. However, it was shown that after the volume fraction was detected, an additional step may be used to obtain the real ply orientations. This method was also validated through both finite element analysis and modal test data.

Previously in literature, a method of added mass to the delaminations was used to identify them on beam structures. This method was extended and applied to plates, cylinders, and pressure vessels. It was identified that the employed method presents a large difference in natural frequencies for all structures considered when the mass is applied on a delamination region and does not provide a meaningful change if the mass is applied elsewhere, compared to a structure that is free of delamination. The employed method was validated both through finite element analysis and modal tests. It was shown that the finite element analysis overestimates the difference obtained in natural frequencies compared to tests.

Keywords: Composite structures, non-destructive evaluation, manufacturing errors, delamination

## ÖZ

### KOMPOZİT BASINÇLI KAP YAPILARINDA ÜRETİM HATALARININ TESPİTİ

Talebi, Cihan  
Yüksek Lisans, Makina Mühendisliği  
Tez Yöneticisi: Dr. Öğr. Üyesi Gökhan Osman Özgen

Eylül 2022, 164 sayfa

Kompozit malzemelerin mühendislik yapılarında kullanımını son birkaç yılda artmakta olup bu nedenle imalat tekniklerinde karmaşıklık ve incelikte bir artış gerektirmiştir. Metal muadillerinden farklı olarak kompozit yapılar, ürünün performansını sağlamak için geniş ve kapsamlı bir test süreci gerektirir. Bu nedenle, ürünün çok az hata içermesi temeldir.

Bu çalışmada, filaman sargılı kompozit yapılar için en sık karşılaşılan hata türleri: katman açmaları karışıklıkları, hacim oranındaki değişiklik ve delaminasyon ele alınmakta ve değerlendirilmektedir. Plaka, silindirik ve basınçlı kap yapıları için her bir hata türü incelenmiştir. Dinamik ve titreşim ilkelerine dayalı tahribatsız değerlendirme yöntemleri ya önerilmiş ya da kullanılmaktadır. Önerilen veya kullanılan yöntemler, sonlu elemanlar analizi ve modal test verileri aracılığıyla doğrulanmıştır.

Katman açmaları karışıklıklarını değerlendirmek için yeni bir yöntem önerildi. Bu yöntem deneysel olarak ölçülen doğal frekansları kullanmakta ve daha sonra bunları katman açmalarını tanımlamak için kullanılacak bir dizi parametreye dönüştürmektedir. Daha sonra bu parameter aralığını tek bir parametreye indirmek



için üretim sürecinin fizikselliğine dayalı bir optimizasyon kullanılmaktadır. Bu parametre daha sonra kompozitteki katman açılarını değerlendirmek için bir yapay sinir ağı ile kullanılmıştır. Önerilen yöntemi doğrulamak için toplam katmanların, geometrinin, boyutun ve sınır koşulunun etkilerini içeren sonlu eleman analizleri ve modal testleri yapılmıştır. Tüm durumlar için, ele alınan durumlar ile önerilen yöntemin tahmininde çok iyi bir eşleşme elde edilmiştir.

Daha önce önerilen yeni yöntem kompozitin hacim oranı ve ortalama kalınlığının etkilerini kapsayacak şekilde genişletilmiştir. Bu etkiler dahil edilerek, yöntem zayıflatılmış ve artık katman açılarını elde edemeyebileceği gösterilmiştir. Önerilen yöntem, bunun yerine değerli bir bilgi içermeyen sahte katman açılarını bulmaktadır. Bununla birlikte, hacim oranı saptandıktan sonra, gerçek katman açılarını elde etmek için ek bir adımın kullanılabileceği gösterilmiştir. Önerilen bu yöntem aynı zamanda hem sonlu elemanlar analizi hem de modal test verileri ile doğrulanmıştır.

Literatürde daha önce, kiriş yapılarında delaminasyonlara kütle ekleme yöntemi kullanılıyordu. Bu yöntem genişletildi; plakalara, silindirlere ve basınçlı kaplara uygulandı. Kullanılan yöntem için, kütle için bir delaminasyon bölgesine uygulandığında dikkate alınan tüm yapılar için doğal frekansları abarttığı ve kütle delaminasyon dışı bir bölgeye uygulandığında anlamlı bir değişiklik sağlamadığı tespit edilmiştir. Kullanılan yöntem hem sonlu elemanlar analizleri hem de modal testler yoluyla doğrulanmıştır. Sonlu elemanlar analizinin, testlere kıyasla doğal frekanslarda elde edilen farkı abarttığı gösterilmiştir.

Anahtar Kelimeler: Kompozit yapılar, tahribatsız muayene, üretim hataları, delaminasyon

To the pioneers of tomorrow

## ACKNOWLEDGMENTS

The author wishes to express their appreciation and gratitude towards their supervisor, Prof. Dr. Gökhan Özgen for their advice and guidance through this research.

The author proposes their sincerest thankfulness to Ali Yetgin and Emre Özaslan for their encouragement, advice, and insight throughout this work.

The author would like to express their thanks to Kıvanç Yurdakul, Begüm Beril İncecik, Gökberk Demirok, and Nusret Cem Diyarbakır for their stellar work on production of the test specimens employed in this research.

The author wishes to thank Bülent Acar for proposing the problems encountered in manufacturing of composite structures that were assessed in this work.

Encouragement, support, and reassurance of the author's family and friends were deeply appreciated. Without them, this thesis could not be completed.

The author wishes thanks to Roketsan Inc. which funded the experimental part of this research.

The author wishes thanks to the jury of this thesis for their valuable comments and feedback.

## TABLE OF CONTENTS

ABSTRACT .....	v
ÖZ.....	viii
ACKNOWLEDGMENTS .....	xi
TABLE OF CONTENTS .....	xii
LIST OF TABLES .....	xvii
LIST OF FIGURES .....	xxiii
CHAPTERS	
1 INTRODUCTION.....	1
1.1 Objective of the Thesis .....	2
1.1.1 Errors in Ply Stacking Configuration .....	3
1.1.2 Errors in Thickness & Volume Fraction .....	4
1.1.3 Delamination Errors .....	5
1.2 Thesis Overview .....	6
2 LITERATURE REVIEW .....	9
2.1 Methods Using Principles of Vibrations & Dynamics .....	10
2.1.1 Frequency Change .....	12
2.1.2 Mode Shape .....	14
2.1.3 Curvature Change .....	15
2.1.4 Flexibility Change .....	15
2.1.5 Frequency Response Function.....	16
2.1.6 Modal Strain Energy.....	17
2.2 Methods Using Principles of Acoustics.....	18

2.2.1	Acoustic Emission .....	18
2.2.2	Ultrasound.....	18
2.2.3	Lamb Waves .....	19
2.3	Methods Using Principles of Optics & Radiation.....	20
2.3.1	Thermal Imaging.....	20
2.3.2	X-Ray.....	21
2.3.3	Microwave .....	22
2.3.4	Shearography .....	22
2.4	Computed Tomography.....	22
2.5	Neural Networks .....	24
2.6	Electrical Properties .....	25
2.7	Discussion of Information Present in Literature .....	26
3	IDENTIFICATION OF PLY LAYUP CONFIGURATION.....	29
3.1	Mechanics of Composite Materials.....	30
3.2	Proposed Method for Identification of Ply Layup Configuration Errors .	34
3.2.1	Obtaining Laminate Property Range from Test Data .....	36
3.2.2	Optimization of Laminate Properties.....	39
3.2.3	Optimization of Ply Properties.....	42
3.3	Numerical Simulation Based Validation of Ply Layup Identification Method.....	46
3.3.1	Numerical Simulation Based Validation for Plate Structures.....	47
3.3.2	Numerical Simulation Based Validation for Cylindrical Structures.	54
3.3.3	Numerical Simulation Based Validation for Pressure Vessel Structures.....	58

3.4	Experiment Based Validation of Ply Layup Identification Method .....	65
3.4.1	Experiment Based Validation for Plate Structures .....	67
3.4.2	Experiment Based Validation for Cylindrical Structures .....	70
3.4.3	Experiment Based Validation for Pressure Vessel Structures.....	71
3.5	Evaluation of the Performance of Proposed Method for Ply Layup Identification.....	73
4	IDENTIFICATION OF AVERAGE THICKNESS AND VOLUME FRACTION .....	75
4.1	Micromechanical Models for Composite Structures .....	76
4.2	Proposed Method for Identification of Average Thickness and Volume Fraction.....	78
4.2.1	Updated Optimization of Laminate Properties .....	80
4.2.2	Updated Optimization of Ply Properties.....	81
4.3	Numerical Simulation Based Validation for Identification of Average Thickness and Volume Fraction.....	82
4.3.1	Numerical Simulation Based Validation for Plate Structures .....	82
4.3.2	Numerical Simulation Based Validation for Cylindrical Structures .	87
4.3.3	Numerical Simulation Based Validation for Pressure Vessel Structures.....	91
4.4	Experiment Based Validation for Identification of Average Thickness and Volume Fraction.....	96
4.4.1	Experiment Based Validation for Plate Structures .....	96
4.4.2	Experiment Based Validation for Cylindrical Structures .....	98
4.4.3	Experiment Based Validation for Pressure Vessel Structures.....	100

4.5	Evaluation of the Performance of Proposed Method for Average Thickness and Volume Fraction .....	101
5	IDENTIFICATION OF DELAMINATION.....	103
5.1	Employed Method for Identification of Delamination.....	104
5.2	Simulation Based Validation for Delamination Identification.....	106
5.2.1	Numerical Simulation Based Validation of Plate Structures .....	108
5.2.2	Numerical Simulation Based Validation of Cylindrical Structures	113
5.2.3	Numerical Simulation Based Validation of Pressure Vessel Structures.....	116
5.3	Experiment Based Validation for Delamination Identification.....	117
5.3.1	Experiment Based Validation of Plate Structures.....	119
5.3.2	Experiment Based Validation of Cylindrical Structures.....	121
5.3.3	Experiment Based Validation of Pressure Vessel Structures .....	123
5.4	Evaluation of the Performance of Employed Method for Identification of Delamination.....	124
6	CONCLUSION.....	127
6.1	Concluding Remarks .....	128
6.2	Future Work .....	131
	REFERENCES .....	133
	APPENDICES	
A.	Obtaining Natural Frequencies for Composite Structures .....	143
A.1	Analytical Modelling.....	143
A.2	Continuous System Modelling .....	144
A.2.1	Continuous System Modelling of Plates.....	145
A.2.2	Continuous System Modelling of Cylinders.....	147

A.3	Numerical Modelling .....	151
B.	Numerical Validation Results for Identification of Ply Layup Configuration.....	153
B.1	Numerical Validation Results for Plate Structures .....	153
B.2	Numerical Validation Results for Pressure Vessel Structures .....	159
C.	Experimentally Obtained FRFs Through Impact Hammer Modal Tests	160
D.	Numerical Validation Results for Identification of Thickness & Volume Fraction for Plate Structures .....	162



## LIST OF TABLES

### TABLES

Table 2.1 Methods found in literature used in defect and error assessment .....	9
Table 3.1 Considered configurations for plate geometry.....	47
Table 3.2 Material properties for the considered carbon epoxy composite system	49
Table 3.3 Ply orientations obtained through the optimization process with consequently reduced search range ANN for P_C1_S1_B1 case.....	53
Table 3.4 Results of the optimization runs for ply orientation identification for P_C1_S1_B1 case.....	53
Table 3.5 Considered configurations for cylindrical geometry .....	54
Table 3.6 Ply orientations obtained through the optimization process with consequently reduced search range ANN for C_C10_S3_B1 case .....	58
Table 3.7 Results of the optimization runs for ply orientation identification for all cylindrical geometry cases considered.....	58
Table 3.8 Considered configurations for pressure vessel geometry .....	60
Table 3.9 Ply orientations obtained through the optimization process with consequently reduced search range ANN for PV_C12_S4_B2 case.....	64
Table 3.10 Results of the optimization runs for ply orientation identification for PV_C12_S4_B2 case .....	65
Table 3.11 Considered cases for the experimental validation of the method for plate geometries .....	67
Table 3.12 Experimentally obtained natural frequencies for the considered plate geometries .....	68
Table 3.13 Results of the optimization runs for ply orientation identification for P_C2_S2_B2 case employing experimentally obtained natural frequencies .....	69
Table 3.14 Results of the optimization runs for ply orientation identification for P_C7_S2_B2 case employing experimentally obtained natural frequencies .....	69
Table 3.15 Results of the optimization runs for ply orientation identification for P_C8_S2_B2 case employing experimentally obtained natural frequencies .....	69

Table 3.16 Results of the optimization runs for ply orientation identification for P_C9_S2_B2 case employing experimentally obtained natural frequencies .....	69
Table 3.17 Considered cases for the experimental validation of the method for cylindrical geometries .....	70
Table 3.18 Experimentally obtained natural frequencies for the considered cylindrical geometries .....	71
Table 3.19 Results of the optimization runs for ply orientation identification for cylindrical geometry cases employing experimentally obtained natural frequencies .....	71
Table 3.20 Considered case for the experimental validation of the method for pressure vessel geometries .....	71
Table 3.21 Experimentally obtained natural frequencies for the considered pressure vessel geometries.....	72
Table 3.22 Results of the optimization runs for ply orientation identification for pressure vessel geometry cases employing experimentally obtained natural frequencies.....	72
Table 4.1 Mechanical properties of the composite material at different volume fractions .....	78
Table 4.2 Considered configurations for numerical simulation based validation of composite plate type structures .....	83
Table 4.3 Pseudo-orientations and volume fractions obtained through the optimization process with consequently reduced search range ANN for P_C1_V40 .....	86
Table 4.4 Pseudo-orientations, volume fraction, and laminate thickness results of the optimization runs for P_C1_V40.....	86
Table 4.5 Pseudo-orientations and final ply orientations obtained for each optimization run for P_C1_V40 .....	87
Table 4.6 Considered configurations for numerical simulation based validation of composite cylindrical type structures .....	87

Table 4.7 Pseudo-orientations and volume fractions obtained through the optimization process with consequently reduced search range ANN for C_C10_V40 .....	90
Table 4.8 Pseudo-orientations and final ply orientations obtained for each optimization run for C_C10_V40 .....	91
Table 4.9 Pseudo-orientations and final ply orientations obtained for each optimization run for C_C11_V70 .....	91
Table 4.10 Considered configurations for pressure vessel geometry .....	92
Table 4.11 Pseudo-orientations and volume fractions obtained through the optimization process with consequently reduced search range ANN for PV_C12_V70.....	95
Table 4.12 Pseudo-orientations and final ply orientations obtained for each optimization run for PV_C12_V70.....	95
Table 4.13 Pseudo-orientations and final ply orientations obtained for each optimization run for PV_C13_V40.....	96
Table 4.14 Considered cases for the experimental validation of the method for plate geometries .....	97
Table 4.15 Experimentally obtained natural frequencies for the considered plate geometries .....	97
Table 4.16 Results of the optimization runs for ply orientation identification for P_C2_V70 case employing experimentally obtained natural frequencies.....	98
Table 4.17 Results of the optimization runs for ply orientation identification for P_C2_S2_B2 case employing experimentally obtained natural frequencies .....	98
Table 4.18 Considered cases for the experimental validation of the method for cylindrical geometries .....	98
Table 4.19 Experimentally obtained natural frequencies for the considered cylindrical geometries .....	99
Table 4.20 Results of the optimization runs for ply orientation identification for C_C11_V70 case employing experimentally obtained natural frequencies .....	99

Table 4.21 Results of the optimization runs for ply orientation identification for C_C11_S4_B2 case employing experimentally obtained natural frequencies.....	100
Table 4.22 Considered cases for the experimental validation of the method for pressure vessel geometries .....	100
Table 4.23 Experimentally obtained natural frequencies for the considered pressure vessel geometries.....	100
Table 4.24 Results of the optimization runs for ply orientation identification for PV_C13_V40 case employing experimentally obtained natural frequencies .....	101
Table 4.25 Results of the optimization runs for ply orientation identification for PV_C14_S4_B2 case employing experimentally obtained natural frequencies ...	101
Table 5.1 Considered cases for the validation of plate geometries .....	108
Table 5.2 Natural frequencies of P_D2 case compared to P_D1. ....	110
Table 5.3 Natural frequencies of P_D3 case compared to P_D1. ....	110
Table 5.4 Natural frequencies of P_D4 case compared to P_D1, with added mass on delamination .....	111
Table 5.5 Natural frequencies of P_D4 case compared to P_D1, with added mass at the opposite side of the delamination .....	111
Table 5.6 Natural frequencies of P_D5 case compared to P_D1 .....	112
Table 5.7 Considered cases for the validation of cylindrical geometries.....	113
Table 5.8 Natural frequencies of C_D2 case compared to C_D1 .....	114
Table 5.9 Natural frequencies of C_D3 case compared to C_D1 .....	115
Table 5.10 Natural frequencies of C_D3 case compared to C_D1, with a larger added mass of size 100mm x 20mm x 20mm .....	115
Table 5.11 Considered cases for the validation of pressure vessel geometries.....	116
Table 5.12 Natural frequencies of PV_D2 case compared to PV_D1 .....	117
Table 5.13 Experimentally obtained natural frequencies for P_D2 and P_D1 .....	119
Table 5.14 Experimentally obtained natural frequencies for P_D4 and P_D1 .....	120
Table 5.15 Experimentally obtained natural frequencies for P_D5 and P_D1 .....	120
Table 5.16 Experimentally obtained natural frequencies for P_D4 and P_D1 with added mass on the opposite side of the plate.....	121

Table 5.17 Experimentally obtained natural frequencies for C_D3 and C_D1 ....	123
Table 5.18 Experimentally obtained natural frequencies for C_D3 and C_D1 with two steel masses added .....	123
Table 5.19 Experimentally obtained natural frequencies for PV_D2 and PV_D1	124
Table B.1 Results of the optimization runs for ply orientation identification for P_C1_S2_B1 case .....	153
Table B.2 Results of the optimization runs for ply orientation identification for P_C1_S1_B2 case .....	154
Table B.3 Results of the optimization runs for ply orientation identification for P_C2_S1_B1 case .....	154
Table B.4 Results of the optimization runs for ply orientation identification for P_C3_S1_B1 case .....	155
Table B.5 Results of the optimization runs for ply orientation identification for P_C4_S1_B1 case .....	155
Table B.6 Results of the optimization runs for ply orientation identification for P_C5_S1_B1 case .....	156
Table B.7 Results of the optimization runs for ply orientation identification for P_C6_S1_B1 case .....	156
Table B.8 Results of the optimization runs for ply orientation identification for P_C2_S2_B2 case .....	157
Table B.9 Results of the optimization runs for ply orientation identification for P_C7_S2_B2 case .....	157
Table B.10 Results of the optimization runs for ply orientation identification for P_C8_S2_B2 case .....	158
Table B.11 Results of the optimization runs for ply orientation identification for P_C9_S2_B2 case .....	158
Table B.12 Results of the optimization runs for ply orientation identification for PV_C13_S4_B2 case .....	159
Table B.13 Results of the optimization runs for ply orientation identification for PV_C14_S4_B2 case .....	159

Table D.1 Pseudo-orientations, volume fraction, and laminate thickness results of the optimization runs for P_C2_V60.....	162
Table D.2 Pseudo-orientations, volume fraction, and laminate thickness results of the optimization runs for P_C3_V40.....	162
Table D.3 Pseudo-orientations, volume fraction, and laminate thickness results of the optimization runs for P_C4_V70.....	163
Table D.4 Pseudo-orientations, volume fraction, and laminate thickness results of the optimization runs for P_C5_V55.....	163
Table D.5 Pseudo-orientations, volume fraction, and laminate thickness results of the optimization runs for P_C6_V50.....	164
Table D.6 Pseudo-orientations, volume fraction, and laminate thickness results of the optimization runs for P_C2_V70.....	164

## LIST OF FIGURES

### FIGURES

Figure 1.1 A general filament winding process [5]. .....	2
Figure 1.2 Possible errors in ply stacking configuration .....	3
Figure 1.3 Effect of volume fraction on the thickness of the composite .....	4
Figure 1.4 Debonded surfaces and the gap in between created by delamination .....	5
Figure 2.1 Coverage of structural health monitoring techniques on detection of defects .....	26
Figure 3.1 Alignment of a single ply compared to the global directions.....	30
Figure 3.2 Applied loads and moments on the composite laminate. For clarity of the figure, forces and moments are only shown on one side of the laminate. ....	33
Figure 3.3 Plies and their respective distances to the mid-plane of the laminate ...	34
Figure 3.4 Flowchart of the process employed to obtain the ply orientations of the unknown composite laminate .....	35
Figure 3.5 Estimated area constructed from unique data points estimated to contain all possible layup configurations.....	38
Figure 3.6 Change of $D^*$ parameters for a single ply .....	41
Figure 3.7 Optimization of ply properties by employing ANN subsequently on smaller search ranges .....	43
Figure 3.8 Finite element model and first three mode shapes for C1_S1_B1 case	50
Figure 3.9 Estimated area for $D_{11}^*$ and the boundary values for the considered first natural frequency .....	51
Figure 3.10 Estimated area for $D_{22}^*$ and the boundary values for the considered first natural frequency .....	51
Figure 3.11 Estimated area for $0.5D_{12}^* + D_{66}^*$ and the boundary values for the considered first natural frequency .....	52
Figure 3.12 Optimization of $D^*$ parameters given maximum and minimum values .....	52

Figure 3.13 Finite element model and first three mode shapes of C_C10_S3_B1 case .....	55
Figure 3.14 Estimated area for $D_{11}$ * and the boundary values for the considered first natural frequency.....	56
Figure 3.15 Estimated area for $D_{22}$ * and the boundary values for the considered first natural frequency.....	56
Figure 3.16 Estimated area for $0.5D_{12}$ * + $D_{66}$ * and the boundary values for the considered first natural frequency .....	57
Figure 3.17 Optimization of $D$ * parameters given maximum and minimum values .....	57
Figure 3.18 Considered pressure vessel geometry for numerical simulation based validation of the proposed method [76].....	60
Figure 3.19 Finite element model and first three mode shapes of PV_C12_S4_B2 case .....	61
Figure 3.20 Estimated area for $D_{11}$ * and the boundary values for the considered first natural frequency.....	62
Figure 3.21 Estimated area for $D_{22}$ * and the boundary values for the considered first natural frequency.....	63
Figure 3.22 Estimated area for $0.5D_{12}$ * + $D_{66}$ * and the boundary values for the considered first natural frequency .....	63
Figure 3.23 Optimization of $D$ * parameters given maximum and minimum values .....	64
Figure 3.24 Test configuration used for the impact hammer modal tests. ....	67
Figure 3.25 Composite plate subjected to impact hammer modal test.....	68
Figure 3.26 Composite cylinder subjected to impact hammer modal test .....	70
Figure 3.27 Composite pressure vessel manufactured that is to be subjected to impact hammer modal test.....	72
Figure 4.1 Proposed method for obtaining volume fraction and average thickness of a laminate.....	79



Figure 4.2 Increased range of $D$ * parameters due to consideration of different volume fractions.....	80
Figure 4.3 Estimated area for $D_{11}$ * and the boundary values for the considered first natural frequency .....	84
Figure 4.4 Estimated area for $D_{22}$ * and the boundary values for the considered first natural frequency .....	84
Figure 4.5 Estimated area for $0.5D_{12}$ * + $D_{66}$ * and the boundary values for the considered first natural frequency .....	85
Figure 4.6 Optimization of $D$ * parameters given maximum and minimum values	85
Figure 4.7 Estimated area for $D_{11}$ * and the boundary values for the considered first natural frequency .....	88
Figure 4.8 Estimated area for $D_{22}$ * and the boundary values for the considered first natural frequency .....	89
Figure 4.9 Estimated area for $0.5D_{12}$ * + $D_{66}$ * and the boundary values for the considered first natural frequency .....	89
Figure 4.10 Optimization of $D$ * parameters given maximum and minimum values .....	90
Figure 4.11 Estimated area for $D_{11}$ * and the boundary values for the considered first natural frequency .....	92
Figure 4.12 Estimated area for $D_{22}$ * and the boundary values for the considered first natural frequency .....	93
Figure 4.13 Estimated area for $0.5D_{12}$ * + $D_{66}$ * and the boundary values for the considered first natural frequency .....	93
Figure 4.14 Optimization of $D$ * parameters given maximum and minimum values .....	94
Figure 4.15 Composite plate subjected to impact hammer modal test .....	97
Figure 4.16 Composite cylinder subjected to impact hammer modal test.....	99
Figure 5.1 Amplification of the effects of delamination by the added mass .....	104
Figure 5.2 Finite element model of added delamination to a composite structure	107

Figure 5.3 Considered cases for the validation of employed method for plate geometries.....	108
Figure 5.4 Considered cases with different added mass locations for P_D4 .....	112
Figure 5.5 Considered cases for the validation of employed method for cylindrical geometries.....	113
Figure 5.6 Mode shapes of the considered pressure vessels with added mass.....	117
Figure 5.7 Teflon films employed to create delamination on structures.....	118
Figure 5.8 Insertion of teflon films during the filament winding process to create delamination .....	118
Figure 5.9 Ultrasonic C-scan results for a pressure vessel with various sized added delaminations [76].....	118
Figure 5.10 Attached steel mass to the structure.....	119
Figure 5.11 Attached steel mass to the cylinder.....	121
Figure 5.12 Attached steel mass to the pressure vessel.....	124
Figure A.1 Reduction of the 4 <sup>th</sup> order matrix to 2 <sup>nd</sup> order.....	147
Figure A.2 Coordinate systems used for the cylinder and general dimensions of the cylinder.....	148
Figure C.1 Point Accelerance taken from P_C2_V70, on the corner of the specimen .....	160
Figure C.2 Point Accelerance taken from C_C11_S4_B2, on the edge of the specimen .....	161

## **CHAPTER 1**

### **INTRODUCTION**

Amongst the many types of composite materials employed in the industry, long-fiber reinforced composites provide very high durability, strength to weight ratio, corrosion resistance, and improved impact properties. Due to these benefits, they are currently used in automotive, sports, aeronautical, civil, renewable energy, off-shore, and marine industries [1-4]. Usage of composite materials are widening as the manufacturing processes become more publicly available and cheaper. However, as the application ranges of composite materials are widening, usage of such materials in industry are proposing novel problems and difficulties, especially with the production of the part.

Many challenges come with the manufacturing of composite materials and due to the not yet fully understood mechanical characteristics of the material and thereafter lack of experimental data, a rigorous quality assurance process is required to assess the design is up to the performance standards. Without ensuring the produced part is free of manufacturing defects, there may occur various differences in mechanical behavior in forms of stiffness alterations, strength reduction, warping, distortions, delaminations, and much more which render the structure unusable.

As the production of composite parts are increasing in the industry and the current error assessment technologies are yielding to be either ineffective in cost or time, new methods are in demand to assess the design criteria of composite parts. In the following section, the objective of this study is presented containing information of the material, production method, and commonly encountered errors.

## 1.1 Objective of the Thesis

The objective of this thesis is to assess the most commonly encountered manufacturing errors for composite parts produced by filament winding process. It is aimed to identify the presence of these errors in various geometries from basic ones such as plates to complex ones like pressure vessels by employing a non-destructive evaluation method.

In filament winding manufacturing technology, continuous rovings of fiber are merged through a resin bath, and then the resulting wet fiber-matrix bands are wound over a rotating mandrel as shown in Figure 1.1. Later, the mandrel and composite are cured in an oven at high temperatures, causing the resin in the composite to set in. After the curing process is complete, the mandrel is removed, and the composite part is obtained. Several machining techniques may also be applied after the rough composite structure is obtained.

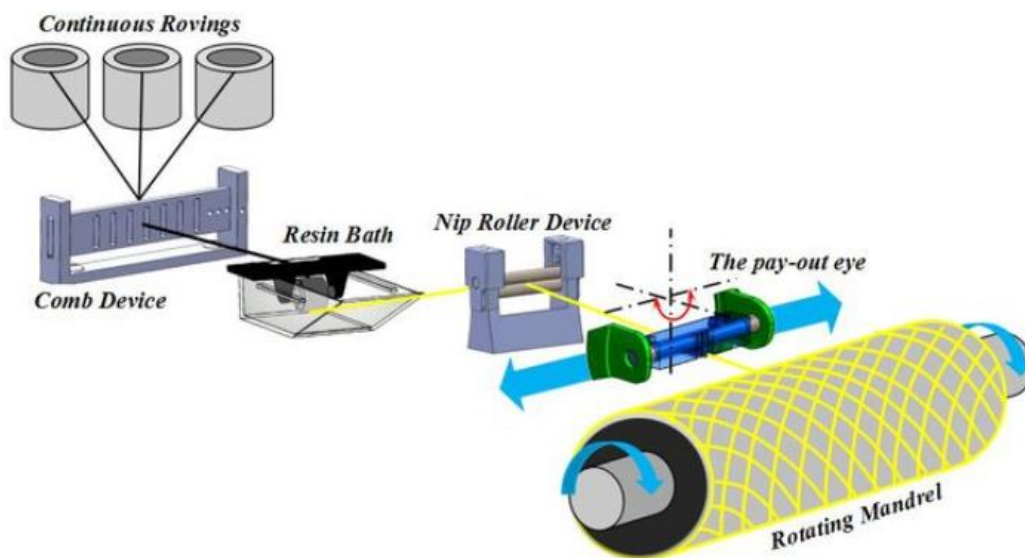


Figure 1.1 A general filament winding process [5].

Due to the nature of the filament winding process most commonly errors in ply orientations, thickness and volume fraction variances, and delamination occur. All of these mentioned errors cause an alteration in fiber and matrix distribution or

lamination. Such defects are bound to cause shift in mechanical properties. Below are some insight and explanations on how these manufacturing errors occur.

### 1.1.1 Errors in Ply Stacking Configuration

When a new ply is wound over the previous one during the filament winding process, there is no visual indicator to assess the previous plies underneath. In practice, the configuration is tracked by taking notes on which ply is wound over the mandrel. However, this process is prone to human error. Mainly, this error is encountered when there is a ply mix-up or from the slippage of fiber bands on the wet resin laid beneath it. Once the product is finished, only the innermost and outermost layers are visible as shown in Figure 1.2. Therefore, any alteration in plies that are not these visible layers cannot be readily assessed.

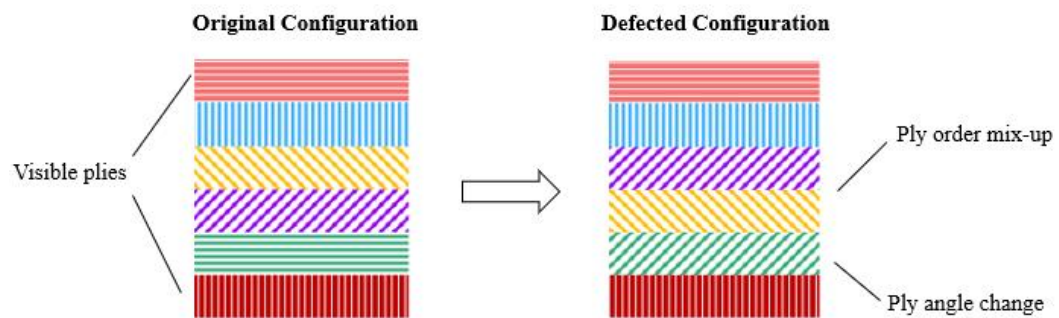


Figure 1.2 Possible errors in ply stacking configuration

Hence, the fiber orientations for individual plies in the laminate are subject to change within this manufacturing error. Commonly, the desired properties of a long-fiber reinforced composite are attributed to the fiber direction, and the secondary properties that are either unwanted or undesired arise from the other directions, commonly denoted as matrix direction. Since the properties of laminate strongly depend on the fiber orientations of plies, produced parts must ensure minimal deviation from the design standards or face severe changes in mechanical behavior or the design. Although very local changes to fibers may also be possible due to

misalignments or fiber waviness, in general this type of error is encountered globally affecting the entire part.

### 1.1.2 Errors in Thickness & Volume Fraction

Depending on the conditions before and during the curing cycle of the composite material, there might occur resin-rich or resin-poor areas, causing either lower or higher volume fraction than the design standards. This change in volume fraction causes a variation in thickness of the material, due to resin content. This effect is shown in Figure 1.3 where for the same number of fibers, additional resin causing a lower volume fraction increases the thickness of the material. Although this error proposes a visible change in the structure, it may not always be easily measured as the variations might occur on complex geometrical parts.

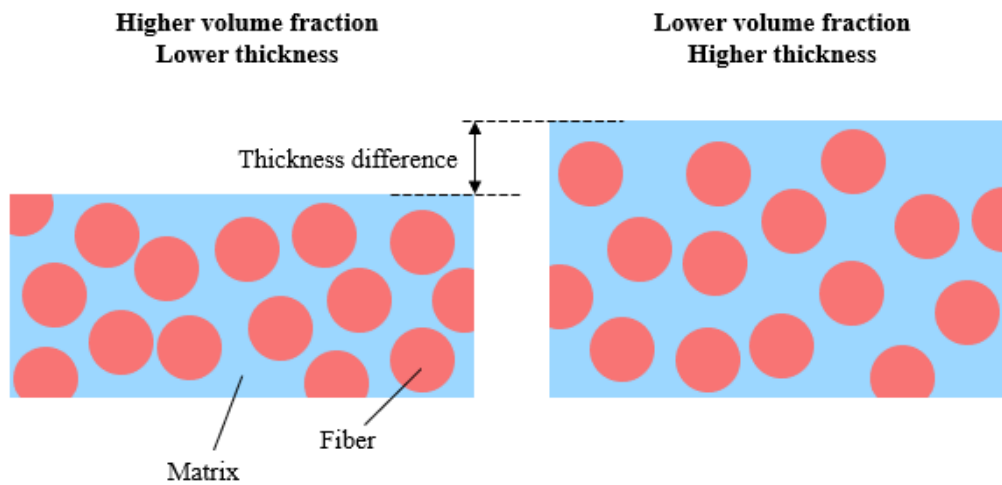


Figure 1.3 Effect of volume fraction on the thickness of the composite

Change in the thickness and volume fraction not only alter the material geometrically, but also affect the mechanical properties of the composite structure. Having both too high and too low volume fractions might make the structure brittle while also significantly altering the elastic properties and the strength.

In filament winding process, most of the resin movement occurs during the winding rather than during the curing process. Additional resin may be removed through help of shrink tapes with negative thermal expansion coefficient wound over the composite structure during its curing. Although the volume fraction can alter locally in other manufacturing methods, it occurs on a grander scale for filament winding process.

### 1.1.3 Delamination Errors

Delamination occurs when two adjacent plies in a laminate debond from each other, causing a gap in between the structure as shown in Figure 1.4. This type of defect mainly occurs due to out of plane shear stresses occurring during the manufacturing process or the weakening of chemical bonds at the interface of two plies due to phase or material difference. It can also occur due to mechanical loading on the part during machining or its assembly.

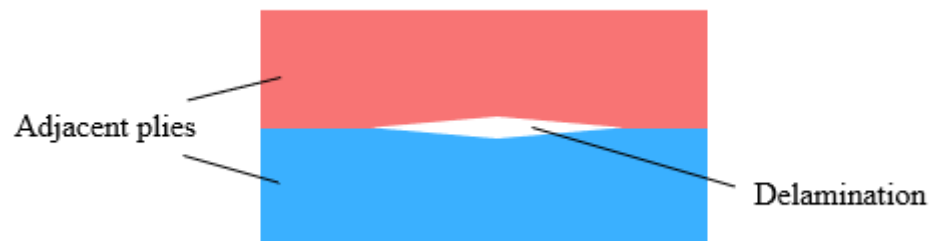


Figure 1.4 Debonded surfaces and the gap in between created by delamination

Although the ply interfaces are separated, there needs not be a physical gap between the two plies when they are delaminated. Hence, two plies seemingly in contact might be delaminated while going unnoticed by the conventional quality control tests.

For a global delamination on the part, stiffness and damping characteristics of the structure change. This is due to the motion of the gap causing effects of friction,

sliding, and impact. The free surfaces also cannot carry shear loads through the section, altering the load path and leading to a stiffness change.

## **1.2 Thesis Overview**

In this thesis, a methodology is derived to assess previously mentioned errors occurring during the manufacturing process at a global scale on the part. The method is then validated through numerical simulations and finally through experiments on produced healthy and defected parts.

In Chapter 2, a literature review is given covering the main methods used in the industry to assess the manufacturing errors of composite materials. These methods are divided into categories based on the principles used, and some supplementary methods that are combined with others are also given.

In Chapter 3, a method based on mechanics of composite materials and optimization of laminate stiffness is considered. The optimized laminate stiffnesses are then input into a loop that contains an artificial neural network that outputs individual ply angles given the laminate stiffness. The process is iterated until the ply angles are converged.

In Chapter 4, to cover thickness variations, the method presented for ply orientation errors is expanded to cover volume fraction of the composite laminate. The process is the same, but first the volume fraction is converged in the process. Then at a set volume fraction, rest of the ply angles are converged.

In Chapter 5, for delamination, vibration modes that are affected by the delamination are magnified by the addition of a local mass to the region. Hence, compared to the original structure either new mode shapes appear, or the existing modes shift differently compared to the healthy structure with the addition of local mass.



Although the main objective of the thesis is to cover pressure vessels, plate and cylindrical structures were also considered mainly for their simplicity and their similarity in case of the cylinder.

In Chapter 6, the thesis is concluded and future work on the subject is discussed.



## CHAPTER 2

### LITERATURE REVIEW

Structural health monitoring techniques have been developed after many accidents caused by unanticipated damages in structures. This approach has been employed for composite materials meticulously due to the fact that composite materials may inherit damage from within, not always visible from surface. Methods employed for defect detection in composite materials are summarized based on the principles used for each method in Table 2.1.

Table 2.1 Methods found in literature used in defect and error assessment

Principle Used	Method
Dynamics & Vibration	Frequency Change
	Mode Shape
	Curvature Change
	Flexibility Change
	Frequency Response Function
	Modal Strain Energy
Acoustics	Acoustic Emission
	Ultrasound
	Lamb Waves
Optics & Radiation	Thermal Imaging
	X-ray
	Microwave
Other Methods	Shearography
	Computed Tomography
	Neural Networks
	Electrical Properties

From what is present in literature, methods based on dynamics & vibration, acoustics, optics & radiation are widely available and are used for composite materials. There are also other methods that are either used supplementary to other existing methods or are used by themselves but are not as popular. Below, the works presented in literature are given based on the principles used to identify the defects.

## **2.1 Methods Using Principles of Vibrations & Dynamics**

In literature, it was identified that defects in composite materials are affecting the vibrational characteristics of produced parts. Hence, several characteristics of the produced parts such as natural frequencies, mode shapes, curvatures, flexibility, frequency response functions (FRFs), and modal strain energy were measured to assess the errors in structure. It was also found that these methods are not always employed alone, and sometimes require several different metrics in order to improve accuracy or localization of defects. Reviews of the literature presented by others as given below.

Zou et. al. provide a review for composite plates and consider frequency, mode shape, curvature, and impedance based methods [6]. It is argued that for most common NDE methods employed like acoustic emissions, showing global mistakes is either very hard, time consuming, or expensive. The mentioned methods are adequate to detect such global defects. Both high frequency and low frequency methods are discussed, and they are good at detecting local and global defects respectively. However, an algorithm that employs both low and high frequencies has not been considered yet. Impedance models discussed use mostly mechanical impedance measurement of force over velocity. The strength of this method is locating planar defects such as delamination. Another discussion is the curvature-based method, which shows promising results compared to experiments. It is also underlined that a mass-based approach might be more feasible due to it having more sensitivity against damage in structures. The article sums up by mentioning that

multiple methods must be at work to correctly assess the damage in both its location and size.

Carden et. al. provides a review for all the dynamic methods mentioned above that is used for damage assessment [7]. The discussed methods are employed on both composite and metal rods, beams, plates and cylinders. It is discussed that either time, frequency, or modal domain should be chosen in order to detect the defects. It is underlined that low frequency analysis is not suitable for local detections, although it is only good at detecting fatigue damage locally. It is advised to use frequency shift-based techniques only to find the location of the defect. For the assessment of how the damage affects the structure, the damage criterion is important, it is mentioned that most of the defect detection techniques in literature are bound to their damage criteria for both locating and identifying them. For the curvature-based methods, it is shown that the curvature takes extreme turns around areas containing defects, and it is found that this method can be modified to be more sensitive than modal shape-based methods. Modal energy-based methods use the idea of if a mode is storing large strain energy in a load path, then both frequency and mode shapes will be exceptionally sensitive to the load path. Hence, the concept of modal energy can be employed, although it is shown that this method can provide false positives for defect localization. Another method that appears in this article is the residual force method. In this method, the damaged structure is taken to be the same as healthy structure, except with specific forces exciting the healthy structure. This means that the damaged structure consists of the healthy structure having its mode shapes excited at specific values. When the structure is not healthy, it can be shown that for some modes these coefficients may become very large. Although this method is very good for localizing the defects, it cannot determine how big the defect is. Most of these mentioned methods are also employed with model updating, where an algorithm dictates the properties of regions in the model after each iteration. This method is mostly used with frequency response functions (FRFs). Finally, damping is discussed to be one of the main parameters that is affected by defects in the structure but has the downside of accurately measuring for complex structures.

Fan and Qiao in their review study, focus on frequency, mode shape, and curvature methods mainly [8]. The structure types considered are almost entirely composite beams. In this review, it is mentioned in literature that most of the natural frequency-based methods are using Euler-Bernoulli beam approach, and consider the defects (mostly cracks) as a rotational spring. Hence, this method is model dependent. It is discussed that modal shape methods only work really good in certain locations. The improvement of both of these methods via wavelet analysis is discussed. For last, curvature-based methods are mentioned including damage index, which show promising results in finding large area damages like low velocity impact damage or delamination.

Considering the reviews, methods used under principles of vibrations and dynamics were further investigated. Previous work in literature under the methods presented in Table 2.1 are given below in further detail.

### **2.1.1 Frequency Change**

Salawu in their study of steel and concrete bridges discuss the idea of using high frequency mode shapes to localize damage [9]. A requirement of 5% change in frequency is stated for the damage identification. Change of boundary conditions during service life is underlined, and its effect on natural frequency is discussed. The article also mentions that cracks of same size at different locations may cause same frequency shift, hence strengthening their argument for usage of other methods on top of frequency change.

Dolinski et. al. works on a composite rotor blade and shows that a frequency-based method would only give global results, they would lack location and size of damage information for local defects [10]. A continuous wavelet analysis has been employed to find the location of delaminations. The results are not exactly accurate, and for small defects localization may not be possible.

Gadelrab in their study of composite beams, divides the beam into parts of defected and undefected regions [11]. Compatibility conditions are introduced between the regions to obtain extension bending coupling for the structure. Delaminations are of interest for this article, and natural frequency of the structure is checked to detect the flaw. The results of the study imply that delaminations close to or around a fixed or modal point are hard, if not impossible, to detect.

Cawley and Adams use a frequency-based method for composite plate geometries [12]. Their modelling of defects consists of the removal of cross-sectional area of the structure. It is found that Ratio of frequency change between healthy and defected structures of two different modes is only a function of location of the defect. Therefore, this parameter is used to locate the defect. A damage index is used to assess and identify the defect, and a weighting of modes is introduced which has a weighting algorithm that checks if two different modes have principal stresses pointing in same directions over the modal shape. For the experiments, a piezo strain gauge is used.

Cawley and Adams worked on the natural frequency characteristics of a free-free composite plate [13]. The free-free boundary condition was obtained by hanging the plate with flexible strings. The excitation of the plate was done by loudspeakers to avoid contact. Data from the plate is collected by strain gauges, and it shows a 6% error at maximum for the data taken. Transverse shear effects were also checked and found to be negligible. It was concluded that mode shapes depended strongly on ply orientations.

Ullah and Sinha worked on deflection mapping of composite plate surfaces at high frequencies (10kHz) [14]. Two plates were checked, one with delamination and other had no defects prior. It was found that both healthy and delaminated plates had almost identical natural frequencies. The main difference was seen when the velocity data was gathered from the surface. On the delamination site, a huge difference existed between the two plates. A damage criterion based on harmonics was employed and correctly showed the location of defected region.

Dawood et. al. employ a Gaussian wavelet of order 2 to estimate the Lipschitz exponent in order to evaluate the the severity and location of the damage introduced on sandwich beams [15-17]. The damage is modelled as a reduction in stiffness, and experimentally a core-skin debond is introduced to investigate the effect of the damaged beam.

### **2.1.2 Mode Shape**

Friswell et. al. shows that damage causes a stiffness loss for beam and plates that are not composites or made from an anisotropic material [18]. Hence a method including penalty function which reduces the local Young Modulus is considered. A genetic algorithm is used which reduces the stiffness of unfit elements in the next generation. The output of this algorithm is to match with the mode shapes of the original defected structure. Since the method takes the input mode shapes, and compresses it to a single quantity, it technically loses information and can provide false positives.

Hamey et. al. considers frequency, mode shape, and curvature to locate defects in beam type composite structures [19]. Frequency based methods are classified to not be suitable to use alone due to the method producing same frequency shift for a large delamination, and two smaller delaminations. It is further shown that impact-based damages produce almost no shift in natural frequencies. This case is also hard for mode shape methods because the general mode shapes do not change, only major changes can be observed at the starting points of delaminations. For experimental purposes, impact hammer tests are done but the areas of interest contained a lot of noise. Even with first three mode shapes considered, assessment of location, identification, and severity of the defects could not be found with confidence.

Katunin and Przystalka produces a model based on mode shapes and FRF data taken by a laser Doppler vibrometer [3]. For composite plates that have been investigated, FRF data is taken to evaluate the mode shapes. Although from the damage was



already known due to FRF data taken, a genetic algorithm is used to localize the damage and identify it with high accuracy.

Shams et. al. show the change in the normalized mode shapes in the presence of a delamination using dynamic stiffness matrix method [20]. A beam geometry was considered, where at the delamination multiple different beams were coupled to estimate the response of the structure. Different modelling techniques were compared, and their results were validated through finite element analysis.

### **2.1.3 Curvature Change**

Lestari et. al. uses curvature method on composite beams [21]. The idea is to track the modal nodes which may shift due to defects in structure. The downside of the method is assuming the wave shape of the structure, so it cannot be suitably employed for complex structures. The damage is introduced as a perturbation, and a curvature damage factor, which is based on the curvature difference from original structure, is used to identify the source of damage. Different types of defects are considered in their study.

Ratcliffe and Bagaria states that no single dynamic property can be measured to directly indicate what type of damage exists [22]. In their article, curvature method was used for a composite beam. A delamination was moved both along the beam and in thickness direction for the defect introduction. A gapped smoothing method is used which according to writers is superior to both the differentiating method and the unmodified curvature method. In this technique, the beam is divided into a grid and measurements are taken from grid points.

### **2.1.4 Flexibility Change**

Vo-Duy et. al. considers a composite beam and derives its equation of motion [23]. The modelled flexibility is then used to process a single quantity which represents

the cumulative normalized energy. It can be shown that this quantity will be zero for damaged elements in the structure. Damage locating vector-based method is used combined with this quantity to accurately detect the location of defects.

Aoki and Byon works on composite hollow circular beams and uses flexibility based methods to detect the defects [24]. Many strain gauges were used along the beam length to correctly measure the rigidity changes along the beam. The method, however, does not give information about where, what, or how bad the defect is. It rather only provides information about if a defect exists in the structure.

Pandey and Biswas investigates the flexibility concept on composite beams [25]. The flexibility is checked for damaged and undamaged structures for different boundary condition types. The study is concluded with results showing that damage near fixed ends were almost undetectable. Also, it is underlined that the stiffness matrix contribution increases as the frequency increases, but only few lower modes can be investigated for complex structures. Hence, rendering this method limited to basic geometries. It is also noted that flexibility methods work best with first few modes.

### **2.1.5 Frequency Response Function**

Kessler et. al. claims that frequency domain analysis is not enough to localize the defect for composite plates [26]. It requires time data to localize the defects. In the article, defects such as holes, matrix cracks, and delaminations are used and radiography is used to locate the defects as a control group. Piezosensors are used to take both frequency response and impedance measurement. The experiment phase is done with vibrometers. The results concluded that for low frequencies and their respective mode shapes, the only detectable damage was fatigue, which would present mode shapes that were not present in healthy structure.

Zak et. al. mathematically models delamination for a composite beam and plate [27]. For this formulation, the beam is divided into two sections: healthy part and delaminated part. Derives a finite element for the delaminated part of the beam and

does modal tests to compare the frequency response for large delaminations. The mathematical model gives confident results for delaminations taking up over 40% of the structure.

Yang and Oyadiji propose a novel method to insert delaminations in the structure [28]. Natural frequency difference, mode shapes, and frequency response functions were checked to understand the effect of delamination on the structure. A new delamination mode was found on the frequency response function for the near surface delamination case at low frequencies.

### **2.1.6 Modal Strain Energy**

Kumar et. al. uses modal strain energy, since their study yielded the information that it performs better over other dynamic based methods [29]. A stiffness loss is introduced as a perturbation and FRF measurements are taken to validate their model. Combined with the experimental data, finite element analysis is used to increase the confidence of the model. Damages that engulfed more than 5% of the structure was identified correctly. The novelty of this study lies in the damage identification algorithm it uses.

Hu et. al. introduces the modal strain energy method on composite plates [30]. The plate is divided into grid sections, and each grid point is excited with a modal hammer. Uses the strain energy method for mode shapes and uses a damage index for the ratio of the modal strain energies for damaged and undamaged structure. Surface cracks were detectable via this method.

Vo-Duy et. al. considered composite plates in their work [31]. The damage was modelled as a reduction in stiffness, and modal strain energy method was used to find the location of the defect. A differential evolution algorithm was used to quantify the extent of damage on the defect site.

## **2.2 Methods Using Principles of Acoustics**

Similar to the case of vibrations & dynamics, it was identified in literature that defects in composite materials may cause an alteration in acoustic performance or waveforms. Mainly acoustic emissions, ultrasonic performance, and lamb waves were measured to identify the errors. The current work in literature for these methods based on acoustics are presented below in further detail.

### **2.2.1 Acoustic Emission**

Arumugam et. al. studied a delamination introduced by a Teflon tape in composite plates [32]. Different damage types were considered such as matrix cracking, delamination, fiber bond failure, et cetera. It was found that same type of patterns occurred in acoustic emission monitoring for each individual defect type. Wavelet transforms were used to distinguish the damage type ranges, yet it was found that these gaps collided with each other, so identifying certain damage types were not always possible.

Sung et. al. collects acoustic emission data on composite plates and then uses a time frequency analysis to assess the damage [33]. The number of sensors used was kept at minimum due to cost. Delamination was modelled with an evolution-based algorithm and wavelet analysis was done to localize the data in both time and frequency. Moire fringes were observed which indicated delamination in the structure. On top of this, matrix cracks could also be located.

### **2.2.2 Ultrasound**

Smith inspects composite plates by many different NDE methods [34]. In the study, ultrasonic methods were found to be able to detect even the voids in structure. It is noted that detection techniques used must measure a quantity that is significantly changing from healthy to damaged state.

Mahmod et. al. discusses ultrasonic methods in detail [35]. In this article, different defects were introduced in composite plates, and their location was successfully determined from ultrasonic flat probes.

Ng et. al. used ultrasonic method on a coarse grain structure, which was a challenge because of the introduced grain noise [36]. To reduce this noise, wavelet analysis was done to the experimental data.

Hudson et. al. uses laser ultrasound, which is a non-contact type ultrasound, to find local defects in composite plates [37]. The main focus was localizing the defects in overlap situations where defects can collide. The method successfully found the defects and was able to even find porosity in the material considered. Although the study only considered a few defects, for the future work new defect types will be considered such as waviness, gaps, and voids.

Taheri and Hassen used guided wave approach with piezo sensors [38]. The defects introduced on the composite plate was actual holes drilled. Like other ultrasonic based methods, the size of the defect was very well obtained but the type information of the defect was not obtainable through this method.

Wang and Zhou introduced a water-logging ultrasonic pulse technique and explains in depth how the method would work to find different types of defects in composite plates [39]. Although, as mentioned earlier, one needs to be expecting a certain type of defect to correctly identify it.

### **2.2.3 Lamb Waves**

Su et. al. investigate composite beams and plates by the usage of lamb waves [40]. The response measured by the excitation was investigated as a function of both time and frequency. It is discussed that lamb waves can be used with many sensors to get the tomography of the structure. However, doing so would require many sensors and would both be time consuming and expensive. The writers put the surface coatings in attention for the possibility of high damping introduction to the structure.

Kirikera investigates composite wind turbine plates and introduces a neural based wave simulation algorithm based on lamb waves to investigate the defects caused by impact [41]. The model, which is based on thin plate theory, ignores the transverse shear and rotary inertia effects. The algorithm only takes high frequency data due to the filtering techniques used, and it can successfully identify various types of damage such as buckling, shear web bond-line failure, and surface damage.

Waghulde and Kumar used piezoelectric wafer sensors to detect delamination in composite beams [42]. The delamination was introduced by the insertion of a Teflon slice during production. Lamb waves were excited by some of the PZT sensors, and the data was obtained from the others. The flexural type lamb waves were highly dispersive, yet the damage could be found for different shaped Teflon inserts.

### **2.3 Methods Using Principles of Optics & Radiation**

Generally, methods based on optics & radiation are applied for local defect detection according to the literature. The methods used for these cases can be summarized under thermal imaging, x-ray, microwave, and shearography. Works presented in literature for these methods are explained in detail below.

#### **2.3.1 Thermal Imaging**

Gamier considered many different composite geometries in their article such as hollow rods, plates and bent plates [43]. Each of these geometries introduced a challenge because due to geometry, certain type of NDE methods were not usable. For example, ultrasonic flat probes could not follow the cylindrical surface of the hollow rod. On the other hand, infrared thermography worked excellently for detecting the defects in that situation. While shearography method was used to identify the defect type, thermography was used to locate and assess the size of defect. It was acknowledged that ultrasonic data would be more accurate for these cases, but as shown earlier, it cannot be always applied.

Ramos da Silva focuses on thermal based methods in their thesis based on composite plates [44]. Many thermal imaging methods have been explained and were tested against many different signals obtained from the composite. Heating of composite and how to handle the thermal methods with that in consideration is discussed.

Beattie and Rumsay made a controlled study on composite wind turbine blades [45]. A black aluminum block was used as a control group which had the same initial temperature as the structure in question. This obtained average was subtracted from the original structure's data, so the only remaining part was the alternating data alone. The DC (steady) data was mainly consisting of temperature effects while the AC (alternating) data contained the stress state information. Fatigue tests were employed on the wind turbine blade, and this method was able to identify complex cracks inside the structure. It was noted that emissivity of the blade was important to obtain correct information about the structure.

Pastor et al. used both infrared thermography and acoustic emissions to assess the damage in composite plates [46]. Acoustic emissions found all the defects successfully while thermography had troubles in identifying some of them. Delamination, peel ply, Teflon coated fiber glass were the defect sources. The strength of thermography was the speed and cost. While thermography was suitable to implement into a real time health monitoring system, acoustic emission-based method was not.

### **2.3.2 X-Ray**

Soete et. al. focuses on different types of production for composite plates [47]. A comparison study was done for 3D printed fiber composites and resin impregnated ones. It is well discussed in literature that 3D printed composites performed worse in strength. X-ray tomography of the structure was taken and various types of defects were observed such as voids, fiber twist, inter-bundle and matrix tearing.

### **2.3.3 Microwave**

Meitzler et. al. studied the disbanding defects on composite plates [48]. In this paper, not only x-ray and microwave methods are used, but ultrasonic methods are employed. Ultrasonic methods are usually used for one type of material, whereas the sandwich setup considered had more than three. From these three methods, x-ray provided the most in-depth defect observation with it locating the cracks and showing their sizes. Microwave based method was less successful, although it was able to find the defects while the composite was in assembly with other parts. It was concluded that ultrasonic based method was not suitable for this type of sandwich plate that consists of different materials.

### **2.3.4 Shearography**

Hung worked on shearography for composite plates [49]. Explains how shearography works in depth: lasers are sent to the surface and due to the irregularities or defects on surface, they will be sent in different directions. A shearing device is used to collect the lasers and after post-processing the surface could be imaged. Edge pull-outs and delaminations were detected, but the method was not suitable for identifying the defects occurring inside the composite.

## **2.4 Computed Tomography**

Despite the success of other methods previously mentioned, several new methods that are not as popular are also considered in literature (such as measurement of electrical properties), and some methods that are only used complementary to others are also available (computed tomography processing, neural networks and optimization processes). The supplementary methods are mostly used to improve the reliability or accuracy of existing methods. These methods are mostly based on



optimization techniques or data processing. The methods present in literature for these mentioned cases are explained in detail below.

Katunin et. al. tests two different composite plates of different production technique [50]. Damage was introduced by holes in the middle of the plates. A CT scanning is done, which is Xray based, and tomography of the structure was taken. It was found that the drilled hole caused delaminations around the drill site. Postprocessing with wavelet analysis is done to obtain more accurate information about the severity of the defect. Although his measurements contained a lot of noise, delaminations and air pockets could be found in the structure.

Foss et. al. analyzed mold filled composite plaques and disks and found flow directional components. These flow directional components are then related to fiber orientations, within 15% error for all considered cases [51].

Tseng et. al. considered a long fiber plastic composite plaque geometry and used improved anisotropic rotary diffusion and retarding principal rate (iARD-RPR). Using this method, they obtained orientation of the fibers in 3D space [52]. Later, yield stress viscosity is added to standard cross-WLF viscosity model to improve the predictions of fiber orientation [53]. Thickness average orientation tensor components were obtained within 12% error of experimental results using this improved method. Results of iARD-RPR were compared at transient shear flow with micro-CT scan results, and 4% maximum error was obtained in predicted elastic modulus [54].

Song et. al. shows that the initial bulk charge being compressed influences the fiber orientation of a discontinuous fiber reinforced thermoplastic composite [55]. These parameters were included in simulation and CT is used to estimate the fiber orientation.

Baranowski et. al. changed their approach to the problem of obtaining fiber orientations by considering a larger volume in the structure that includes fewer voxels [56]. Instead of the individual orientation of the fibers, a new texture

orientation defined for the volume is found. It was also shown that for a complex geometrical part, simulations are not always enough to estimate the fiber orientations.

Quintana et. al. shows that simulations for a venturi shaped molded part fail to estimate change in fiber orientation. They found that this change was mainly caused by variable thickness and section, as obtained through micro-CT [57].

Kratmann et. al. employ a method based on fourier transform and logarithmic power spectrum computation on micrographs [58]. The method requires further image processing based on an object and frequency filter, which enabled the calculation of average fiber direction in their composite structure.

## **2.5 Neural Networks**

Additional post-processing can be utilized on micrographs obtained by CT, which enables the employment of the micrograph as a training data set for neural networks to later identify composite part's fiber orientations.

Creighton et. al. used low-magnification micrographs to predict the fiber orientations in a carbon-epoxy based composite [59]. The orientation is obtained through the elliptical shape of fibers seen from the cut angle in micrograph and relating them to the original circular cross-section to obtain the fiber orientations through neural networks.

Sabiston et. al. use an artificial neural network employing 3 hidden neural layers to predict fiber orientation tensor for a complex geometry [60]. The method unfortunately requires a lot of X-ray CT training data prior. However, once the neural network is trained, it can be readily used to obtain the results at a near instantaneous pace.

Bleiziffer et. al. present an analysis by inertia tensor evaluation and a convolutional neural network approach [61]. Using their convolutional neural network approach,

it was shown when compared to experimental micro-X-ray CT results, 99% of predictions were predicted within an error range of 10%.

Zhang et. al. used an algorithm employing finite element model and artificial neural networks to locate and estimate the area of delamination in curved composite parts [62]. Their method optimizes the difference in natural frequencies and is based on a genetic algorithm, which is a stochastic optimizer. In the genetic algorithm, the best of the “population” is used to crossover new members of the population and is then looped back into the neural network until convergence is achieved.

Şahin and Shenoi employ an artificial neural network to identify the location and severity of the damage on a composite and steel beams using natural frequencies and mode shapes as the input [63-65]. Later, a similar study is conducted by Şahin [66] as well employing a single hidden layer artificial neural network. The damage was modelled as a reduction in stiffness. A sensitivity analysis was performed to find the necessary parameters for damage detection.

## **2.6 Electrical Properties**

Electrical properties of the composite material are also directional and can be measured to obtain ply orientations. Such methods usually employ a current in a test probe that causes an inductive current on the part tested. By measuring the strength and phase of the inducted current, both local defects and fiber orientations can be detected.

Mook et. al. has detected fiber orientation in a carbon fiber reinforced plastic composite using both a static and rotary probe [67]. Rotary probe could readily identify the fiber orientations, but static probe needed lateral movements to predict the same orientations.

Wu et. al. later has improved the method by eliminating fluctuations caused by errors such as lift-off. A self-resonant system was produced that has amplified signal to

noise ratio. This was necessary to avoid the errors caused by the high frequencies employed [68,69].

Terahertz time-domain spectroscopy is also used in literature to measure dielectric constants, which as discussed before can then be related to fiber orientations and layup configuration. Park et. al. used the difference between a reference and sample part to calculate complex relative permittivity [1]. Dielectric constants of 3 different layups are predicted within 0.25% error by employing different polarization angles.

### 2.7 Discussion of Information Present in Literature

Although many different methods are present for nondestructive evaluation of composite materials, each of them has their suitable uses due to their strengths and weaknesses. The general use of these methods for detection of various types of defects are shown in Figure 2.1.

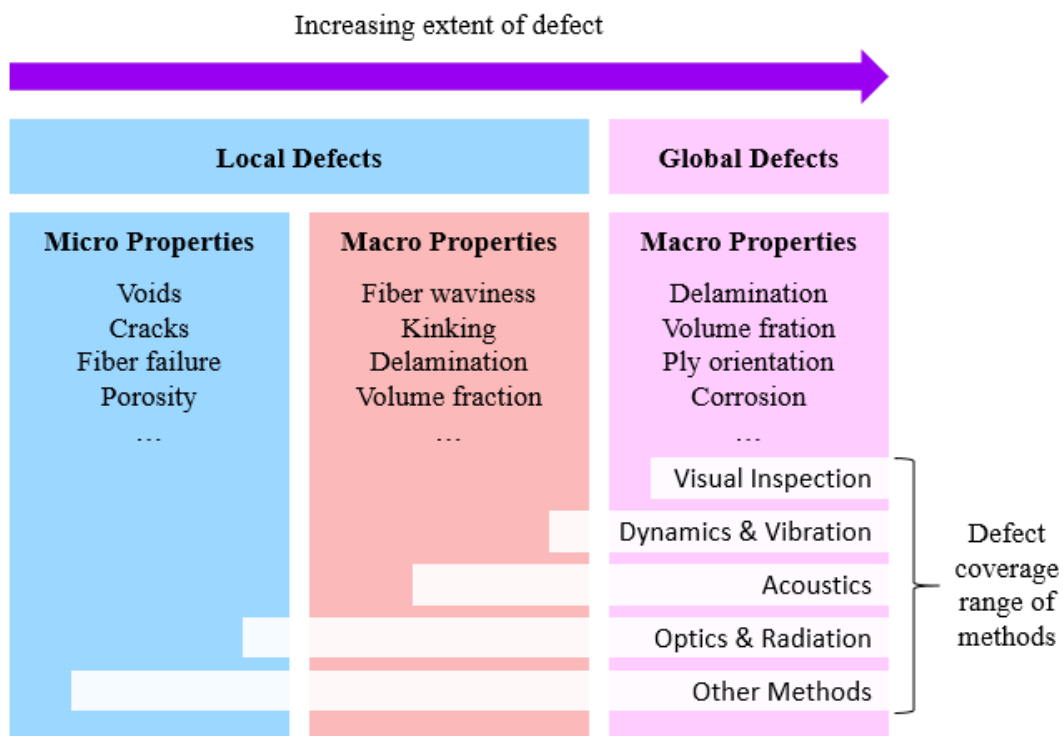


Figure 2.1 Coverage of structural health monitoring techniques on detection of defects

It is shown that methods based on vibrations & dynamics are more suitable for the use of detection of errors that occur on a global scale on the part. Acoustic based methods are more precise than the ones based on vibrations & dynamics, but they mainly assess the structures locally, and either an array of sensors or several tests are required to globally identify the defects in the structure. For methods employing optics & radiation principles, they are very accurate for local defects but are not suitable to be used for the entire part. This means that possible error locations in the structure have to be predicted beforehand so that it may be assessed with these more accurate methods. Other complementary methods may be used with any of the aforementioned methods, and in general improve them in certain aspects but may cause significant time or cost issues.

In the industry, usually methods covering a wider variety of defects in the structure are either more time consuming or are costlier. These methods are also developed to assess local defects mainly, therefore rendering them mostly useless for global defects. Although, compared to methods covering less defects, they are more precise and can infer more information about the defect in the structure. Considering the objective of the thesis, a fast, reliable, and relatively cheap method is required in the industry that can assess the manufacturing errors encountered globally through the structure. From the literature review, methods based on principles of dynamics & vibrations is visibly the strongest contender to assess such errors. Therefore, in the following chapters where identification of each error in the structure is presented, the identification methods used will be based on principles of dynamics and vibrations.



## CHAPTER 3

### IDENTIFICATION OF PLY LAYUP CONFIGURATION

Errors in ply layup configurations are one of the most commonly encountered errors in production of composite parts. Due to the changes in ply orientations, mechanical behavior of the produced parts is heavily altered. Given a high extent of this error, it is not rare to see major distortions or even direct failure of the part can be encountered.

Depending on the geometry at hand, all types of ply orientation variations may not be possible. For example, on simpler geometries like plates, any angle might be encountered. However, for a more complex part like cylinder or pressure vessel, either the layup may be confused so that the placement of two plies in the laminate may change or slippage of the fibers on the wet resin may occur, slightly altering the orientation angles within a band of  $15^\circ$ . It should also be noted that due to the nature of filament winding process, when an angle ply is laid out the opposite angle is always laid out with it, resulting in an always balanced laminate. Hence, balance errors cannot be encountered.

No matter the constraints on errors in ply layup configuration, all of them present a major change in the composite material mechanics. Therefore, it is elementary to first fully understand the material mechanics so that it may be used to model the differences in test results. In this chapter, first an introduction to mechanics of long fiber composite materials is given, and later the proposed method to assess this type or error is presented, which later is validated through numerical simulations and experimental results.

### 3.1 Mechanics of Composite Materials

Ply orientations and stacking configuration are the key factor that affects the stiffness of the laminate and its mechanical behavior. In this section it is explained how to assess the stiffness of the laminate, relating the section forces and moments to strains and curvatures.

From various material tests, the properties of a single ply are known preliminarily in the fiber and transverse directions. However, a single ply of composite material does not necessarily align to the plane of global coordinates as shown in Figure 3.1. Hence, to estimate the global response of the laminate, stiffness of each ply must be transformed from its local coordinates to the global coordinates.

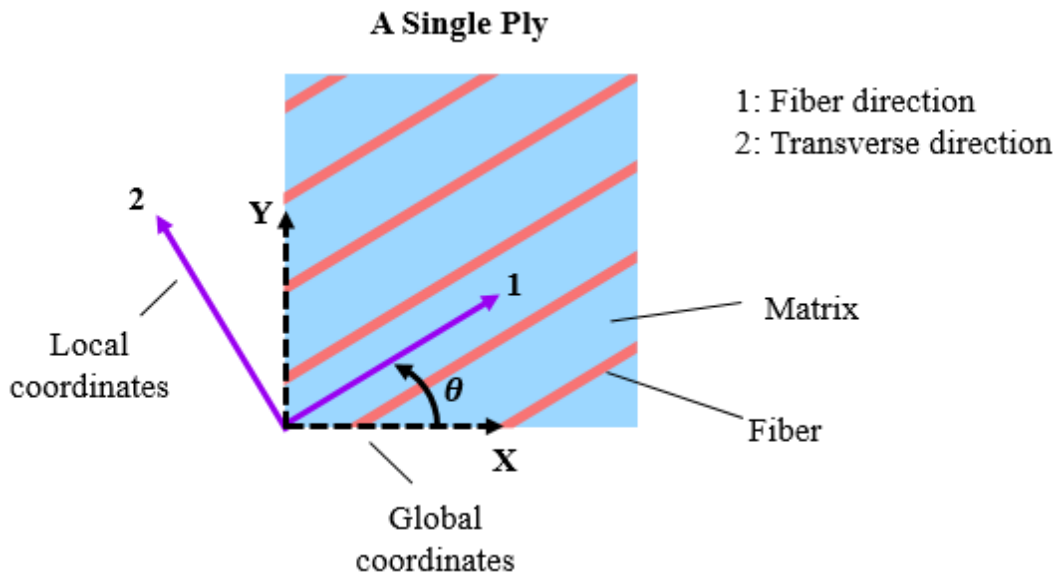


Figure 3.1 Alignment of a single ply compared to the global directions.

Due to the nature of filament winding process, the produced composite parts always infer plies that are orthotropic. For an orthotropic composite material, the constitutive relation for the orthogonal planes describing the relation between stresses and strains can be expressed as:

$$\varepsilon_1 = \frac{\sigma_1}{E_{11}} - \frac{\nu_{21}\sigma_2}{E_{22}} \quad (3.1)$$



$$\varepsilon_2 = \frac{\sigma_2}{E_{22}} - \frac{\nu_{12}\sigma_1}{E_{11}} \quad (3.2)$$

$$\gamma_{12} = \frac{\tau_{12}}{G_{12}} \quad (3.3)$$

Where  $\varepsilon$  are normal strains,  $\sigma$  are normal stresses,  $\gamma$  is shear strain,  $\tau$  is shear stress,  $E$  is elastic modulus,  $G$  is shear modulus,  $\nu$  is Poisson's ratio, and 1 & 2 denote fiber and transverse directions of the ply.

These equations are true for the principal directions of the ply. However, to obtain the relationship of stress and strain in the global direction, a coordinate transformation must be applied. The stresses in the global coordinate systems can be obtained from the local coordinate system as:

$$\sigma_{xx} = \sigma_1 \cos^2 \theta + \sigma_2 \sin^2 \theta + 2\tau_{12} \cos \theta \sin \theta \quad (3.4)$$

$$\sigma_{yy} = \sigma_2 \cos^2 \theta + \sigma_1 \sin^2 \theta - 2\tau_{12} \cos \theta \sin \theta \quad (3.5)$$

$$\tau_{xy} = \sin \theta \cos \theta (\sigma_2 - \sigma_1) + (\cos^2 \theta - \sin^2 \theta)\tau_{12} \quad (3.6)$$

Where  $x, y$  are global coordinates, and  $\theta$  is the angle between fiber direction and global  $x$  coordinate.

It is, however, more convenient to express the equations (3.4 – 3.6) in matrix form. This form can be shown as:

$$\begin{Bmatrix} \sigma_{xx} \\ \sigma_{yy} \\ \tau_{xy} \end{Bmatrix} = \begin{bmatrix} \cos^2 \theta & \sin^2 \theta & 2 \cos \theta \sin \theta \\ \sin^2 \theta & \cos^2 \theta & -\cos \theta \sin \theta \\ -\cos \theta \sin \theta & \cos \theta \sin \theta & \cos^2 \theta - \sin^2 \theta \end{bmatrix} \begin{Bmatrix} \sigma_{11} \\ \sigma_{22} \\ \tau_{12} \end{Bmatrix} \quad (3.7)$$

More conveniently, equation (3.7) can be expressed in the compact form:

$$\{\sigma_{global}\} = [R_\sigma]\{\sigma_{local}\} \quad (3.8)$$

Where  $[R_\sigma]$  is the rotation tensor that transforms local stresses to global stresses.

Considering the conservation of strain energy, the ply must have the same total strain energy no matter the coordinate system. Therefore, the following equity of energies can be expressed:

$$\int \{\sigma_{global}\}^T \{\varepsilon_{global}\} dV = \int \{\sigma_{local}\}^T \{\varepsilon_{local}\} dV \quad (3.9)$$

Where  $V$  is the total volume of the ply,  $dV$  indicating integration over the entire ply.

From equation (3.9), the rotation tensor for the strains can be obtained as:

$$[R_\varepsilon] = [R_\sigma]^{-T} \quad (3.10)$$

Where  $[R_\varepsilon]$  is the rotation tensor that transforms local strains to global strains.

Therefore, using equations (3.1 – 3.3), (3.8), and (3.10), one can define the following constitutive relationship on global coordinates:

$$[Q_{global}] = [R_\sigma]^{-1}[Q_{local}][R_\varepsilon] \quad (3.11)$$

Where  $[Q_{global}]$  is the inverse of compliance matrix of the ply for the global coordinate system, and  $[Q_{local}]$  is the inverse of local compliance matrix of the ply, constructed using equations (3.1 – 3.3) as:

$$[Q_{local}]^{-1} = \begin{bmatrix} \frac{1}{E_{11}} & -\frac{\nu_{21}}{E_{22}} & 0 \\ -\frac{\nu_{12}}{E_{11}} & \frac{1}{E_{22}} & 0 \\ 0 & 0 & \frac{1}{G_{12}} \end{bmatrix} \quad (3.12)$$

However, the above relations are valid only for a single ply. To define the constitutive relation of the laminate, the previously defined properties must be considered and summed up for all plies in the laminate.

The most general relation for the laminate between forces & moments and the resulting deformations can be expressed as:

$$\begin{Bmatrix} \{N\} \\ \{M\} \end{Bmatrix} = \begin{bmatrix} [A] & [B] \\ [B] & [D] \end{bmatrix} \begin{Bmatrix} \{\varepsilon_0\} \\ \{\kappa\} \end{Bmatrix} \quad (3.13)$$

Where  $\{N\}$  represent the vector containing forces per unit length,  $\{M\}$  represent the vector containing moment per unit length,  $\{\varepsilon_0\}$  is the vector containing strains and  $\{\kappa\}$  is the vector containing curvatures.  $[A]$  is the extension stiffness matrix,  $[B]$  is the extension and bending coupling stiffness matrix,  $[D]$  is the bending stiffness matrix of the laminate. The directions considered for these forces and moments are shown in Figure 3.2.

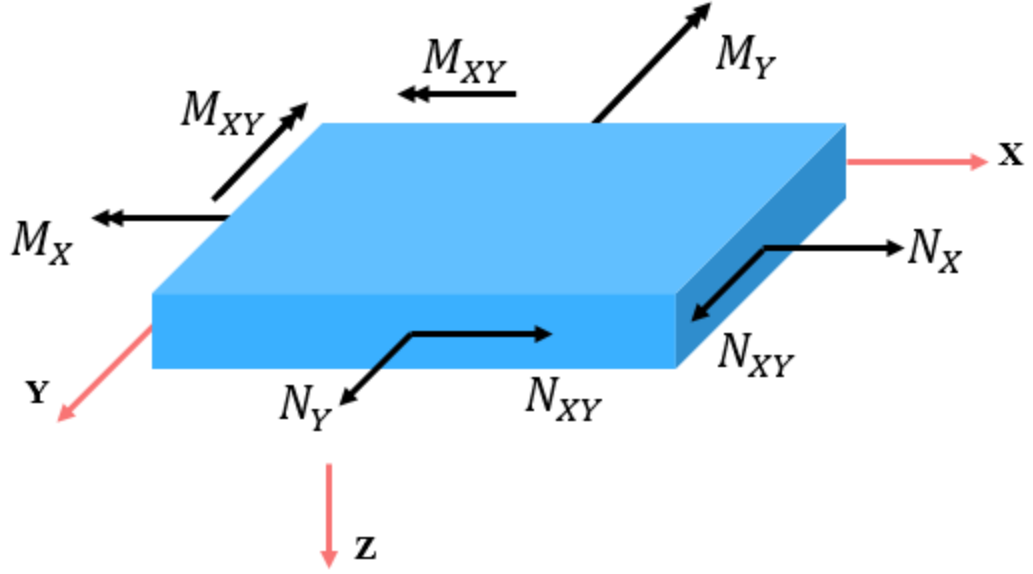


Figure 3.2 Applied loads and moments on the composite laminate. For clarity of the figure, forces and moments are only shown on one side of the laminate.

The stiffness matrices defined as  $[A]$ ,  $[B]$ , and  $[D]$  can be defined as:

$$[A] = \sum_{n=1}^N [Q_{global}]_n (z_{n+1} - z_n) \quad (3.14)$$

$$[B] = \frac{1}{2} \sum_{n=1}^N [Q_{global}]_n (z_{n+1}^2 - z_n^2) \quad (3.15)$$

$$[D] = \frac{1}{3} \sum_{n=1}^N [Q_{global}]_n (z_{n+1}^3 - z_n^3) \quad (3.16)$$

Where  $z_n$  is the distance of the ply with respect to the mid-plane of the laminate in the thickness direction,  $[Q_{global}]_n$  is the inverse global compliance matrix for the  $n^{\text{th}}$  ply. The distances for the  $n^{\text{th}}$  ply is shown in Figure 3.3.

Therefore, the  $[ABD]$  matrix that is shown in equation (3.13) can be used to model the laminate behavior. This matrix, in a sense, is identical to the elasticity matrix for an isotropic material. Therefore, to define the stiffness of the geometry,  $[ABD]$  must be coupled with geometric features.

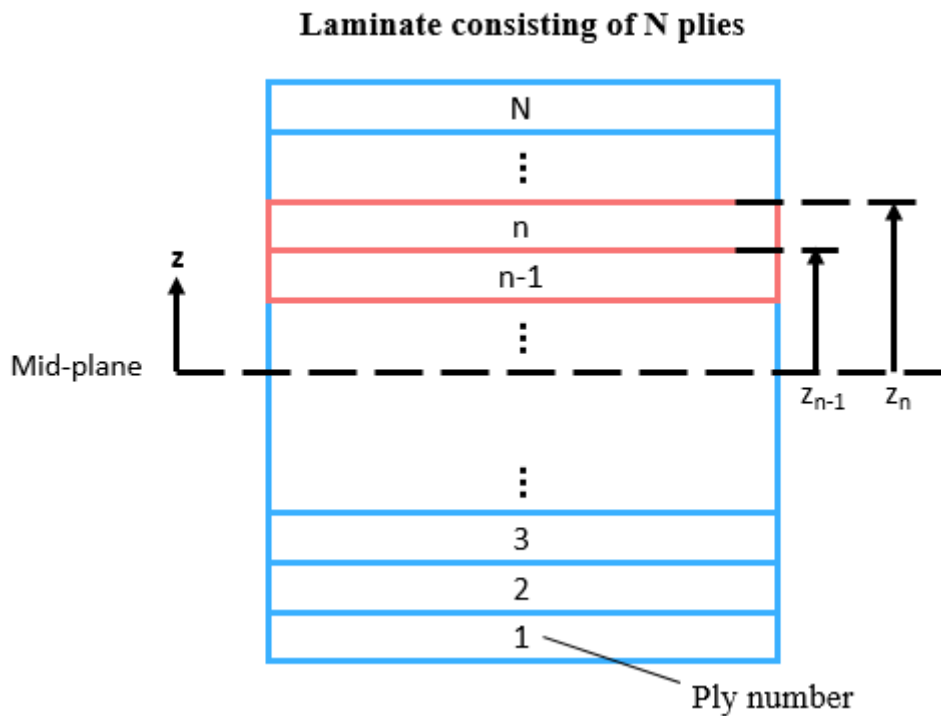


Figure 3.3 Plies and their respective distances to the mid-plane of the laminate

### 3.2 Proposed Method for Identification of Ply Layup Configuration Errors

As was mentioned in section 3.1,  $[ABD]$  matrix is generated by using the material elasticity and ply orientations for the laminate. Combined with geometric features, stiffness of the entire structure can be obtained. This stiffness and mass are going to define the natural frequencies of our structure. Henceforth, it is elementary that natural frequencies of the structure are majorly influenced by the ply orientation configuration of the laminate. Then, since the link exists between these parameters, natural frequencies can be obtained through modal tests and then can be used to identify the ply stacking configuration.

It is assumed that preliminarily quantities obtained through a modal test are known for the composite part considered. Therefore, first few natural frequencies are available. Due to this, the method is divided into three parts. First, a proper range for properties of the laminate are obtained through the first natural frequency obtain

experimentally. Then, in the second step, laminate properties are optimized using the rest of the experimentally obtained natural frequencies and a single laminate property is obtained rather than a range given previously. Finally, the ply properties are optimized given the optimized laminate property through an artificial neural network, and the ply orientations are obtained. The general flowchart of this process is given in Figure 3.4.

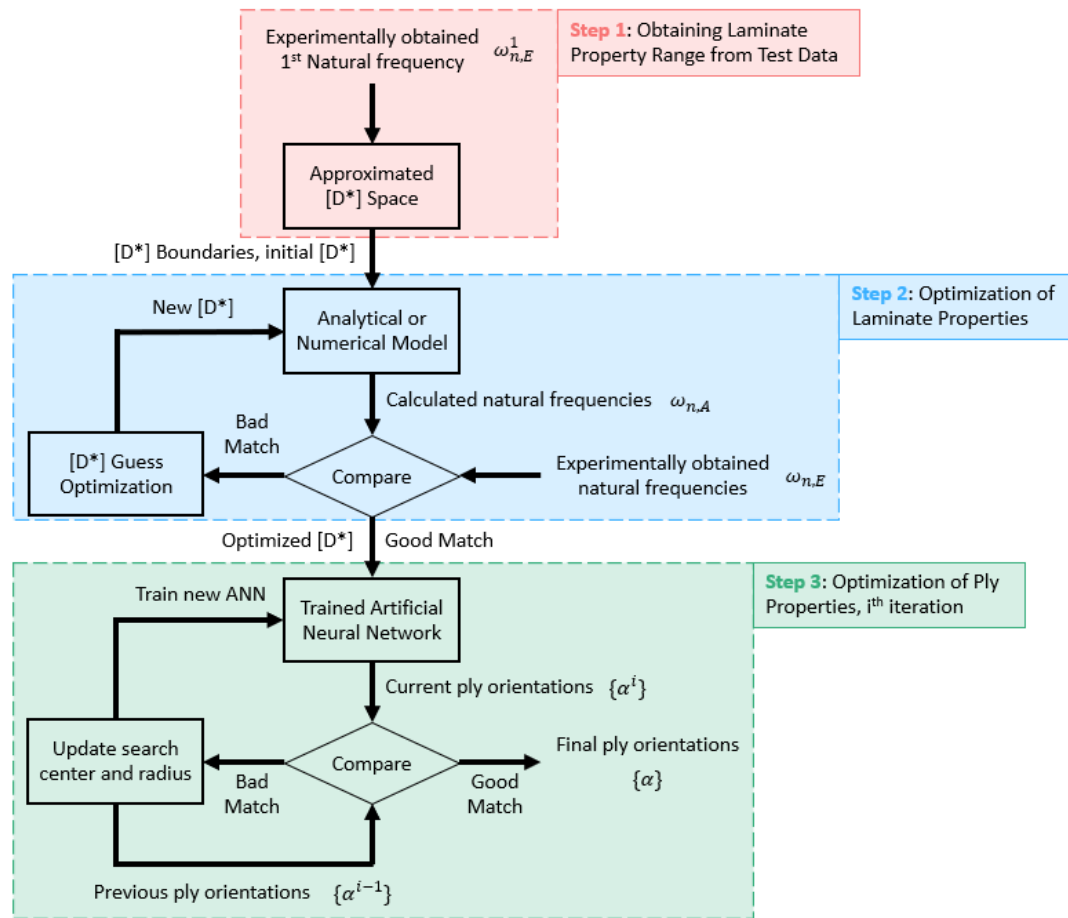


Figure 3.4 Flowchart of the process employed to obtain the ply orientations of the unknown composite laminate

In this flowchart, the laminate properties are selected as the reduced bending stiffness of the laminate denoted as  $[D^*]$ . The ply orientations for the laminate are denoted as a vector shown as  $\{\alpha\}$ . Artificial Neural Network is shortened as ANN. The reduced bending stiffness of the laminate is defined in the following section. The natural

frequencies obtained through experiments and analytical/numerical methods are given as  $\omega_{n,E}$  and  $\omega_{n,A}$  respectively. The first natural frequency obtained through experiments is employed to find an approximated  $[D^*]$  space, amongst all possible configurations that yield different sets of  $[D^*]$  with their own natural frequencies. Then, after this step, a range for the  $[D^*]$  is found. However, a single  $[D^*]$  is required to identify the part. Therefore, the previously found range for  $[D^*]$  is optimized with respect to the other experimentally obtained natural frequencies, such that all of the natural frequencies are matching instead of only the first one. This leads to us obtaining an optimized  $[D^*]$ , which can be used in the next step. This optimized  $[D^*]$  is then used in an artificial neural network that correlates the ply orientations to  $[D^*]$ , to obtain the ply orientations. The artificial neural network is then iterated, searching for ply orientations with subsequently smaller search ranges, until the ply orientations are converged.

Although final ply orientations are obtained at the end of this flowchart, due to the usage of artificial neural networks, the entire flowchart must be iterated several times to ensure the convergence of the ply orientations. Although a converged solution for the neural network employed, the output ply orientations may not always be suitable for the laminate. Therefore, repeating the process several times and comparing the outcomes helps assess any outlier solution occurring.

In the following sections, the process described in Figure 3.4 are explained in detail. The sections are divided into parts, each explaining a step shown in this figure.

### **3.2.1 Obtaining Laminate Property Range from Test Data**

Natural frequencies for a composite laminate depend on many different elastic constants as opposed to isotropic materials, which are only influenced by Young's modulus and Poisson's ratio. Hence, different combinations of elastic properties may yield the same natural frequency. The objective of this section is to assess a range

for the elastic properties defined in the  $[ABD]$  matrix so that it may later be used for identification of the laminate.

For plate type of structures, a single reduced bending stiffness matrix may be defined to express the entire stiffness characteristic of the laminate for calculation of natural frequencies [70]. This reduced bending stiffness is defined in terms of elements of  $[ABD]$  matrix. The reduced bending stiffness matrix may be defined as:

$$[D^*] = [D] - [B][A]^{-1}[B] \quad (3.17)$$

Although mostly useful for plates, this matrix can also be used for other complex geometries to define a unique approximate bending stiffness behavior for the laminate in presence of extension bending coupling. For an orthotropic material, this matrix only contains 4 elements, namely  $D_{11}^*$ ,  $D_{22}^*$ ,  $D_{12}^*$ , and  $D_{66}^*$ . These quantities will later be used as parameters to identify the laminate stiffness. These parameters are selected as  $D_{11}^*$ ,  $D_{22}^*$ , and  $0.5D_{12}^* + D_{66}^*$ , reducing the number of parameters to 3. These parameters are called  $D^*$  parameters.

The reason these  $D^*$  parameters are employed in this process is due to their usage in direct estimation of natural frequencies for a plate type structure [70]. Therefore, it was expected that such parameters must govern the change in natural frequencies for more complex geometries as well. The parameters were chosen by the fact that to obtain the natural frequencies, the elastic constants  $D_{11}^*$ ,  $D_{22}^*$ , and  $0.5D_{12}^* + D_{66}^*$  are multiplied with other parameters related to the mode shapes. Therefore, 3 parameters were deemed enough.

From equations (3.11) and (3.14 – 3.16) it can be readily seen that these selected parameters depend on the ply orientations of the laminate. Hence, for each individual laminate configuration, a different set of  $D^*$  parameters exist. The difference in these parameters result in different natural frequencies for the structure. Therefore, using either an analytical, semi-analytical, or numerical method to compute natural frequencies for these unique layups, one can construct a diagram of  $D^*$  parameters versus natural frequency. An example of this chart is shown in Figure 3.5. This figure

must be constructed 3 times, for each  $D^*$  parameter:  $D_{11}^*$ ,  $D_{22}^*$ , and  $0.5D_{12}^* + D_{66}^*$  versus natural frequency.

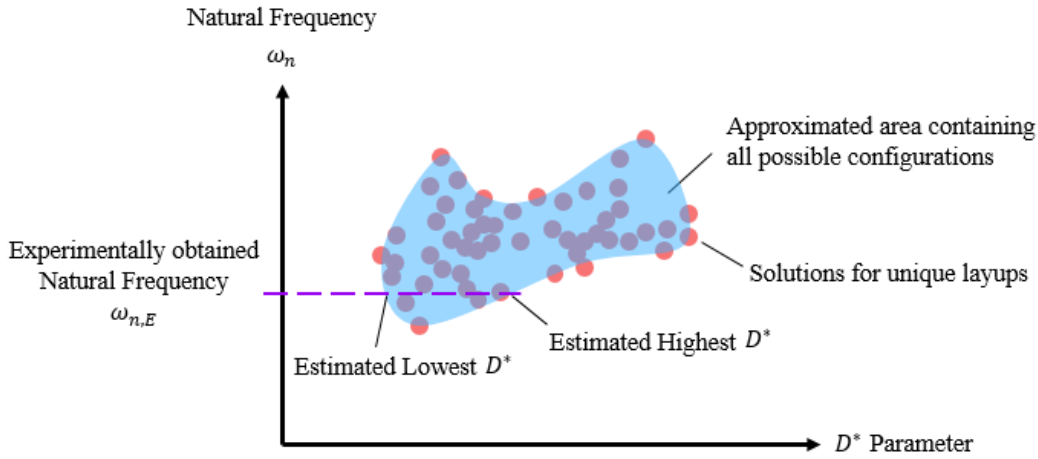


Figure 3.5 Estimated area constructed from unique data points estimated to contain all possible layup configurations

Since the natural frequencies of the unknown laminate are experimentally obtained, this chart can be used to obtain a range for the  $D^*$  parameters. Theoretically, any  $D^*$  selected within these boundaries defined should satisfy the natural frequency. However, when selected at random, different  $D^*$  parameters may not be constructing a physical setup. A primitive example of this case would be setting both  $D_{11}^*$  and  $D_{22}^*$  to their highest possible value, indicating that the laminate is unidirectional and both global  $x$  and  $y$  directions are the fiber directions for each ply. This case cannot be realized physically. In the following sections, this problem is assessed for the selection of  $D^*$  parameters to always realize a physical configuration.

From Figure 3.5 it can be inferred that several different  $D^*$  parameters set can be relating to the same natural frequencies. However, if the other natural frequencies are also considered, it can be shown that two different laminates cannot refer to the same set of natural frequencies. The only exception to this case is the presence of symmetry, in which case symmetric structures may yield the same natural frequency set. Such an example would be a square plate.



### 3.2.2 Optimization of Laminate Properties

Previously, a range of  $D^*$  parameters was defined considering a single natural frequency. However, a different range might be obtained when another natural frequency is considered. Therefore, considering all experimentally obtained natural frequencies, the previously obtained range can be optimized to find a singular value for the  $D^*$  constants that match all natural frequencies at once. Therefore, a method must be used to obtain natural frequencies given the  $D^*$  parameters, so the calculated and experimentally obtained natural frequencies can be optimized. Therefore, some formulation of process is required to obtain the natural frequencies given the ply layup or  $D^*$  parameters. Ways to obtain natural frequencies has been explained in detail in Appendix A for various geometries and cases.

When only a single natural frequency is considered as shown in the previous section, a range of  $D^*$  parameters is obtained. However, when multiple natural frequencies are considered, only one single set of  $D^*$  parameters should satisfy all the natural frequencies. Therefore, the  $D^*$  parameters range should be optimized against all measured natural frequencies. However, if done blindly, we need to optimize the  $D^*$  parameters in a 3D space, which may yield to a set that cannot satisfy the existence of a physical laminate. In the following section, more information on the optimization scheme and how to reduce the problem into a 1D optimization is presented.

Once the natural frequencies are obtained, calculated natural frequencies from a set of  $D^*$  parameters can be optimized against the experimentally obtained ones in a multi-input, multi-output optimization setup. However, considering physical properties of the system, the problem can be reduced to a single input single output optimization problem.

Equations (3.14 – 3.16) can be modified considering a change of  $P$  number of plies in the laminate as

$$[A] = \sum_{n=1}^N [Q_{global}]_n (z_{n+1} - z_n) - \sum_{k=1}^P \left( [Q_{global}]_k - [\bar{Q}_{global}]_k \right) (z_{k+1} - z_k) \quad (3.18)$$

$$[B] = \frac{1}{2} \sum_{n=1}^N [Q_{global}]_n (z_{n+1}^2 - z_n^2) - \frac{1}{2} \sum_{k=1}^P \left( [Q_{global}]_k - [\bar{Q}_{global}]_k \right) (z_{k+1}^2 - z_k^2) \quad (3.19)$$

$$[D] = \frac{1}{3} \sum_{n=1}^N [Q_{global}]_n (z_{n+1}^3 - z_n^3) - \frac{1}{3} \sum_{k=1}^P \left( [Q_{global}]_k - [\bar{Q}_{global}]_k \right) (z_{k+1}^3 - z_k^3) \quad (3.20)$$

Where  $[\bar{Q}_{global}]$  is the inverse of compliance matrix in global coordinate system for the altered ply in the laminate.

Equations (3.18 – 3.20) imply that any orientation change of any number of plies in the laminate will alter the matrices  $[A]$ ,  $[B]$ , and  $[D]$  in the same form a single ply constructs these matrices depending on its orientation. Therefore,  $D^*$  parameters alter in the same way between their maximum and minimum values as a single ply's function forms as shown in Figure 3.6.

This means,  $D^*$  parameters in fact can be governed by a single parameter, called equivalent angle for the entire laminate. Any physical change to the laminate in terms of ply orientations must correspond to a value of equivalent angle.

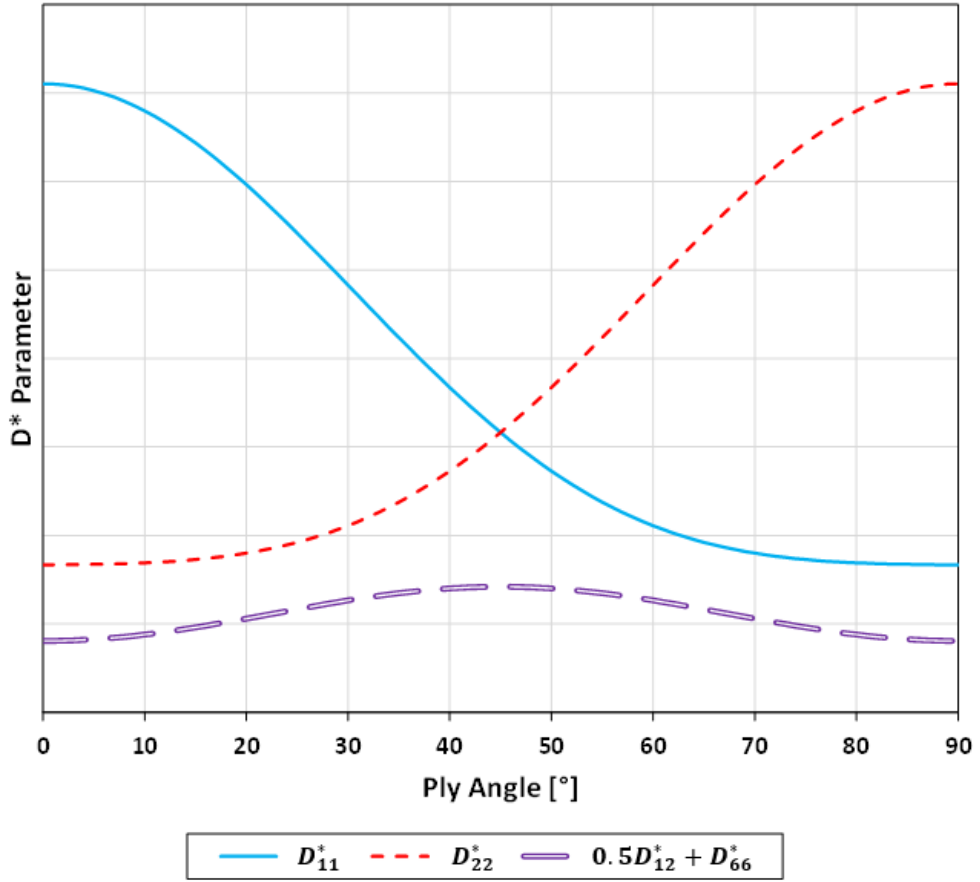


Figure 3.6 Change of  $D^*$  parameters for a single ply

Using the function forms presented in Figure 3.6 combined with the  $D^*$  parameter ranges previously obtained, the optimization problem can be reduced to a single input that is the equivalent angle. However, there are still multiple outputs that has to be optimized. Since all of them have to be optimized at the same time, absolute error between calculated and experimentally obtained natural frequencies can be optimized as the output. This error is shown below as

$$Absolute\ Total\ D^*\ Error = \sum_{i=1} |\omega_{n,E}^i - \omega_{n,A}^i| \quad (3.21)$$

Where  $\omega_{n,E}^i$  is the  $i^{th}$  experimentally obtained natural frequency, and  $\omega_{n,A}^i$  is the  $i^{th}$  calculated natural frequency.

Equation (3.21) must be summed over all experimentally obtained natural frequencies. Therefore, Absolute total  $D^*$  error can be minimized with respect to equivalent angle of the laminate to obtain the best fit of  $D^*$  parameters, which can then be used to identify the ply orientations.

### 3.2.3 Optimization of Ply Properties

In section 3.2.2,  $D^*$  parameters were optimized in such a manner that all natural frequencies were matching for the unknown laminate and constructed model. However, as shown in equations (3.14 – 3.16), properties of each ply are summed over the entire laminate to obtain these  $D^*$  parameters. Hence, it is difficult to identify the exact stacking sequence of the laminate, as there might be multiple ply configurations that might yield the same or similar  $D^*$  parameters. A primitive example of this case is a square unidirectional laminate constructed only of  $0^\circ$  and  $90^\circ$  plies, as the square laminate is symmetric in both directions, the exact orientation of material in one direction or the other wouldn't matter.

Due to the complexity and nonlinearity of this optimization problem, an artificial neural network (ANN) is constructed using Matlab [71]. Although, the ANN has limitations as well depending on its training set. For a very large training set containing almost every possible ply configuration, the accuracy of ANN would be low. As opposed to this, a very tight training range for the ANN would yield very accurate results but then the exact searching area must be predicted beforehand. To assess this situation, several ANNs are trained with reduced search range one after another to converge to the exact laminate configuration. The initial ANNs trained with large range help estimate the general search area for the later used smaller training range ANNs, which can accurately find the ply orientation configuration within the area. This process is summarized in Figure 3.7.

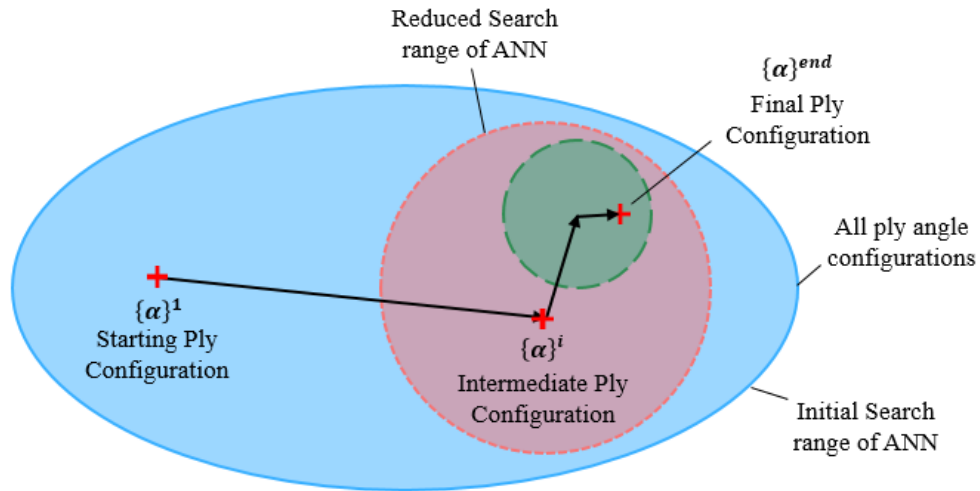


Figure 3.7 Optimization of ply properties by employing ANN subsequently on smaller search ranges

When the final ply orientations are obtained, the process defined in Figure 3.4 is finished. However, due to the nonlinearity of the process, this process should be run several times and then checked to see if the obtained ply layup configuration represents the experimentally obtained natural frequencies.

During the process of ANN, either a single or several plies might converge to an artificial solution. Running the process defined in Figure 3.4, and either averaging the solutions or getting rid of the outlier solutions helps assess these artificial solutions created by the nature of the solver. On top of this, the final ply orientations need to be cross-checked. Therefore, natural frequencies must be calculated from these ply orientations. If these calculated natural frequencies match with the experimentally obtained ones, then the procedure will be finished. Otherwise, more runs of the process defined in Figure 3.4 must be completed to assess the errors of the ply orientations. To correctly assess the ply orientations, number of runs are selected as 5. In case of nonmatching experimental and calculated natural frequencies, more are to be calculated until changes in ply orientations or outlier solutions are visible.

Previously in literature, ANN has been used to estimate fiber orientations given CT images of specimens [60]. Other than that, as mentioned in the literature survey,

orientations of fibers are usually obtained from micrographs from CT by analyzing image data. Hence, given the complexity of the problem, an ANN was chosen to optimize the ply configuration given the dataset for the laminate properties.

In this study, similar to their implementation [60], a 2 hidden layer ANN is employed. First layer employs 10 neurons with a “purelin” transfer function. The second layer employs 50 neurons with a “logsig” transfer function. The choice of these transfer functions was made by employing a transfer function combination that can assess a single ply correctly within  $0^\circ$  to  $90^\circ$  ply orientation. The output layer is chosen as a “logsig” function as well. Usage of “logsig” function is necessary for optimization of highly nonlinear problems. However, this function ranges values from 0 to 1. The first “purelin” layer, employing a range from -1 to 1, converts the range of this nonlinear function to -1 to 1.

The ANN uses 3 inputs as the  $D^*$  parameters, which are  $D_{11}^*$ ,  $D_{22}^*$ , and  $0.5D_{12}^* + D_{66}^*$ . The dataset for the ANN is divided randomly with distributions 50% for training, 35% for validation, and 15% for testing. Validation checks for the ANN are set to 10. Maximum of 1000 epochs are allowed which is standard. Training algorithm was chosen as Levenberg-Marquardt which is the standard setting. Performance criteria was based on mean squared error.

The output of the ANN is a vector set of ply orientations. As shown in Figure 3.4, obtained ply orientations must converge before the process is terminated. If convergence of the ply orientations is not satisfied, a new ANN is trained with a new search radius and center as shown in Figure 3.7, and the process is iterated.

Initially, ANN is trained at a set that contains all possible ply layup configurations. Therefore, accuracy of this ANN is low, and without proper reduced range searches afterwards, the entire process might diverge. Therefore, the reduction of search range for ply angles must be applied gradually.

Initially, the search must start from either the healthy configuration that has a ply configuration that was desired to be produced, and the search range should cover all

possible layups from  $-90^\circ$  to  $90^\circ$ . Then, a solution is obtained through ANN as  $\{\alpha\}^i$ . Initially, the search range was  $180^\circ$  for each ply assuming center at  $0^\circ$ , but now the search shall be centered around  $\{\alpha\}^i$ , and the range should be reduced. The new lower and upper bounds for the search are selected as

$$\alpha_{Lower}^{i+1} = \alpha_{Lower}^i + \frac{\alpha_{Upper}^i - \alpha_{Lower}^i}{2 + i} \quad (3.22)$$

$$\alpha_{Upper}^{i+1} = \alpha_{Upper}^i - \frac{\alpha_{Upper}^i - \alpha_{Lower}^i}{2 + i} \quad (3.23)$$

Where  $\alpha_{Lower}^i$  and  $\alpha_{Upper}^i$  are the lower and upper bounds for search range of the current step, and  $\alpha_{Lower}^{i+1}$  and  $\alpha_{Upper}^{i+1}$  are the lower and upper bounds for the search range for the next step, calculated from the current step. These equations are defined for each ply in the laminate.

Equations (3.22) and (3.23) slow down the reduction of search range as the iterations progress, so that after many iterations the search range doesn't reduce too much to affect the solutions of the ANN. In such cases, ANN can fit to a very small data range, extrapolating its solution, and finding arbitrary points as results.

Convergence of the results are based on the previous solution obtained through an ANN trained at a larger range. An absolute total ply angle difference is defined as

$$Absolute\ Total\ Ply\ Angle\ Difference = \sum_{k=1} |\alpha_k^{i+1} - \alpha_k^i| \quad (3.24)$$

Where the summation is summed over all plies in the laminate.

Realistically, a resolution of  $5^\circ$  for identification of each ply is acceptable, as lower angles may not be suitable measured, so this criterion is compared to the total ply angle error to establish the convergence of the process.

In the following sections, the proposed methodology described above is validated through numerical simulations and experimental data.

### **3.3 Numerical Simulation Based Validation of Ply Layup Identification Method**

It is fundamental to evaluate the performance of a proposed method. It is also best to do so by using data obtained through experiments and tests. However, doing so might be time consuming, costly, and not always possible. Therefore, as a first step, validation through numerical simulations is used. This way, the method can be evaluated at a much larger dataset which may provide more insight on its strengths and weaknesses.

In this section, results for numerically simulated cases and applied method are given. First, a healthy configuration is assumed. Then, a defected configuration is constructed that has different ply orientations compared to the healthy one. The method described in this chapter is then applied using the natural frequencies of the defected structure as input to estimate the ply orientations. Results are given for different geometries in each individual section.

For all cases considered, a finite element analysis is employed to generate the defected setups using Abaqus [72]. In these analysis, composite parts are modelled as shells and composite layups are used to generate the plies and orientations. Reduced integration quadratic quadrilateral elements (S8R) were chosen to best represent the stiffness. Material properties are defined as engineering constants, providing orthotropic material constants. Lanczos solver is used.

Due to the length of the process and the number of cases considered, only one case for each geometry is explained in detail in all of its calculation steps. For the rest of the cases, the outcome results are given and discussed, as shown below.



### 3.3.1 Numerical Simulation Based Validation for Plate Structures

In this section, effects of geometric dimensions, total ply number, various bending and axial stiffness differences, unbalanced laminates, boundary condition are studied. Configurations in Table 3.1 were considered to assess these effects.

Table 3.1 Considered configurations for plate geometry

Name	Ply Configuration	Size [mm x mm]	Boundary Condition
P_C1_S1_B1	[0] <sub>8</sub>	225x225	SSSS
P_C1_S2_B1	[0] <sub>8</sub>	100x100	SSSS
P_C1_S1_B2	[0] <sub>8</sub>	225x225	FFFF
P_C2_S1_B1	[±45] <sub>4</sub>	225x225	SSSS
P_C3_S1_B1	[±15/±70/±20]	225x225	SSSS
P_C4_S1_B1	[0 <sub>2</sub> /±45/90 <sub>2</sub> ]	225x225	SSSS
P_C5_S1_B1	[±20] <sub>3</sub>	225x225	SSSS
P_C6_S1_B1	[±25/±27/±28]	225x225	SSSS
P_C2_S2_B2	[±45] <sub>4</sub>	100x100	FFFF
P_C7_S2_B2	[±45/0 <sub>4</sub> /±45]	100x100	FFFF
P_C8_S2_B2	[0 <sub>2</sub> /±45 <sub>2</sub> /0 <sub>2</sub> ]	100x100	FFFF
P_C9_S2_B2	[0 <sub>2</sub> /±45/0 <sub>2</sub> /±45]	100x100	FFFF

In Table 3.1, the naming convention is as follows. Since all of these are plate structures their naming starts with a “P”. Followed by the ply orientation configuration denoted by C, followed by a number for different layups. Then, S is used for size, and B is used for the boundary conditions, both taking numbers for different setups. SSSS boundary conditions are representing a simply supported boundary condition for all edges, and FFFF represent all edges having free boundary conditions. P\_C1\_S1\_B1 is chosen as the baseline for all comparison. P\_C1\_S2\_B1 was chosen to establish the effect of difference in geometric dimensions. P\_C1\_S1\_B2 was chosen to inspect the effect of a different boundary condition.

P\_C2\_S1\_B1 was chosen to study the difference in defected ply orientations, in this case presenting the highest shear stiffness. P\_C3\_S1\_B1 was chosen to identify the effect of a non-repeating ply angle difference in the laminate. P\_C4\_S1\_B1 was chosen to study a relatively quasi-isotropic laminate with equal increments for ply angle difference. P\_C5\_S1\_B1 was chosen to see the effect of a unidirectional laminate that does not align with the global coordinates. P\_C6\_B1\_S1 was chosen to inspect the intricacies of the proposed method when the ply angles are very close to each other.

Rest of the cases presented in Table 3.1 are a bit different when compared to the others. These laminates are included as they are the ones that will be experimentally validated. For these laminates, P\_C2\_S2\_B2 can be seen as the baseline. P\_C7\_S2\_B2 presents a different axial stiffness compared to the baseline. P\_C8\_S2\_B2 presents the same axial stiffness as P\_C7\_S2\_B2 but has a different bending stiffness. These two configurations also employ the same plies in switched positions. P\_C9\_S2\_B2 also has the same number of plies and orientations compared to the prior, but it is unsymmetrical, leading to extension-bending coupling effects.

As described prior, only the case for P\_C1\_S1\_B1 will be explained in detail, while the results for others will be presented at the end of this section. Initially, assume an arbitrary healthy setup is given that does not have the ply orientations of P\_C1\_S1\_B1 case. Therefore, the modal analysis of this case is required to supplement natural frequencies to start the proposed method. Material properties for the composite material employed is given in Table 3.2.

Table 3.2 Material properties for the considered carbon epoxy composite system

Property	Value	Unit	Description
$E_{11}$	143800	MPa	Fiber direction modulus
$E_{22}, E_{33}$	5800	MPa	Transverse direction modulus
$\nu_{12}, \nu_{13}$	0.27	-	Fiber-transverse Poisson's ratio
$\nu_{23}$	0.38	-	Transverse in-plane Poisson's ratio
$G_{12}, G_{13}$	5200	MPa	Fiber-transverse shear modulus
$G_{23}$	2300	MPa	Transverse in-plane shear modulus
$\rho$	1520	kg m <sup>-3</sup>	Density

A total of 5625 elements were used for the model as shown in Figure 3.8. Pinned boundary conditions are used that simulate the case. First three natural frequencies obtained for this case are 124.7 Hz, 172.7 Hz, and 272.7 Hz. Mode shapes for these cases are shown in Figure 3.8. Then, the first natural frequency, 124.7 Hz, can be used to identify the range of the  $D^*$  parameters. The estimated regions for these  $D^*$  parameters are shown in Figure 3.9, Figure 3.10, and Figure 3.11. In the same figures, minimum and maximum values of the  $D^*$  parameters are identified. Then, using these parameters, an optimization of the other two natural frequencies is applied. The optimization problem was reduced to single input single output as described in section 3.2.2. The optimization scheme for  $D^*$  parameters with respect to the equivalent angle is shown in Figure 3.12. Starting  $D^*$  parameters and final optimized  $D^*$  parameters are also present on this figure.

Once the  $D^*$  parameters were optimized, these parameters are used in the ply angle optimization described in section 3.2.3. Output ply angles during the convergence of the process is presented in Table 3.3 for each step of the search range reduction. 4 sections in the laminate were considered for optimization process. In this table, the step number 0 is the ANN employed for the entire possible layup configurations. The process was terminated by the criterion given in section 3.2.3. Hence the final ply orientation configuration is obtained as  $[\pm 0.2/\pm 1.9/\pm 0.7/\pm 1.3]$ , while the target

configuration is  $[0]_8$ , which presents less than  $2^\circ$  angle error for every considered section in the laminate.

The process described in section 3.2.3 is iterated 4 more times, and the final ply orientations for case P\_C1\_S1\_B1 are presented in Table 3.4. This was to ensure the stability of ANN solution. The average of these 5 runs is assumed to be the definite ply orientation configuration of the defected laminate. The process described for P\_C1\_S1\_B1 is employed for the other configurations shown in Table 3.1, and the results are shown in Appendix B.

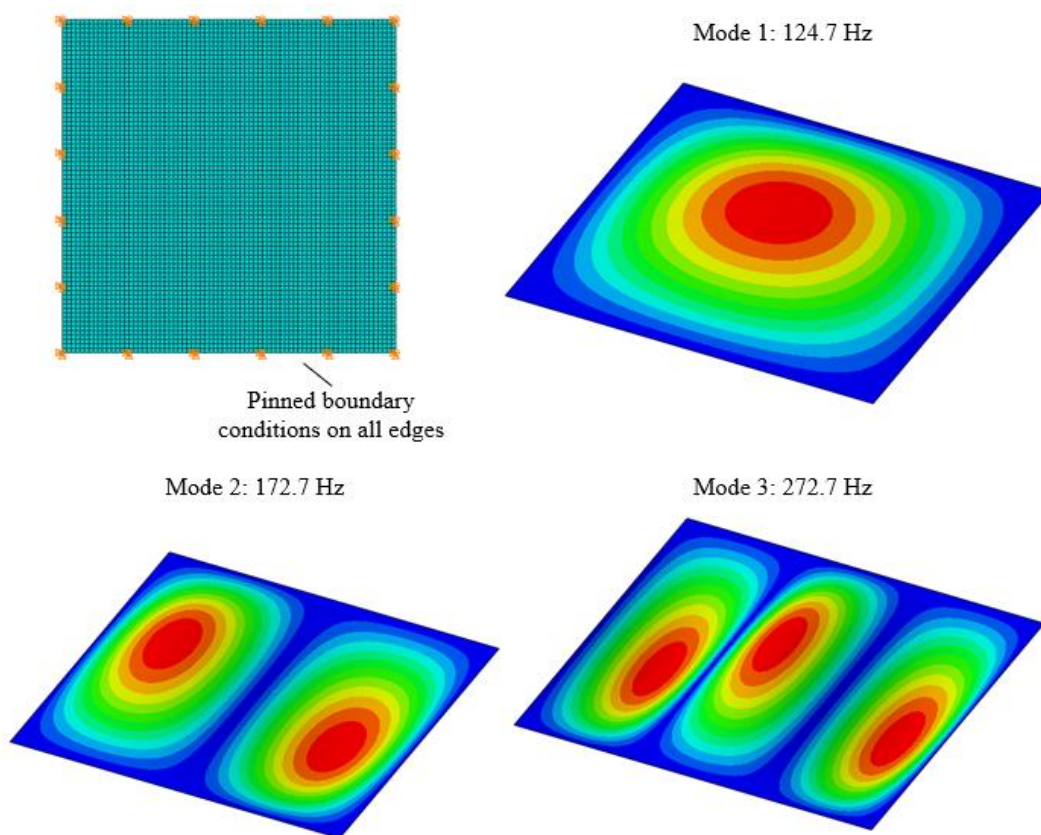


Figure 3.8 Finite element model and first three mode shapes for C1\_S1\_B1 case

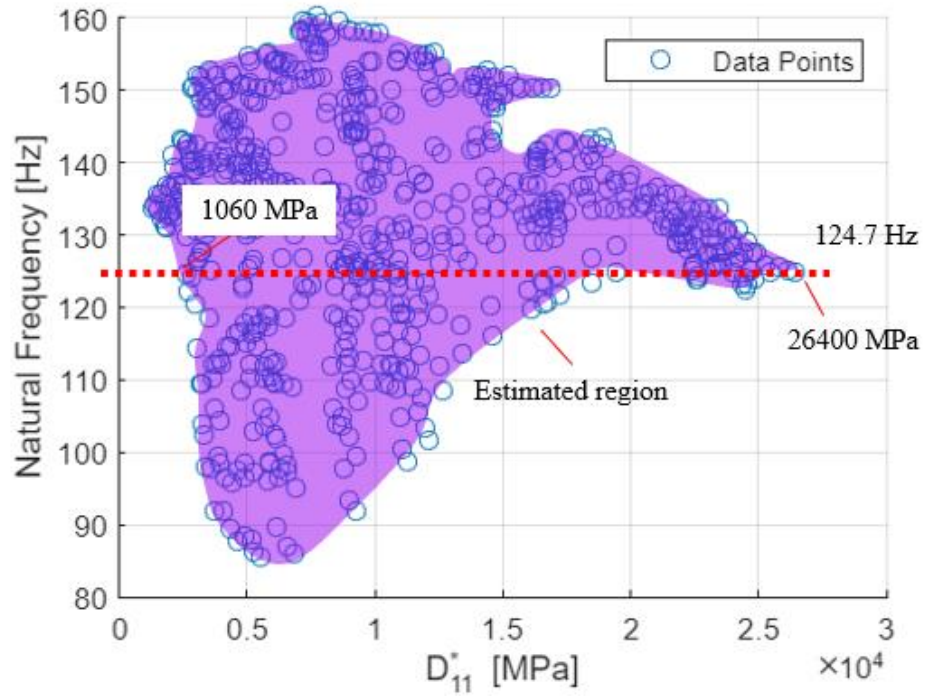


Figure 3.9 Estimated area for  $D_{11}^*$  and the boundary values for the considered first natural frequency

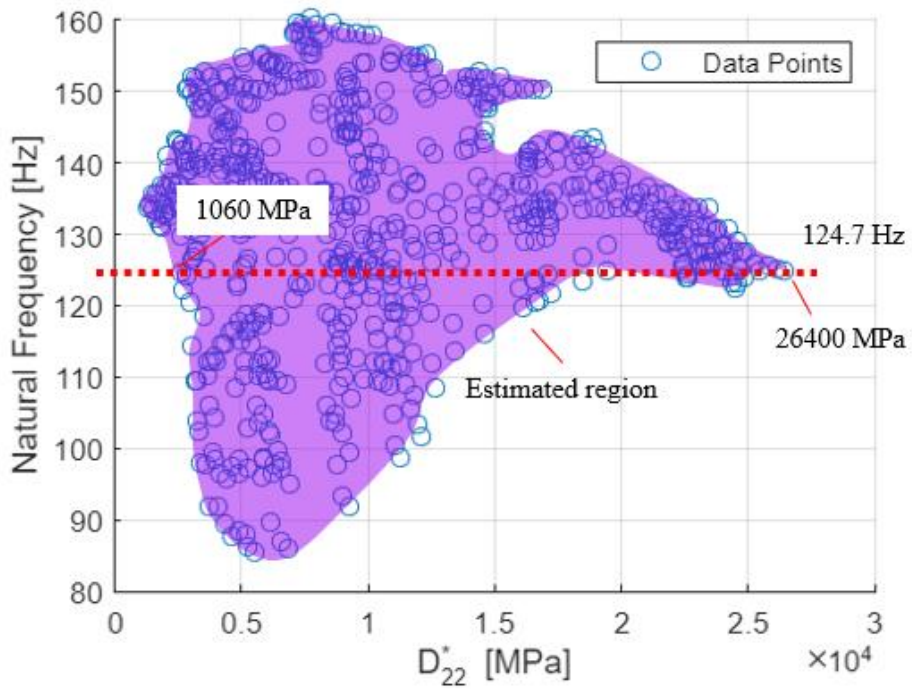


Figure 3.10 Estimated area for  $D_{22}^*$  and the boundary values for the considered first natural frequency

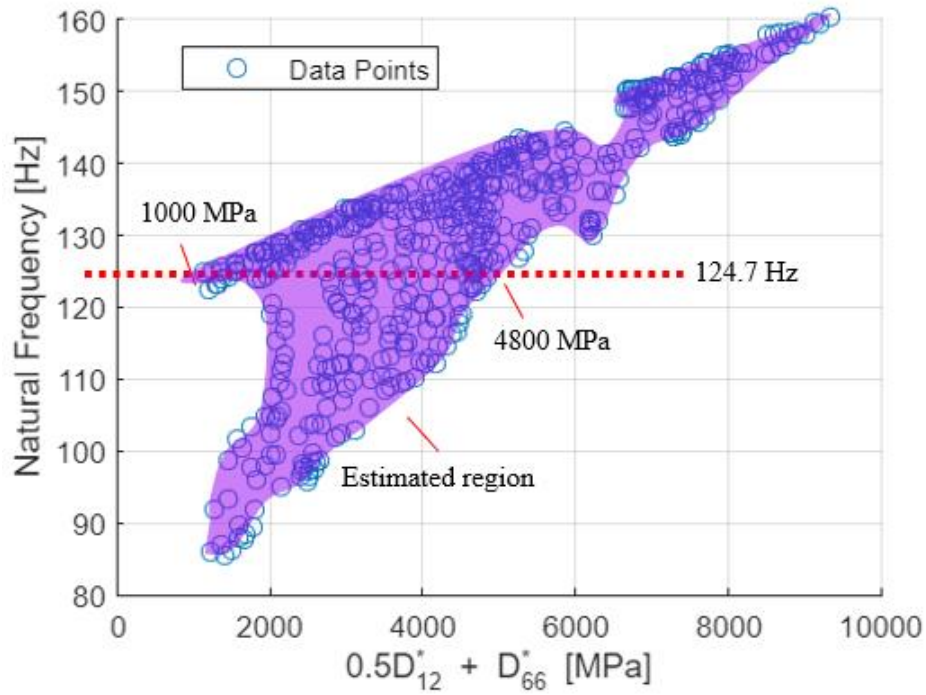


Figure 3.11 Estimated area for  $0.5D_{12}^* + D_{66}^*$  and the boundary values for the considered first natural frequency

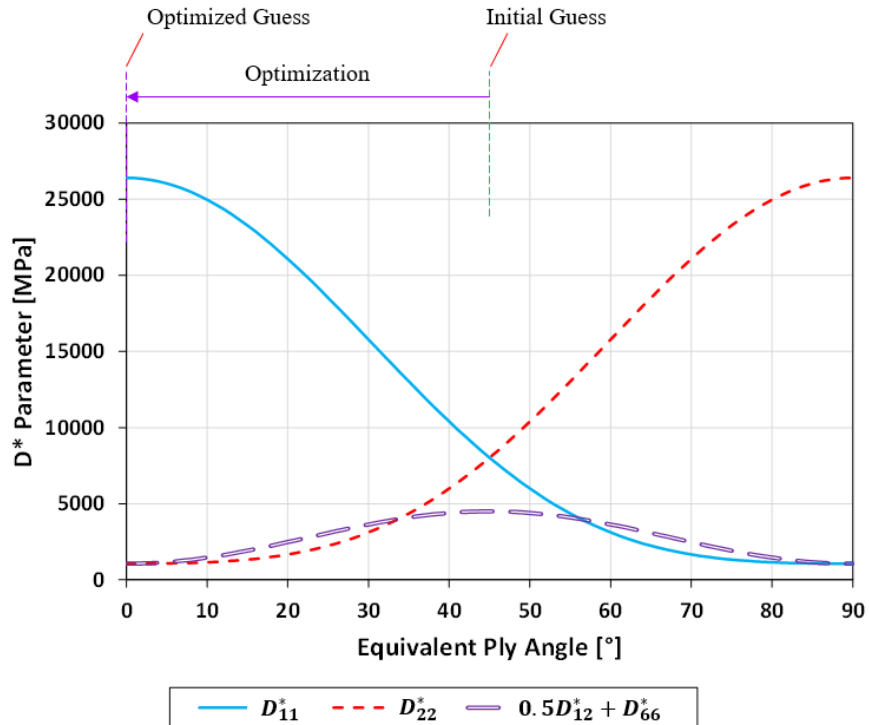


Figure 3.12 Optimization of  $D^*$  parameters given maximum and minimum values

Table 3.3 Ply orientations obtained through the optimization process with consequently reduced search range ANN for P\_C1\_S1\_B1 case

Step Number	Section 1	Section 2	Section 3	Section 4
0	[±45]	[±45]	[±45]	[±45]
1	[±17.2]	[±73.3]	[±45.2]	[±6.3]
2	[±8.2]	[±12.8]	[±26.1]	[±6.2]
3	[±4.2]	[±1.2]	[±3.9]	[±6.0]
4	[±0.2]	[±1.9]	[±0.7]	[±1.3]

Table 3.4 Results of the optimization runs for ply orientation identification for P\_C1\_S1\_B1 case

Optimization Run	Section 1	Section 2	Section 3	Section 4
1	[±0.2]	[±1.9]	[±0.7]	[±1.3]
2	[±1.8]	[±0.8]	[±1.6]	[±0.2]
3	[±2.3]	[±2.9]	[±0.4]	[±0.7]
4	[±1.0]	[±0.1]	[±0.5]	[±1.1]
5	[±0.4]	[±1.1]	[±1.7]	[±0.6]
Average	[±1.1]	[±1.4]	[±1.0]	[±0.8]
Target Layup	[0] <sub>2</sub>	[0] <sub>2</sub>	[0] <sub>2</sub>	[0] <sub>2</sub>

### 3.3.2 Numerical Simulation Based Validation for Cylindrical Structures

Just like the previous section for plate, validation for cylindrical structures are presented in this section. Since the effect of many parameters were exhaustively investigated in section 3.3.1, a smaller set of cases are considered for the cylindrical case, and for the later validation cases. Cases considered for the cylindrical structures are shown in Table 3.5.

Table 3.5 Considered configurations for cylindrical geometry

Name	Ply Configuration	Size [mm x mm]	Boundary Condition
C_C10_S3_B1	[±40]	R73x200	SSSS
C_C11_S4_B1	[90] <sub>2</sub>		SSSS
C_C10_S3_B2	[±40]		FFFF
C_C11_S4_B2	[90] <sub>2</sub>		FFFF

The naming convention used in Table 3.5 is the same as the one given in validation cases for plates in Table 3.1. The numbers in the naming convention were continued from the aforementioned table. The validation cases for cylindrical cases obtain a “C” preposition to denote that they are cylinders. As these are cylindrical geometries, the boundary conditions are only applied to the open ends of the cylinders.

Like the plate validations, only one case, namely C\_C10\_S3\_B1 will be shown in detail here, and the results for the other cases will be presented afterwards. For C\_C10\_S3\_B1, a finite element model is constructed employing 4784 reduced integration quadratic quadrilateral elements (S8R) on the cylindrical geometry as shown in Figure 3.13 along with the first few mode shapes. First three modes of this cylinder have 511.5 Hz, 517.1 Hz, and 579.8 Hz natural frequencies.

Like the validations for plate geometries, the estimated regions for these  $D^*$  parameters are shown in Figure 3.14, Figure 3.15, and Figure 3.16. It should be noticed in Figure 3.14 and Figure 3.15 that the search range is partitioned into two.



Therefore, both of these ranges need to be considered individually rather than using the global minimum and maximum ranges.  $D^*$  parameters range in Figure 3.14 is taken from 80 MPa to 200 MPa, and 60 MPa to 155 MPa for Figure 3.15 which do not necessarily correspond to global minimum and maximum values.

Similar to the validation of plates, optimization scheme for  $D^*$  parameters with respect to the equivalent angle is shown in Figure 3.17 and output ply angles during the convergence of the process are presented in Table 3.6 for each step of the search range reduction. Hence the final ply orientation configuration is obtained as  $[\pm 40.1]$ , while the target configuration is  $[\pm 40]$ , which presents  $0.1^\circ$  angle error in the laminate.

The process described in section 3.2.3 is iterated 4 more times, and the final ply orientations for case C\_C10\_S3\_B1 are presented in Table 3.7. The average of these 5 runs is assumed to be the definite ply orientation configuration of the defected laminate. The process described for C\_C10\_S3\_B1 is employed for the other configurations shown in Table 3.5, and the results are shown in Table 3.7 as well.

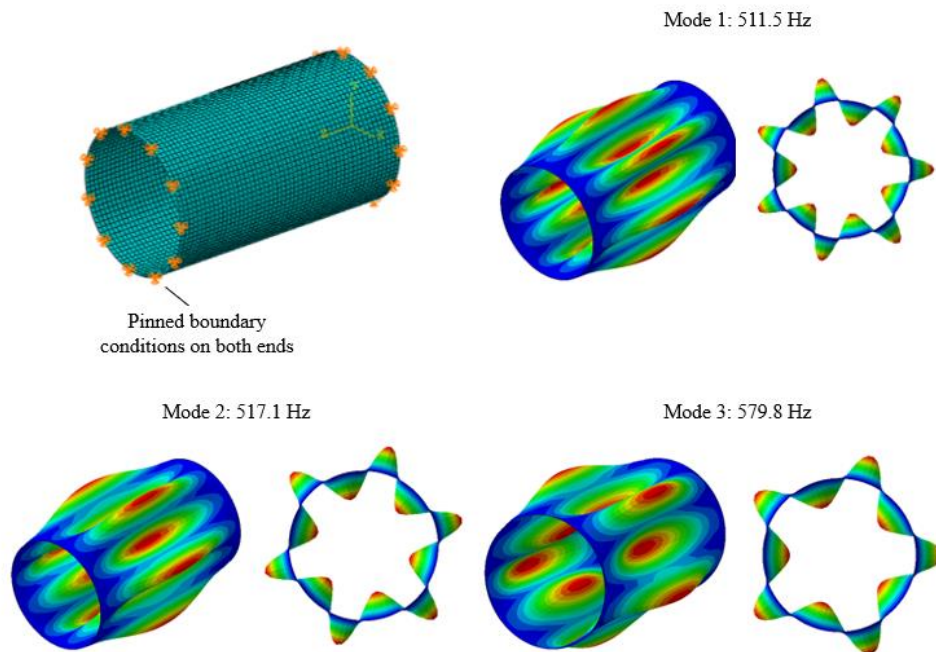


Figure 3.13 Finite element model and first three mode shapes of C\_C10\_S3\_B1 case

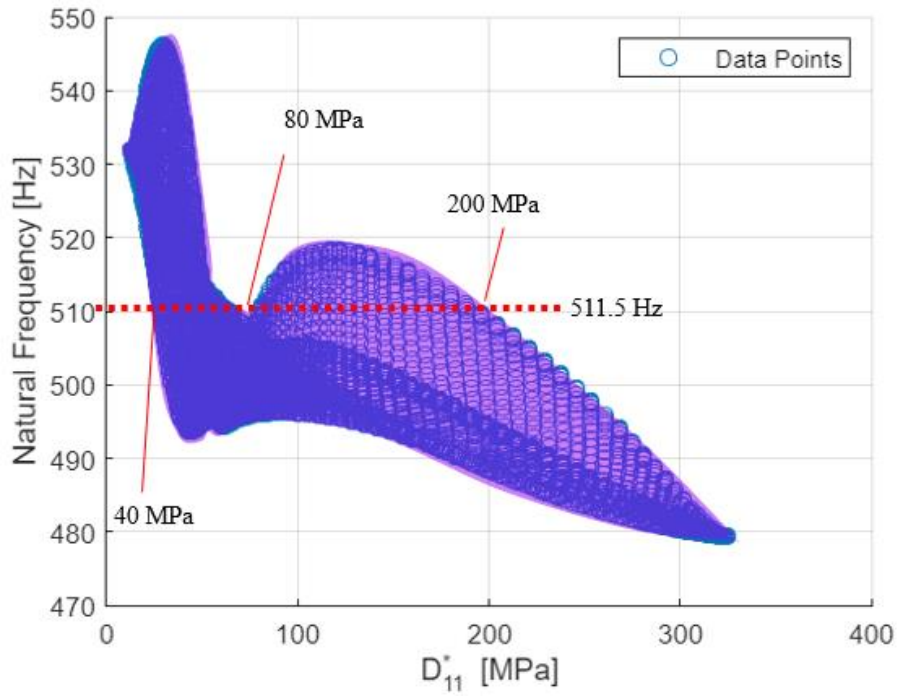


Figure 3.14 Estimated area for  $D_{11}^*$  and the boundary values for the considered first natural frequency

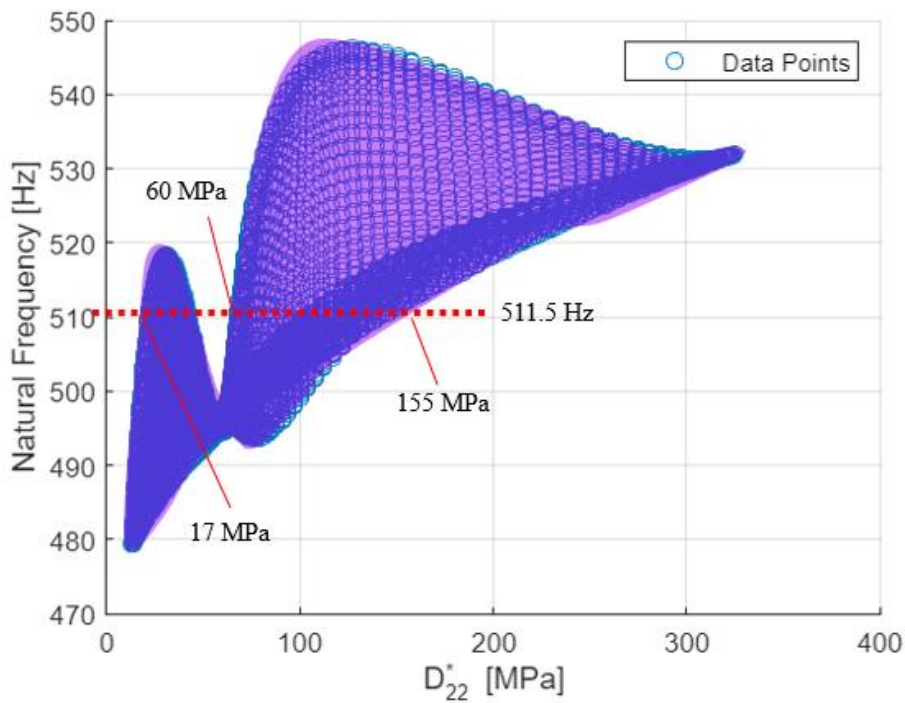


Figure 3.15 Estimated area for  $D_{22}^*$  and the boundary values for the considered first natural frequency

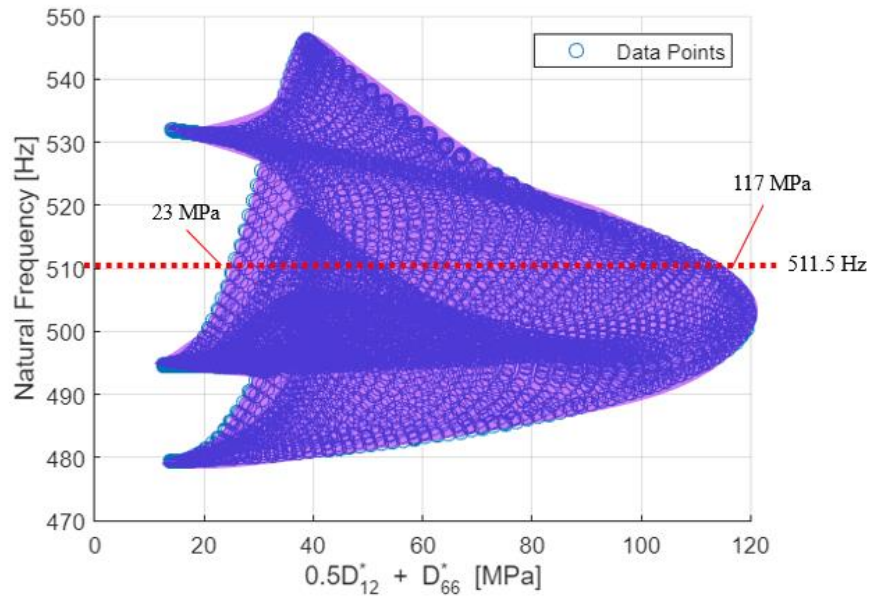


Figure 3.16 Estimated area for  $0.5D_{12}^* + D_{66}^*$  and the boundary values for the considered first natural frequency

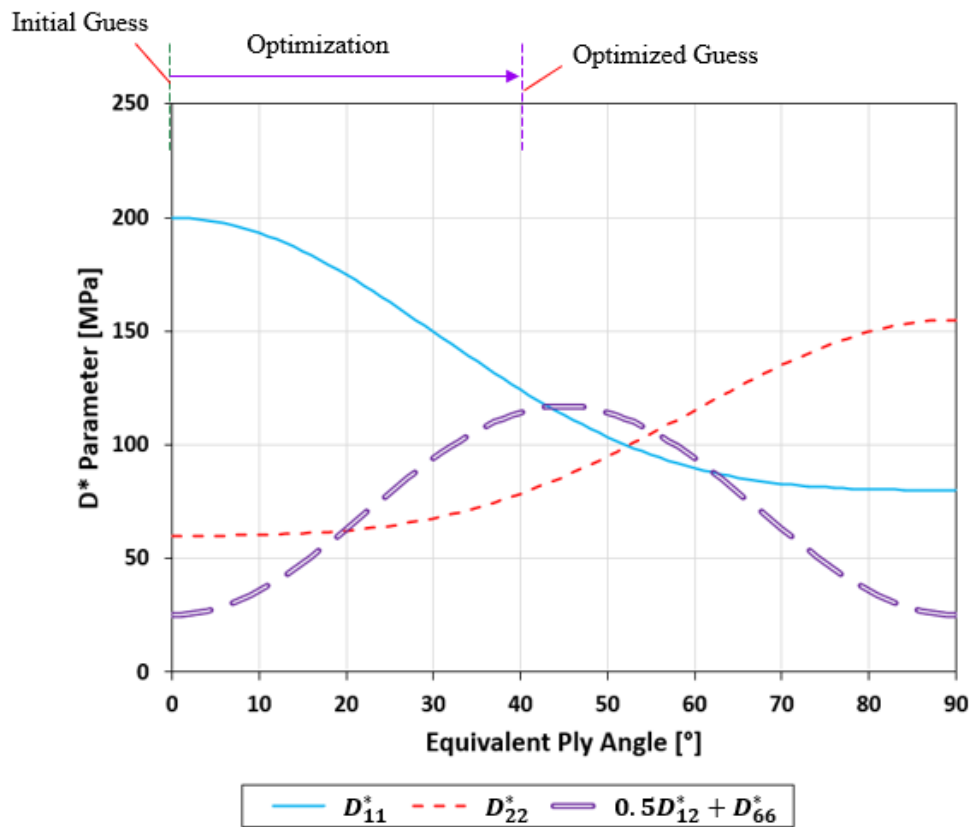


Figure 3.17 Optimization of  $D^*$  parameters given maximum and minimum values

Table 3.6 Ply orientations obtained through the optimization process with consequently reduced search range ANN for C\_C10\_S3\_B1 case

Step Number	Ply Angle [°]
0	[0] <sub>2</sub>
1	[±67.2]
2	[±54.6]
3	[±46.1]
4	[±40.7]
5	[±40.1]

Table 3.7 Results of the optimization runs for ply orientation identification for all cylindrical geometry cases considered

Optimization Run	C_C10_S3_B1	C_C11_S4_B1	C_C10_S3_B2	C_C11_S4_B2
1	[±40.1]	[±92.4]	[±40.3]	[±91.9]
2	[±38.1]	[±89.9]	[±39.1]	[±87.2]
3	[±46.7]	[±86.2]	[±42.4]	[±87.3]
4	[±42.8]	[±95.0]	[±35.3]	[±86.2]
5	[±45.1]	[±94.8]	[±44.2]	[±86.8]
Average	[±42.5]	[±91.7]	[±40.3]	[±87.9]
Target Layup	[±40.0]	[90] <sub>2</sub>	[±40.0]	[90] <sub>2</sub>

### 3.3.3 Numerical Simulation Based Validation for Pressure Vessel Structures

In this section, validation of a complex geometry such as a pressure vessel is presented. Previously, the geometries were rather simpler so to generate the calculated natural frequencies, a continuous system model could be used. However, pressure vessels are complex enough to warrant a better performance for obtaining

natural frequencies through finite element analysis. Therefore, the estimated area of all possible configurations is drawn from finite element analysis results.

Geometric dimensions of the pressure vessel considered for this case is presented in Figure 3.18. In this study the pressure vessel is employed without the end caps. In sections 3.3.1 and 3.3.2 various cases were considered for validation, so in this section a smaller set of cases are studied that can represent the ply configuration errors in pressure vessels the best. There are mainly two winding sets for filament wound pressure vessels, hoop winding (O) and helical winding (X). Unlike helical winding, hoop winding can only cover the cylindrical part of the pressure vessel, hence its effective domain is limited considering the entire geometry. The winding angle of helical winding is usually fixed due to geometric constraints, but due to fiber slippage it may vary around the geodesic path a little [73-75].

Considered cases for these numerical simulations are presented in Table 3.8. In this table, cases are taken “PV” prefix to denote that they are pressure vessels. For all helical windings, geodesic path was assumed employing close to 40° angle, varying a bit depending on the current ply position. PV\_C12\_S4\_B2 case is studied to validate the model for a configuration that affects the pressure vessel entire. PV\_C13\_S4\_B2 adds a hoop layer in between the helical ones, presenting a case where the layup doesn’t fully cover the pressure vessel. PV\_C14\_S4\_B2 is chosen to assess if the proposed method can reliably detect the position of individual plies, since in this case the hoop winding’s position is changed compared to PV\_C13\_S4\_B2.

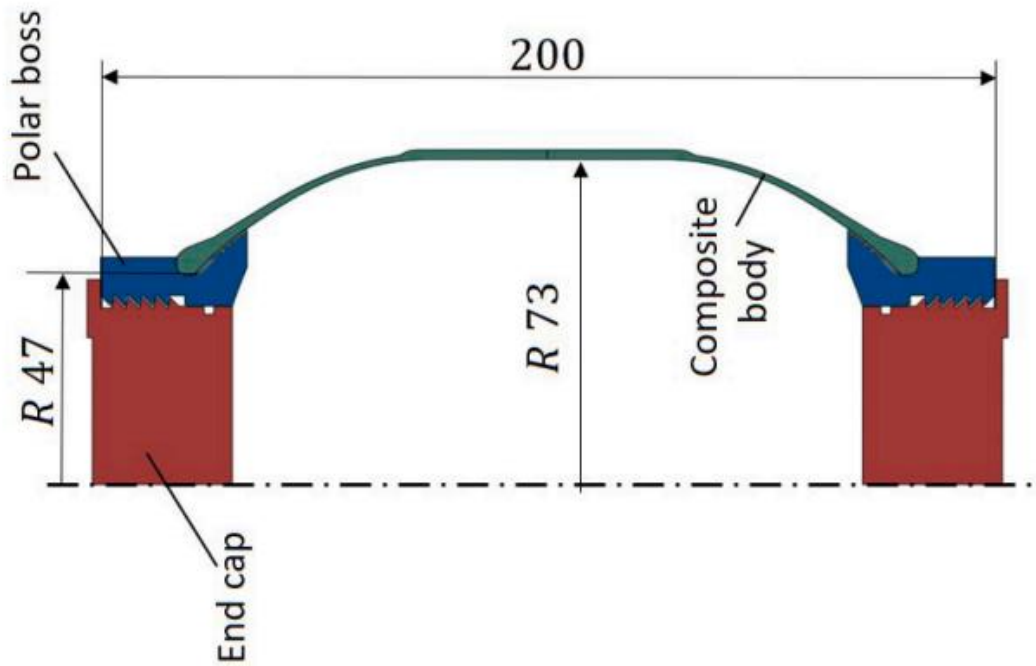


Figure 3.18 Considered pressure vessel geometry for numerical simulation based validation of the proposed method [76]

Table 3.8 Considered configurations for pressure vessel geometry

Name	Ply Configuration	Size	Boundary Condition
PV_C12_S4_B2	<i>XX</i>		
PV_C13_S4_B2	<i>XOX</i>	Figure 3.20	FFFF
PV_C14_S4_B2	<i>XXO</i>		

Just as the previous numerical simulation-based validations, only one case, namely PV\_C12\_S4\_B2, will be presented in detail here. The results for other cases will be presented at the end of the section. For PV\_C12\_S4\_B2, a finite element model is constructed employing a total of 61892 elements on the pressure vessel. 8000 of these were used to construct the shell geometry of the composite body, of type S8R. Rest of the elements were used to construct the aluminum polar bosses with C3D8R elements. The constructed model along with the first three mode shapes is shown in Figure 3.19. First three natural frequencies are 1309 Hz, 1801 Hz, and 2370 Hz.

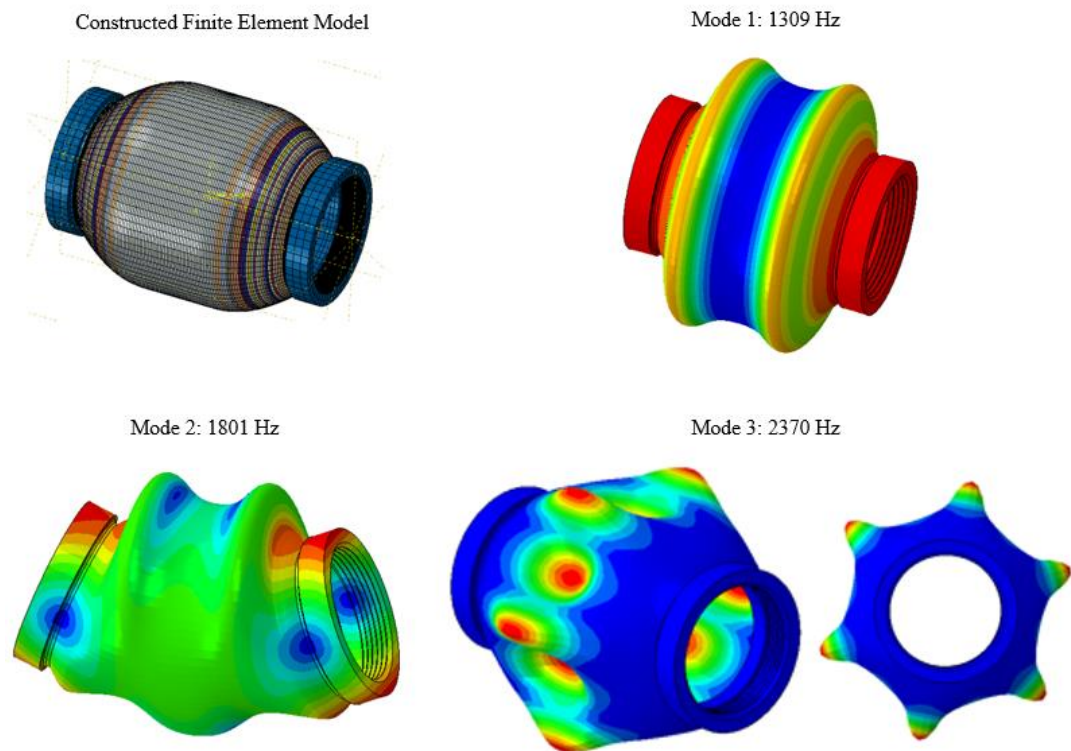


Figure 3.19 Finite element model and first three mode shapes of PV\_C12\_S4\_B2 case

Like the validations for plate and cylindrical geometries, the estimated regions for these  $D^*$  parameters are shown in Figure 3.20, Figure 3.21, and Figure 3.22. These charts were constructed using the valid ply angle errors possible in the laminate, so not all configurations were considered. It should be noted that there are two estimated areas in these figures. These areas were separated by the fact that estimated region 1 does not contain any hoop winding, and estimated region 2 contains hoop windings. The presence of a hoop winding significantly alters the natural frequencies, hence the search areas are divided to ensure more accurate  $D^*$  estimations.

Similar to the validation of plates and cylinders, optimization scheme for  $D^*$  parameters with respect to the equivalent angle is shown in Figure 3.23. Due to the physical constraints of the problem, the entire range of the figure is not usable. Instead, an angle difference centered around the nominal angle, or nominal equivalent angle for this case is considered. The entirety of the figure could be

considered if finite element analysis of pure 0° and pure hoop winding pressure vessels were included, however these vessels are either impossible to produce or impossible to construct geometrically. Both cases would not be able to cover the dome areas with composite material.

Output ply angles during the convergence of the process are presented in Table 3.9 for each step of the search range reduction. Hence the final ply orientation configuration is obtained as  $[\pm 40.9/\pm 38.9]$ , while the target configuration is  $[\pm 40]_2$ , which presents around 1° angle error in the laminate.

The process described in section 3.2.3 is iterated 4 more times, and the final ply orientations for case PV\_C12\_S4\_B2 are presented in Table 3.10. The average of these 5 runs is assumed to be the definite ply orientation configuration of the defected laminate. The process described for PV\_C12\_S4\_B2 is employed for the other configurations shown in Table 3.8, and the results are shown in Appendix B.

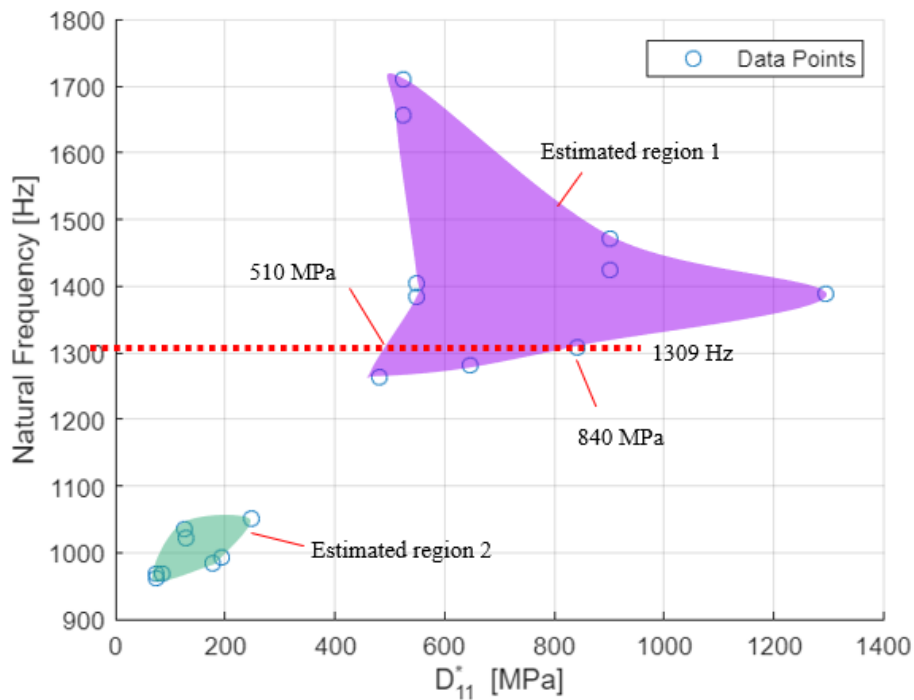


Figure 3.20 Estimated area for  $D_{11}^*$  and the boundary values for the considered first natural frequency



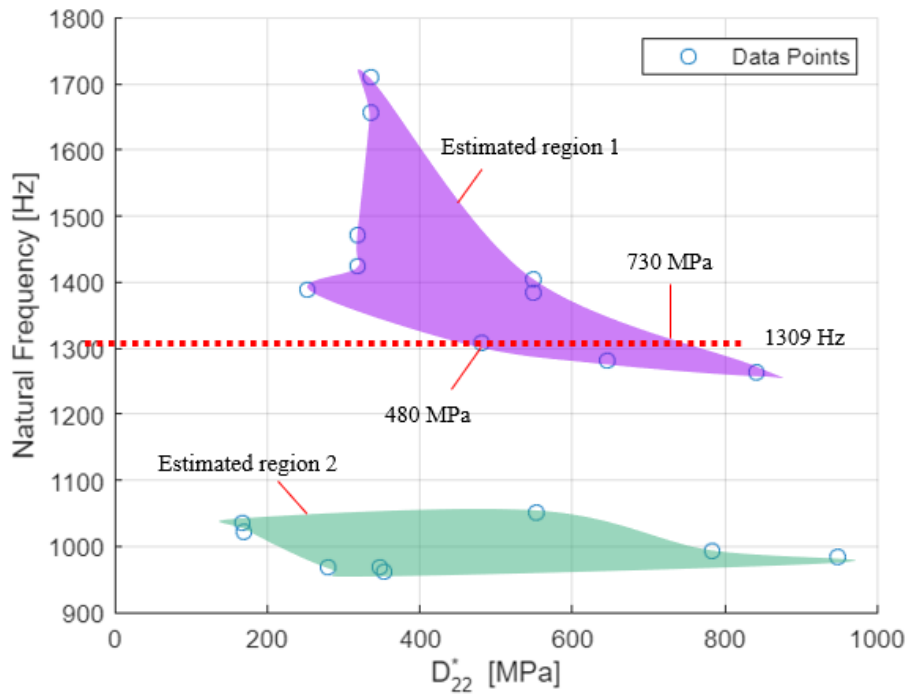


Figure 3.21 Estimated area for  $D_{22}^*$  and the boundary values for the considered first natural frequency

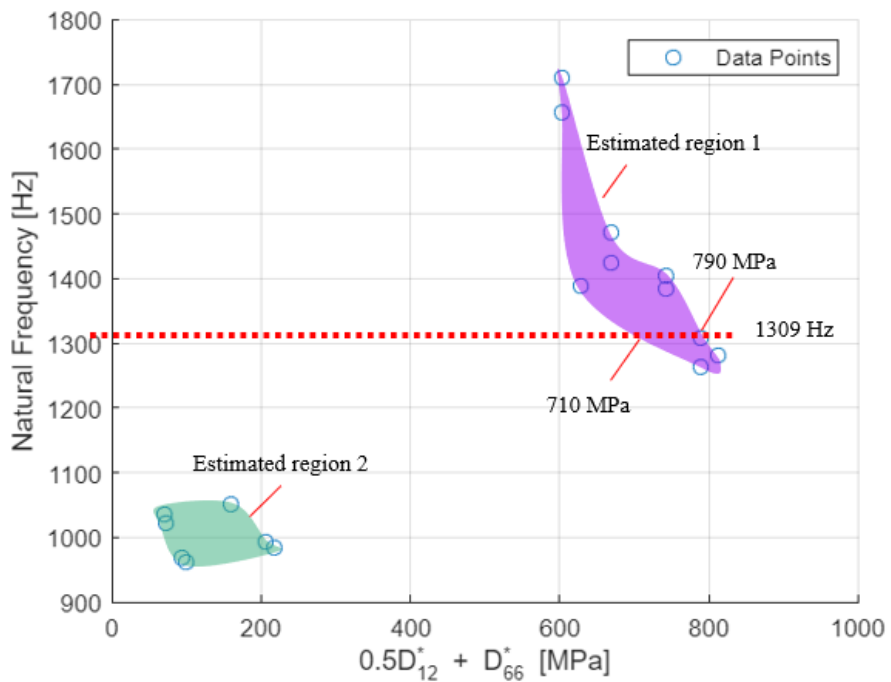


Figure 3.22 Estimated area for  $0.5D_{12}^* + D_{66}^*$  and the boundary values for the considered first natural frequency

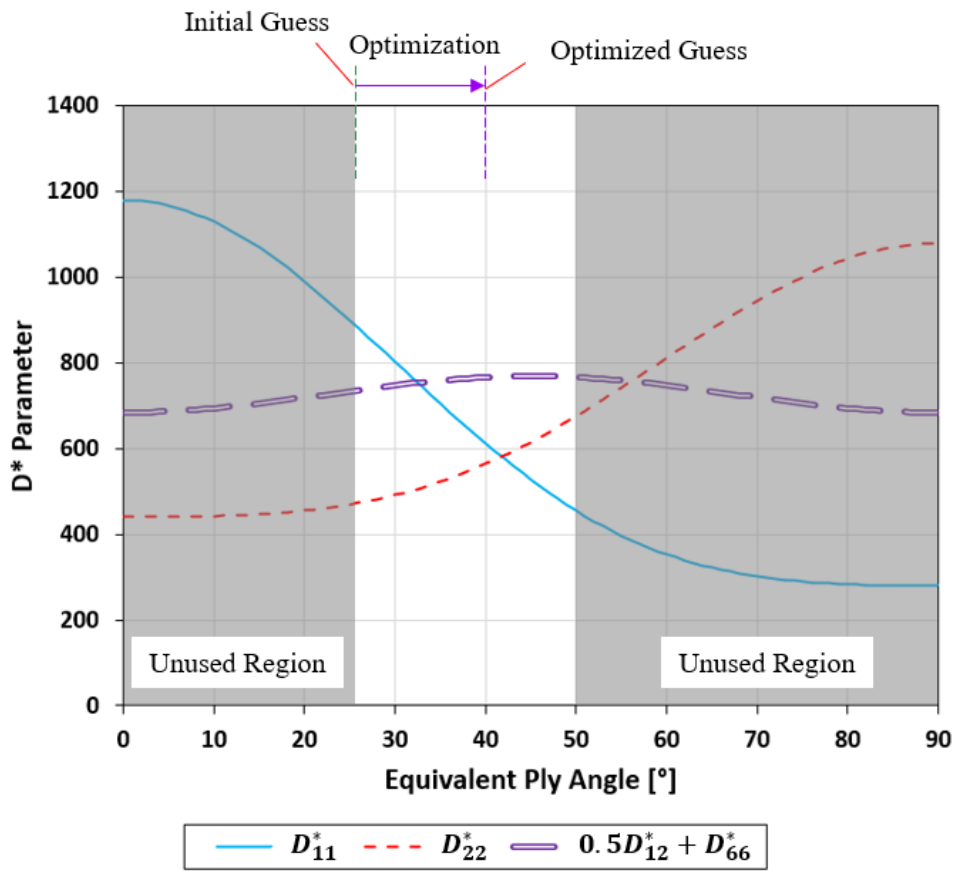


Figure 3.23 Optimization of  $D^*$  parameters given maximum and minimum values

Table 3.9 Ply orientations obtained through the optimization process with consequently reduced search range ANN for PV\_C12\_S4\_B2 case

Step Number	Section 1	Section 2
0	[±25]	[±25]
1	[±49.4]	[±32.6]
2	[±43.2]	[±41.1]
3	[±40.9]	[±38.9]

Table 3.10 Results of the optimization runs for ply orientation identification for PV\_C12\_S4\_B2 case

Optimization Run	Section 1	Section 2
1	[±40.9]	[±38.9]
2	[±43.5]	[±36.0]
3	[±40.7]	[±41.1]
4	[±42.9]	[±39.0]
5	[±38.7]	[±43.0]
Average	[±41.3]	[±39.6]
Target Layup	[±40]	[±40]

### 3.4 Experiment Based Validation of Ply Layup Identification Method

The proposed method was validated through numerical simulations prior. However, validation through only numerical simulations is not enough to completely validate the method. It would require some real case application, tests, or experiments to validate the method completely. Therefore, in this section, validation of the geometries considered for various produced parts are presented.

The proposed method used experimentally obtained natural frequencies as inputs. Then, these frequencies must be obtained through modal tests. An impact hammer modal test setup is prepared for the modal tests. This test setup employs an impact hammer combined with an accelerometer, bonded to the part, to obtain the natural frequencies. The part must be held in accordance with the necessary boundary conditions, and then a grid of points must be selected on the part. The modal data will be taken from these grid points, so they have to be dense enough to identify the mode shapes for the necessary natural frequencies that are desired to be obtained. A total of 5 impacts are conducted on each point, and the results are averaged for each

individual point as its final result. The tip of the modal hammer was chosen as a rather compliant material to not damage the composite parts with the impact. In later sections for validation of individual geometries, only the free – free boundary condition cases are validated. To achieve this boundary condition, all parts are held in place by elastic bands. The generic test setup for an impact modal test is presented in Figure 3.24. The hammer used during the tests has 22.5 mV/N sensitivity and the accelerometer has 98.7 mV/g sensitivity, both products of PCB. With the vinyl cover on the impact hammer, up to 300 Hz could be measured, and for higher frequencies the tip was removed which lead to a band of 4000 Hz. The mass of the accelerometer was negligible compared to all considered structures in this thesis, which was checked through finite element analysis, and confirmed through some cases experimentally. Generally, a MAC of above 85% was obtained for all structures, lower ones mainly for pressure vessels and delaminated cases. General plates and cylinders had MAC above 90%.

There are possible error sources in this test scenario. First, the results of the test may vary due to the properties of the impact. To minimize this, an impact was applied as close to normal of the surface as possible while not altering away from the marked points on the surface. Any data showing major deviation compared to the other impacts for the same point was discarded to maintain the quality of the test. Accelerometer on the parts was not permanently bonded to the surface, which may also present errors at very high frequencies.



Figure 3.24 Test configuration used for the impact hammer modal tests.

In the following sections, experiment-based validation of the proposed method is presented, divided into sections for each geometry.

### 3.4.1 Experiment Based Validation for Plate Structures

Previously, the proposed method was validated through numerical simulations for plate geometries. In this section, a few of these cases will be validated experimentally. These cases are presented in Table 3.11.

Table 3.11 Considered cases for the experimental validation of the method for plate geometries

Name	Ply Configuration	Size [mm x mm]	Boundary Condition
P_C2_S2_B2	$[\pm 45]_4$		
P_C7_S2_B2	$[\pm 45/0_4/\pm 45]$	100x100	FFFF
P_C8_S2_B2	$[0_2/\pm 45_2/0_2]$		
P_C9_S2_B2	$[0_2/\pm 45/0_2/\pm 45]$		

A total of 9 points (3x3 grid) are selected on the plate geometry as shown in Figure 3.25 [77]. The location of the accelerometer attached to the plate is also shown in the same figure. Previously, ply orientations for these cases were predicted in section

3.3.1. Hence, for comparison, the method was applied to these cases employing the experimentally obtained first three natural frequencies, and results will be presented. Experimentally obtained natural frequencies for the considered configurations is given in Table 3.12. Using these natural frequencies, and applying the proposed method in this chapter, the average ply orientations for 5 optimization runs in Table 3.13 – Table 3.16 are obtained. An example FRF for the experiments is presented in Appendix C.



Figure 3.25 Composite plate subjected to impact hammer modal test

Table 3.12 Experimentally obtained natural frequencies for the considered plate geometries

Name	1 <sup>st</sup> Natural Frequency [Hz]	2 <sup>nd</sup> Natural Frequency [Hz]	3 <sup>rd</sup> Natural Frequency [Hz]
P_C2_S2_B2	786	1228	1611
P_C7_S2_B2	863	1006	1453
P_C8_S2_B2	556	638	1283
P_C9_S2_B2	776	928	1652

Table 3.13 Results of the optimization runs for ply orientation identification for P\_C2\_S2\_B2 case employing experimentally obtained natural frequencies

Optimization Run	Section 1	Section 2	Section 3	Section 4
5 Run Average	[±43.1]	[±48.6]	[±41.4]	[±44.4]
Target Layup	[±45]	[±45]	[±45]	[±45]

Table 3.14 Results of the optimization runs for ply orientation identification for P\_C7\_S2\_B2 case employing experimentally obtained natural frequencies

Optimization Run	Section 1	Section 2	Section 3	Section 4
5 Run Average	[±45.1]	[±0.6]	[±3.2]	[±45.0]
Target Layup	[±45]	[0] <sub>2</sub>	[0] <sub>2</sub>	[±45]

Table 3.15 Results of the optimization runs for ply orientation identification for P\_C8\_S2\_B2 case employing experimentally obtained natural frequencies

Optimization Run	Section 1	Section 2	Section 3	Section 4
5 Run Average	[±1.0]	[±41.2]	[±47.8]	[±0.3]
Target Layup	[0] <sub>2</sub>	[±45]	[±45]	[0] <sub>2</sub>

Table 3.16 Results of the optimization runs for ply orientation identification for P\_C9\_S2\_B2 case employing experimentally obtained natural frequencies

Optimization Run	Section 1	Section 2	Section 3	Section 4
5 Run Average	[±0.2]	[±45.1]	[±0.7]	[±42.9]
Target Layup	[0] <sub>2</sub>	[±45]	[0] <sub>2</sub>	[±45]

### 3.4.2 Experiment Based Validation for Cylindrical Structures

Like the experimental validation of plate structures, in this section experiment-based validation of cylindrical structures is presented. Cases considered for experimental validation are presented in Table 3.17.

Table 3.17 Considered cases for the experimental validation of the method for cylindrical geometries

Name	Ply Configuration	Size [mm x mm]	Boundary Condition
C_C10_S3_B2	[±40]	R73x260	FFFF
C_C11_S4_B2	[90] <sub>2</sub>		

A total of 60 points (12 in circumference, 5 along axial direction) are selected as the impact points for the modal tests. Modal test setup for C\_C10\_S3\_B2 is presented in Figure 3.26. Experimental validation methodology is the same as in section 3.4.1 for plate cases. Natural frequencies are obtained experimentally and are presented in Table 3.18. Average ply orientations obtained through 5 optimization runs using the experimentally natural frequencies is presented in Table 3.19 for both cases.



Figure 3.26 Composite cylinder subjected to impact hammer modal test



Table 3.18 Experimentally obtained natural frequencies for the considered cylindrical geometries

Name	1 <sup>st</sup> Natural Frequency [Hz]	2 <sup>nd</sup> Natural Frequency [Hz]	3 <sup>rd</sup> Natural Frequency [Hz]
C_C10_S3_B2	24.6	31.0	69.8
C_C11_S4_B2	67.1	68.2	192.3

Table 3.19 Results of the optimization runs for ply orientation identification for cylindrical geometry cases employing experimentally obtained natural frequencies

Optimization Run	C_C10_S3_B2	C_C11_S4_B2
5 Run Average	[±39.7]	[89.7/91.2]
Target Layup	[±40]	[90] <sub>2</sub>

### 3.4.3 Experiment Based Validation for Pressure Vessel Structures

One of the cases shown in numerical validation of pressure vessel structures is validated experimentally in this section. Properties of the considered case, which is PV\_C14\_S4\_B2, is shown in Table 3.20. The manufactured pressure vessel is also present in Figure 3.27.

Table 3.20 Considered case for the experimental validation of the method for pressure vessel geometries

Name	Ply Configuration	Size	Boundary Condition
PV_C14_S4_B2	<i>XXO</i>	Figure 3.20	FFFF

Similar to the previous experimental validation cases, the experimentally obtained natural frequencies are presented in Table 3.21, and the average ply orientations for 5 optimization runs calculated through the experimentally obtained natural frequencies is shown in Table 3.22.



Figure 3.27 Composite pressure vessel manufactured that is to be subjected to impact hammer modal test

Table 3.21 Experimentally obtained natural frequencies for the considered pressure vessel geometries

Name	1 <sup>st</sup> Natural Frequency [Hz]	2 <sup>nd</sup> Natural Frequency [Hz]	3 <sup>rd</sup> Natural Frequency [Hz]
PV_C14_S4_B2	1366	1856	2235

Table 3.22 Results of the optimization runs for ply orientation identification for pressure vessel geometry cases employing experimentally obtained natural frequencies

Optimization Run	Section 1	Section 2	Section 3
5 Run Average	[±40.2]	[±45.1]	[90.7]
Target Layup	[±40]	[±40]	[90]

### **3.5 Evaluation of the Performance of Proposed Method for Ply Layup Identification**

In this chapter, a novel method is proposed to assess the ply angle variations in a laminate for various geometries. The proposed method divides into 3 main steps, which are obtaining the range for  $D^*$  parameters, optimization of these parameters, and finally, obtaining the ply orientations through optimized  $D^*$  parameters.

The method works exceptionally well for all geometries considered, which are employed in different sizes, ply configurations, boundary conditions, and more. All ply angles were determined within  $5^\circ$  error, even lower for most cases. This was deemed very good accuracy as in the industry for complex shapes, below  $5^\circ$  difference cannot be reliably measured. In fact, with a stricter convergence criterion, errors below  $5^\circ$  can also be obtained with this method, which would only cost higher computation time.

The main weakness of this method is during the optimization of  $D^*$  parameters. If the  $D^*$  parameters are optimized well, then with the employment of trained AI with consecutively smaller search ranges works very robust and accurate in prediction of the ply orientations. However, if these parameters aren't optimized well, then this initial error may be enlarged during the optimization of ply orientations. Unfortunately, the method is based on an estimated area of all possible configurations. While if an analytical formulation is available this is easy and relatively fast, for complex geometries finite element analysis is practically the only tool available, slowing the process down significantly. Also, obviously, a smaller amount of data points will be available with the finite element analysis results, leading to a worse estimation of all possible configurations. Therefore, the method is open to improvement in estimation of the optimized  $D^*$  parameters.

Another weakness of the method is the requirement of some initial knowledge of number of plies. The entire method is based on a set number of plies that are already known at the start, so a missing ply or an extra ply cannot be determined by this

method. This mainly presents problems for thick laminates, where it is not readily easy to identify if a ply is missing or extra in the laminate. Although, this error case was not considered in the scope of the ply orientation errors.

## CHAPTER 4

### IDENTIFICATION OF AVERAGE THICKNESS AND VOLUME FRACTION

During the filament winding production process, bands of fiber are submerged into a resin bath which then adhere some of the resin on their surface. These resin coated fiber bands are then wound onto the mandrel. However, depending on environmental and manufacturing parameters, the amount of resin employed on the part may alter. On top of this, different types or amounts of shrink bands may be used after the winding is complete to decrease the resin content of the final part. Therefore, the amount of resin might be different on two produced parts of identical geometry, which affects the fiber – matrix volume fraction and therefore the thickness of each individual ply. Although thicknesses can be measured, when the part has a complex geometric shape or when it can only be assessed from a single side, measurements might not be possible or accurate enough to assess the thickness variation.

In this chapter, it is aimed to identify these variations in average thickness of the part. As described above, the main factor in the average thickness of a single ply is the amount of resin it employs. Different amounts of resin lead to a different volume fraction, which has a significant impact on the mechanical properties of the laminate. Therefore, like chapter 3, it was aimed to identify the mechanical property changes to later relate to the volume fraction of the produced part, and in sequence, to the average thickness.

Due to the similarities of the proposed method in this chapter and to that in chapter 3, the same workflow will be used with minor adjustments to account for the volume fraction changes. These changes will be explained in detail in upcoming sections.

Although some general information about volume fraction is presented above, not all volume fractions can be employed on parts. Realistically the volume fraction usually takes values around 40% and 70%, as any lower or higher value might cause

significant damage in matrix solely from the manufacturing process, damaging the part before its production is complete. Very high volume fractions also cannot be achieved due to the fact that fibers cannot be 100% packed together to account for no matrix in between from geometric constraints. Also, for thick composite parts, there may be variation of volume fraction through thickness direction, hence presenting another challenge as the volume fractions then need to be calculated at ply levels rather than laminate level.

Micromechanic modelling of composite structures has already been discussed priorly in literature [78-82] as shown in the next section. Therefore, mechanics of composites may be modelled related to the volume fractions through such micromechanical models. More information about micromechanical models employed in the literature is presented below.

#### **4.1 Micromechanical Models for Composite Structures**

As described above, micromechanical modelling of composite materials is required to include the effects of volume fraction and average thickness into the calculation of natural frequencies. This mainly occurs because the micromechanical properties of the composite significantly alter the macromechanical properties of the composite, which are used to estimate the stiffness and mass characteristics of the structure.

There are many different micromechanical models available in the literature, including rule of mixtures, modified rule of mixtures, Chamis model, Halpin-Tsai model, generalized self-consistent model, Mori-Tanaka model, bridging model, asymptotic homogenization, elasticity-based models, and more less commonly acknowledged models [78-82]. Some of these models are based on analytical calculations, and some are empirical. The main purpose of having such a wide variety of different models is that due to the variables in manufacturing, your produced composite part may obey one of the models better than the others. In this

work, the model of Chamis is used to obtain the micromechanical properties of the composite material. The micromechanical model presents the equations below:

$$E_{11} = E^m + (1 - V_v)V_f(E_1^f - E^m) \quad (4.1)$$

$$E_{22} = \frac{E^m}{1 - \sqrt{(1 - V_v)V_f} \left(1 - \frac{E^m}{E_2^f}\right)} \quad (4.2)$$

$$G_{12} = \frac{G^m}{1 - \sqrt{(1 - V_v)V_f} \left(1 - \frac{G^m}{G_{12}^f}\right)} \quad (4.3)$$

$$G_{23} = \frac{G^m}{1 - \sqrt{(1 - V_v)V_f} \left(1 - \frac{G^m}{G_{23}^f}\right)} \quad (4.4)$$

$$v_{12} = v^m + (1 - V_v)V_f(v_{12}^f - v^m) \quad (4.5)$$

Where  $E^m$  is the elastic modulus of matrix,  $E_1^f$  is the elastic modulus of fiber in the fiber direction,  $E_2^f$  is the elastic modulus of the fiber in transverse direction,  $V_v$  is the void fraction,  $G^m$  is the shear modulus of matrix,  $G_{12}^f$  is the fiber-transverse shear modulus of the fiber,  $G_{23}^f$  is the transverse in-plane shear modulus of the fiber,  $v_{12}^f$  is the fiber-transverse Poisson's ratio of the fiber, and  $v^m$  is the Poisson's ratio of the matrix.

On top of the Chamis model, one can define the density of the composite material as

$$\rho = V_f\rho^f + (1 - V_f)\rho^m \quad (4.6)$$

Where  $\rho^f$  is the density of the fiber and  $\rho^m$  is the density of the matrix material. Like density, the thickness of a single ply can also be estimated by volume fractions, assuming the total fiber amount is the same in material. This leads to the equation

$$\frac{h_{ply}^{ref}}{h_{ply}} = \frac{V_f^{ref}}{V_f} \quad (4.7)$$

Where  $h_{ply}$  is the thickness of a ply,  $h_{ply}^{ref}$  is the thickness of a ply with reference volume fraction, and  $V_f^{ref}$  is a reference volume fraction.

Using equations (4.1 – 4.6), one can update the macromechanical properties given in Table 3.2 for different volume fractions, as shown in Table 4.1.

Table 4.1 Mechanical properties of the composite material at different volume fractions

Property	40% $V_f$	50% $V_f$	60% $V_f$	70% $V_f$
$E_{11}$	96450 MPa	120300 MPa	143800 MPa	168200 MPa
$E_{22}, E_{33}$	3580 MPa	4480 MPa	5800 MPa	7900 MPa
$\nu_{12}, \nu_{13}$	0.31	0.29	0.27	0.25
$\nu_{23}$	0.38	0.38	0.38	0.38
$G_{12}, G_{13}$	2300 MPa	2880 MPa	5200 MPa	5040 MPa
$G_{23}$	1430 MPa	1790 MPa	2300 MPa	3160 MPa
$\rho$	1630 kg m <sup>-3</sup>	1580 kg m <sup>-3</sup>	1520 kg m <sup>-3</sup>	1470 kg m <sup>-3</sup>
$h_{ply}$	$1.5h_{ply}^{ref}$	$1.2h_{ply}^{ref}$	$h_{ply}^{ref}$	$0.86h_{ply}^{ref}$

Therefore, since the mechanical properties at other volume fractions are established, a similar methodology as proposed in chapter 3 can be used to identify the volume fractions, average thicknesses, and even ply orientations at the end. However, the general outline of the method as presented in Figure 3.4 needs to be updated to account for the differences volume fraction causes. This will be explained in detail in the following section.

## 4.2 Proposed Method for Identification of Average Thickness and Volume Fraction

The method proposed to assess the average thickness and volume fractions in a structure is similar to that was shown in chapter 3. The updated method adds more on top of Figure 3.4, as shown in Figure 4.1. The lines shown in red in this figure represent the route taken after the step 3 is done, and the optimized volume fraction is obtained.



In step 1, the  $D^*$  parameters range is updated to account for various volume fractions. In step 2, effect of volume fraction is added which presents the output of  $D^*$  parameters that need to be both used in identification of volume fraction and ply orientations. In step 3, pseudo-orientation of plies are obtained which do not represent the actual ply orientations, mainly due to the larger approximated  $D^*$  parameters space. However, in this step, volume fractions are accurately estimated. Once the volume fractions, and therefore the thickness is estimated correctly, the step 3 presented in Figure 3.4 is utilized as a step 4 in this process to obtain the ply orientations correctly if necessary. In step 4, the entire training and search is based on a single volume fraction obtained in step 3. Step 4 is required as a check mechanism, as both volume fraction and ply orientation errors may exist in the laminate.

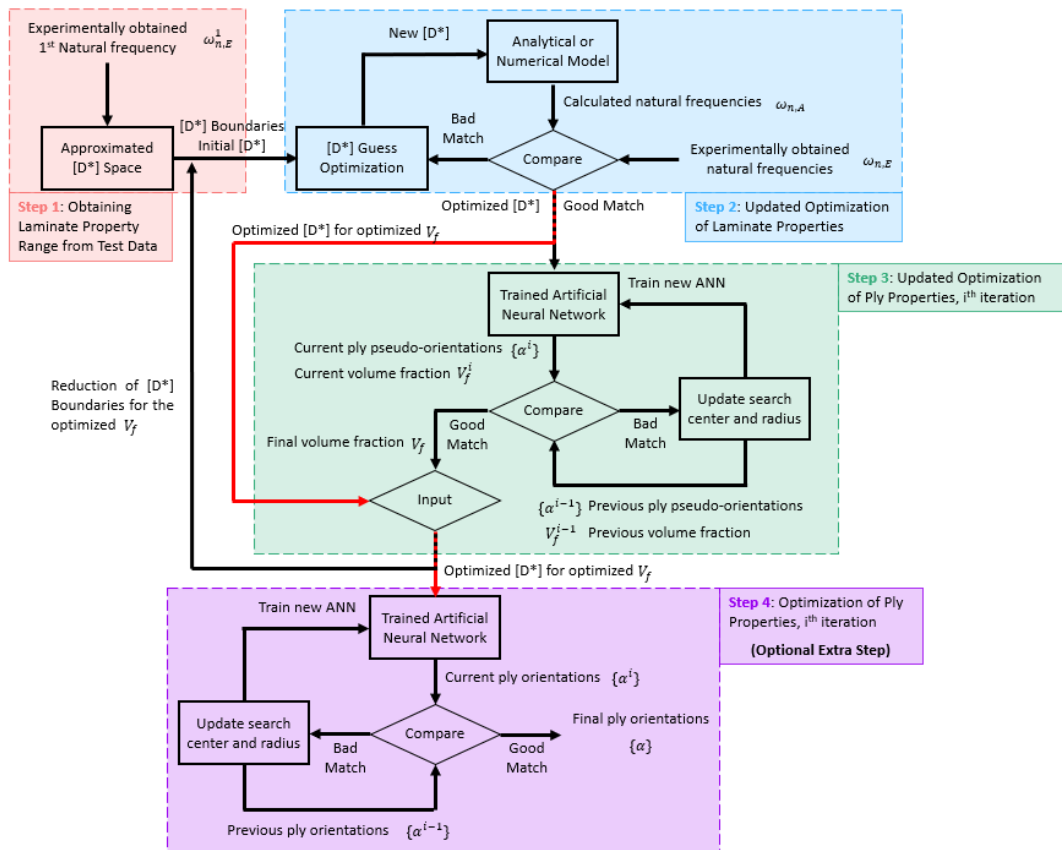


Figure 4.1 Proposed method for obtaining volume fraction and average thickness of a laminate

Due to the consideration of many different volume fractions, the  $D^*$  parameters space is enlarged by the many different volume fractions as shown in Figure 4.2. Hence, in step 1, this newly created larger range is employed to obtain the boundaries of  $D^*$  parameters.

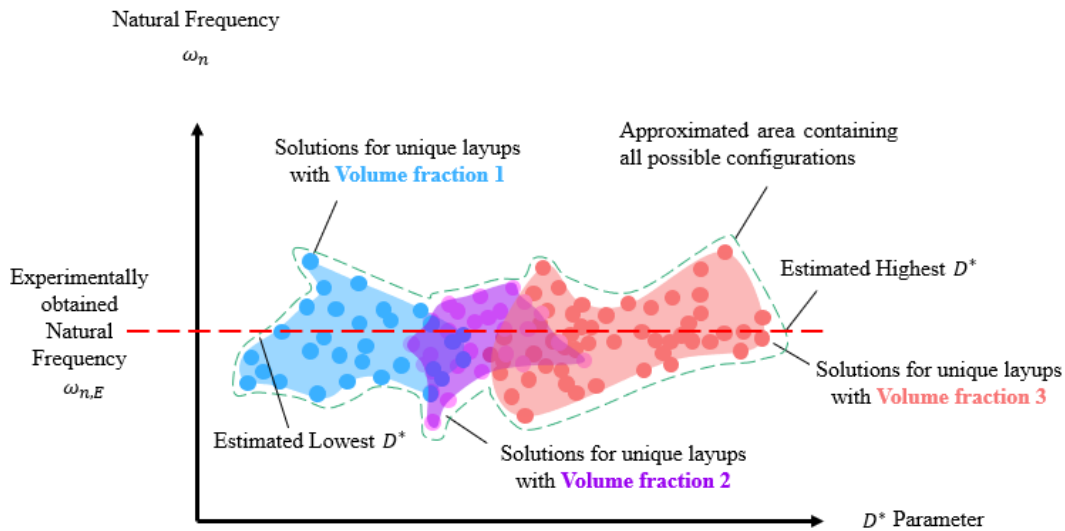


Figure 4.2 Increased range of  $D^*$  parameters due to consideration of different volume fractions

In the following section, insight on optimization of the  $D^*$  parameters given this new increased range is discussed.

#### 4.2.1 Updated Optimization of Laminate Properties

Previously in chapter 3, optimization of  $D^*$  parameters were discussed for a single volume fraction case. To optimize these parameters, a master curve for all  $D^*$  parameters was employed with given lowest and highest boundary ranges as shown in Figure 3.8. Although this method is accurate for a single volume fraction, it starts to be more of a stretch when considering different volume fractions, as the curves shown in this figure are only valid for a single volume fraction. Nevertheless, the same curve shapes will be used for optimization of  $D^*$  parameters. Due to this, the ply angles obtained through these parameters will not be the correct ply angles in the

laminates in a general sense. These ply angles are called as “pseudo-orientations”. However, these pseudo-orientations are not the main concern as we are required to obtain the volume fractions.

Once the volume fraction is set, the  $D^*$  parameters range needs to be updated again for this volume fraction, so that within this new range the curve forms shown in Figure 3.8 will be valid for ply orientations. Therefore, a potentially new set of  $D^*$  parameters is obtained which is to be used in optimization of ply orientations later to get rid of the pseudo-orientations that do not represent the laminate at hand. Once this new set of  $D^*$  parameters is obtained, the red lines shown in Figure 4.1 must be followed to the step 4, where the correct orientations will be obtained.

However, before obtaining these ply orientations, the volume fraction must be determined. In the following section, it is explained in detail how the volume fraction is optimized.

#### **4.2.2 Updated Optimization of Ply Properties**

As mentioned earlier, the optimization scheme similar to chapter 3 will be used that was for identification of ply orientations. However, this time as an additional parameter the volume fractions are added as an unknown to be optimized. Therefore, the pseudo-orientations and the volume fractions are optimized through the ANN at the same time. Although previously reduction of ANN search range was stopped when the convergence of ply orientations was achieved, this time the convergence criteria is changed into the convergence of volume fractions. When the change in volume fraction falls below 1% the process is stopped, and the final volume fraction is obtained.

Although the pseudo-orientations are obtained, this information is discarded as it is acknowledged to not represent the laminate at hand. The newly obtained volume fraction information is then used to reduce the  $D^*$  parameters range, and then the process is practically continued as described in chapter 3. The new  $D^*$  parameters

range is calculated at the determined volume fraction, which is used to estimate the new  $D^*$  parameters boundaries. Within these boundaries, a newly optimized  $D^*$  parameters are found. These parameters are not used in the step 3, but directly fed into the optional step 4 to obtain the correct ply orientations. As much optional as this lastly stated process is, it is a good practice to go through it to identify any other error present in laminate.

### **4.3 Numerical Simulation Based Validation for Identification of Average Thickness and Volume Fraction**

The method proposed prior must be validated. The easiest way to validate the model by various cases is to employ a finite element simulation. In this section, finite element models of various geometries, volume fractions, and ply orientations will be generated and will be treated as unknown laminates. The proposed method will then be applied to these models to estimate their volume fractions and thicknesses.

The construction of these finite element models has been exhaustively described in section 3.3, and the same models will be employed here only by altering the material properties. Below is presented the validation of the proposed method using numerical simulations for different geometries considered.

#### **4.3.1 Numerical Simulation Based Validation for Plate Structures**

In this section, validation of the proposed method for plate type composite structures is shown. Many variables are considered in this scenario, including number of plies, geometric dimensions, ply orientations, boundary condition, and of course, volume fraction, leading to a different thickness. Considered configurations are shown in Table 4.2. The configurations in this table are picked to be in line with the previously considered cases in chapter 3. Similar to chapter 3, only one of the cases will be shown in detail and the results of the other cases will be presented afterwards.

Table 4.2 Considered configurations for numerical simulation based validation of composite plate type structures

Name	Ply Configuration	Size [mm x mm]	Boundary Condition	Volume Fraction
P_C1_V40	$[0]_8$	225x225	SSSS	40%
P_C2_V60	$[\pm 45]_3$	100x100	SSSS	60%
P_C3_V40	$[\pm 15/\pm 70/\pm 20]$	225x225	SSSS	40%
P_C4_V70	$[0_2/\pm 45/90_2]$	225x225	SSSS	70%
P_C5_V55	$[\pm 20]_3$	225x225	SSSS	55%
P_C6_V50	$[\pm 25/\pm 27/\pm 28]$	225x225	SSSS	50%
P_C2_V70	$[\pm 45]_3$	225x225	FFFF	70%

In Table 4.2, a similar naming convention to Table 3.1 is presented. The prefix “P” means that these structures are plates. “C” denotes the ply configuration, which has different numbers for different configurations. “V” denotes the volume fraction, followed by a number that represents the percentage of volume fraction. In this table, P\_C1\_V40 is considered baseline which also has a different number of plies than the rest of the configurations. P\_C2\_V60 presents a both different ply configuration and size. P\_C3\_V40 was chosen to study the effect of various ply angles existing in laminate. P\_C4\_V70 was chosen to study a rather quasi-isotropic laminate. P\_C5\_V55 was chosen to study a laminate that has a volume fraction that does not correspond to the material properties that are directly given in Table 4.1. P\_C6\_V50 was picked to study the effects of ply angles that are close to each other. P\_C2\_V50 was chosen to see the effect of a different boundary condition.

Results of P\_C1\_V40 will be presented in detail. From the finite element simulation, the first three natural frequencies are obtained as 286.9 Hz, 382.9 Hz, and 599.5 Hz with the same mode shapes as shown in Figure 3.10. Therefore, the  $D^*$  parameters range can be obtained from the first natural frequency as shown in Figure 4.3, Figure 4.4, and Figure 4.5. The optimization scheme for  $D^*$  parameters with respect to the equivalent angle is shown in Figure 4.6.

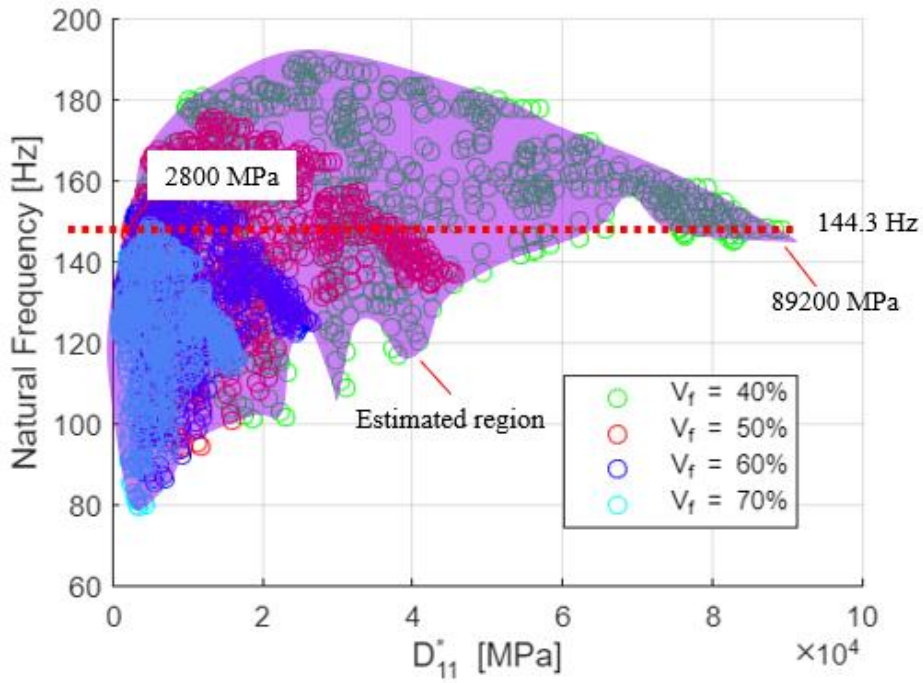


Figure 4.3 Estimated area for  $D_{11}^*$  and the boundary values for the considered first natural frequency

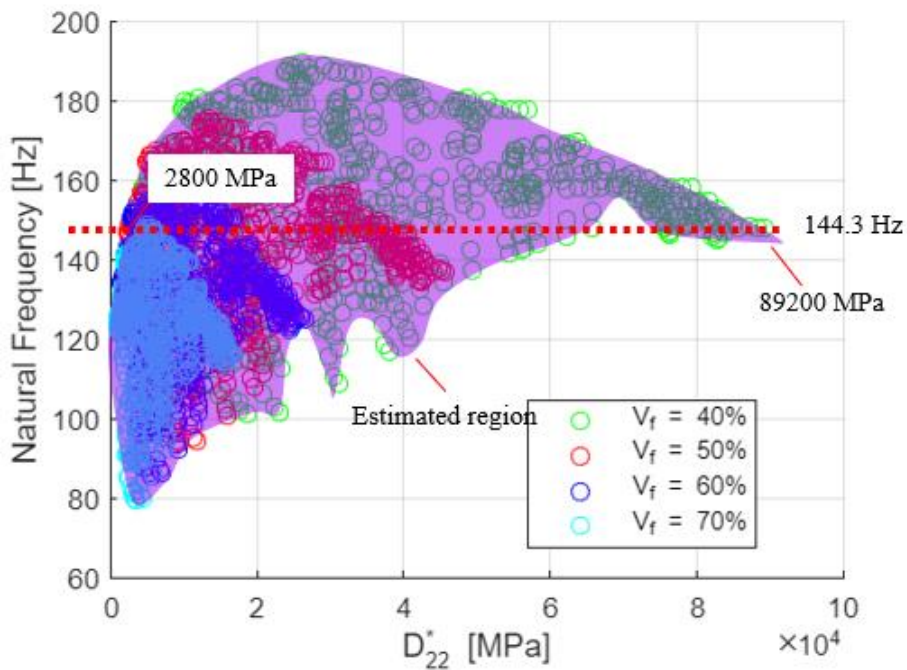


Figure 4.4 Estimated area for  $D_{22}^*$  and the boundary values for the considered first natural frequency

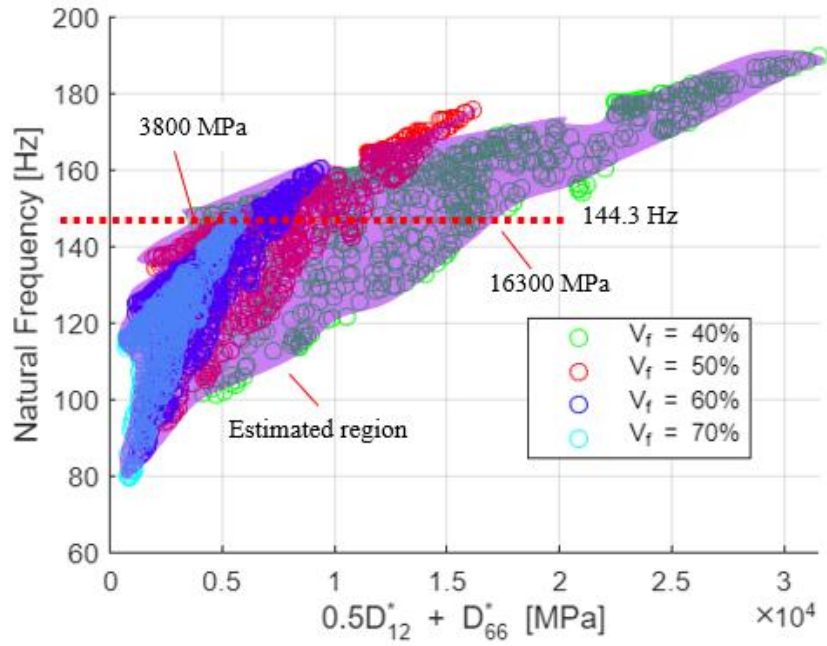


Figure 4.5 Estimated area for  $0.5D_{12}^* + D_{66}^*$  and the boundary values for the considered first natural frequency

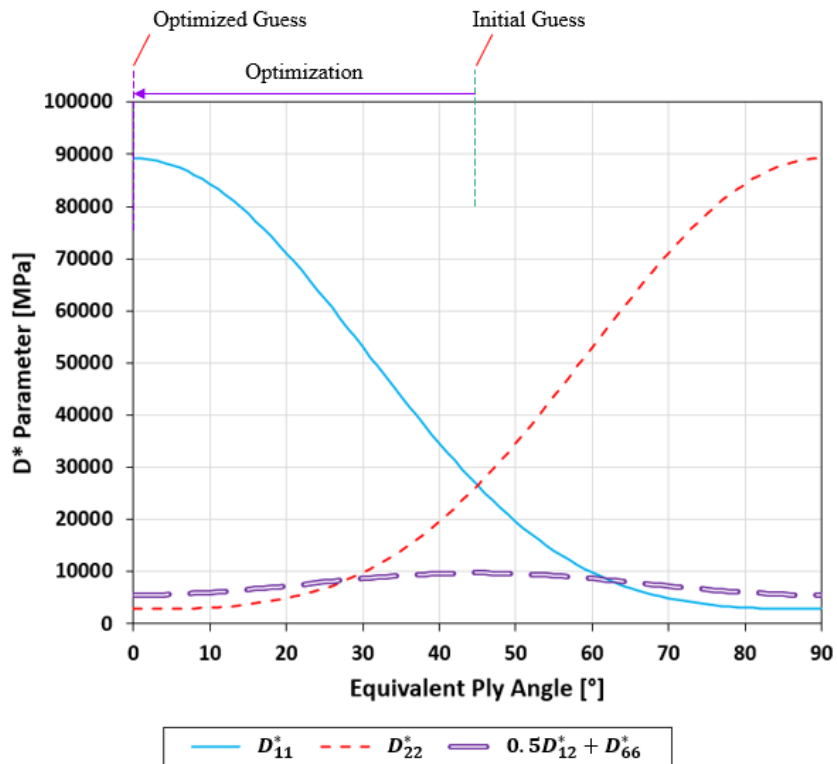


Figure 4.6 Optimization of  $D^*$  parameters given maximum and minimum values

Once the optimized  $D^*$  parameters are obtained, ANN can be used to generate the pseudo-orientations and volume fractions. The iterations of ANN for prediction of these variables are shown in Table 4.3. Several optimization runs for results including volume fractions, laminate thickness, and final pseudo-orientations obtained for the considered case is presented in Table 4.4. Correct ply orientations are obtained by using the step 4 in Figure 4.1 and are presented for P\_C1\_V40 in Table 4.5. As this process was already presented in chapter 3, it will not be repeated for the rest of the cases considered under this section. The final pseudo-orientations, volume fractions, and laminate thicknesses of other cases are presented in Appendix D.

Table 4.3 Pseudo-orientations and volume fractions obtained through the optimization process with consequently reduced search range ANN for P\_C1\_V40

Step Number	Section 1	Section 2	Section 3	Section 4	Volume Fraction
0	[±45]	[±45]	[±45]	[±45]	60%
1	[±16.4]	[±87.2]	[±75.1]	[±36.4]	52%
2	[±4.9]	[±9.1]	[±2.5]	[±23.8]	40%
3	[±4.3]	[±9.0]	[±5.1]	[±1.0]	39%

Table 4.4 Pseudo-orientations, volume fraction, and laminate thickness results of the optimization runs for P\_C1\_V40

Optimization Run	Pseudo-orientations	Volume Fraction	Laminate Thickness [mm]
1	[±4.3/±9.0/±5.1/±1.0]	39%	2.00
2	[±5.5/±2.8/±8.5/±7.5]	38%	2.05
3	[±0.5/±4.1/±4.4/±15.1]	36%	2.17
4	[±9.4/±5.2/±5.4/±5.2]	41%	1.90
5	[±2.7/±6.1/±0.0/±19.0]	45%	1.73
Average	[±4.5/±5.4/±4.7/±9.6]	40%	1.97
Target Layup	$[0]_8$	40%	1.95



Table 4.5 Pseudo-orientations and final ply orientations obtained for each optimization run for P\_C1\_V40

Optimization Run	Pseudo-orientations	Ply Orientations
1	[±4.3/±9.0/±5.1/±1.0]	[±0.9/±0.7/±0.7/±0.5]
2	[±5.5/±2.8/±8.5/±7.5]	[±0.7/±1.9/±1.3/±1.2]
3	[±0.5/±4.1/±4.4/±15.1]	[±2.5/±0.3/±0.7/±0.9]
4	[±9.4/±5.2/±5.4/±5.2]	[±1.2/±0.9/±2.3/±0.9]
5	[±2.7/±6.1/±0.0/±19.0]	[±0.9/±3.9/±0.1/±3.7]
Average	[±4.5/±5.4/±4.7/±9.6]	[±1.2/±1.5/±0.1/±3.7]
Target Layup	[0] <sub>8</sub>	

#### 4.3.2 Numerical Simulation Based Validation for Cylindrical Structures

Just like for the plate type structures, the numerical based validation of the proposed method for cylindrical structures is presented in this section. Due to the fact that many of the parameters were already investigated in section 4.3.1 and in chapter 3, a smaller set of cases is considered under this section. These cases are shown in Table 4.6.

Table 4.6 Considered configurations for numerical simulation based validation of composite cylindrical type structures

Name	Ply Configuration	Size [mm x mm]	Boundary Condition	Volume Fraction
C_C10_V40	[±40]	R73x260	SSSS	40%
C_C11_V70	[90] <sub>2</sub>		FFFF	70%

The naming convention present in Table 4.6 is similar to those of the previous sections. The preposition “C” denotes that these are cylinders. The second “C” in the name represents the configuration, which matches with those that are in chapter 3. The number that follows “V” denotes the volume fraction in percentage. Like the

validation of plate structures, only C\_C10\_V40 case will be presented in detail under this section. Results of the other case will be presented afterwards. The finite element model for this geometry has already been discussed in chapter 3.

From the finite element simulation, one can obtain the first few natural frequencies of C\_C10\_V40 as 440.2 Hz, 471.6 Hz, and 499.4 Hz. Then, the first of these frequencies can be used to estimate the  $D^*$  parameters range as shown in Figure 4.7, Figure 4.8, and Figure 4.9. Then, the optimization of these  $D^*$  parameters can be done as discussed priorly in this chapter, with respect to the equivalent ply angle, as shown in Figure 4.10.

Once the optimized  $D^*$  parameters are obtained, ANN can be used to generate the pseudo-orientations and volume fractions like in section 4.3.1. The iterations of ANN for prediction of these variables are shown in Table 4.7. Volume fractions, laminate thickness, and final pseudo-orientations obtained for each considered case is presented in Table 4.8 and Table 4.9.

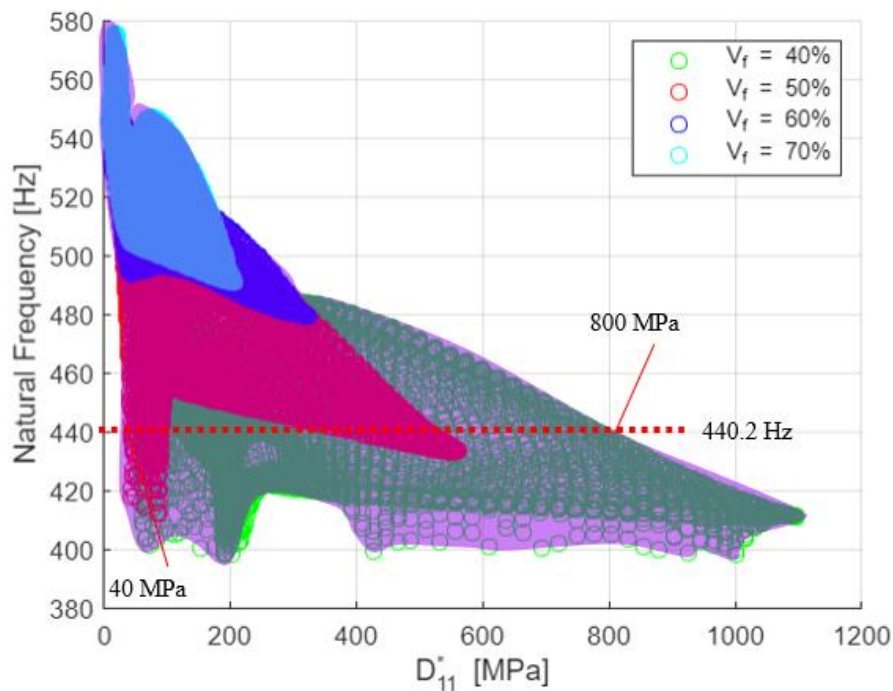


Figure 4.7 Estimated area for  $D_{11}^*$  and the boundary values for the considered first natural frequency

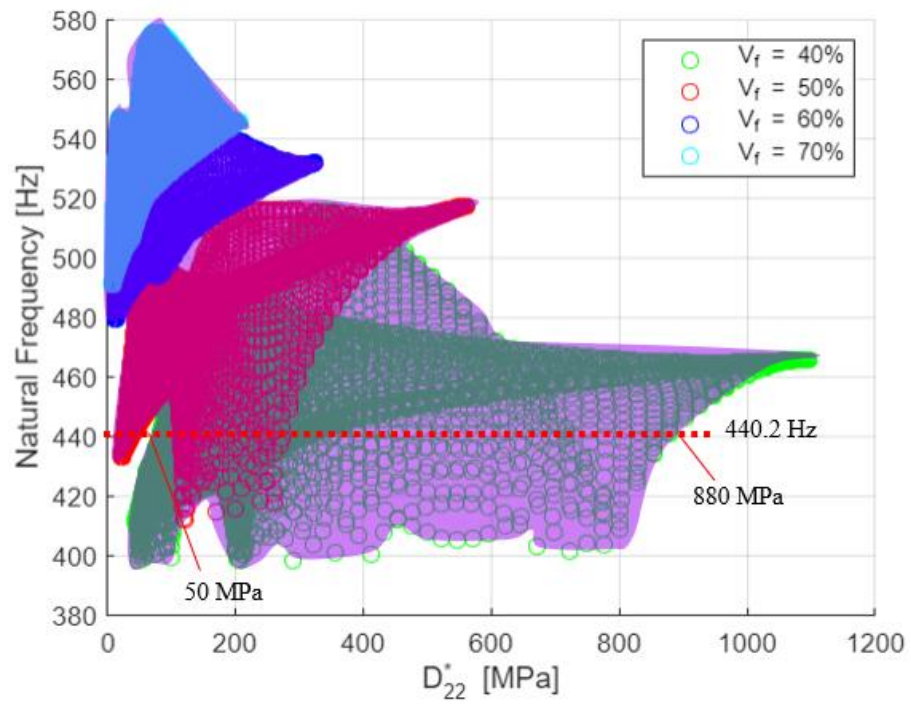


Figure 4.8 Estimated area for  $D_{22}^*$  and the boundary values for the considered first natural frequency

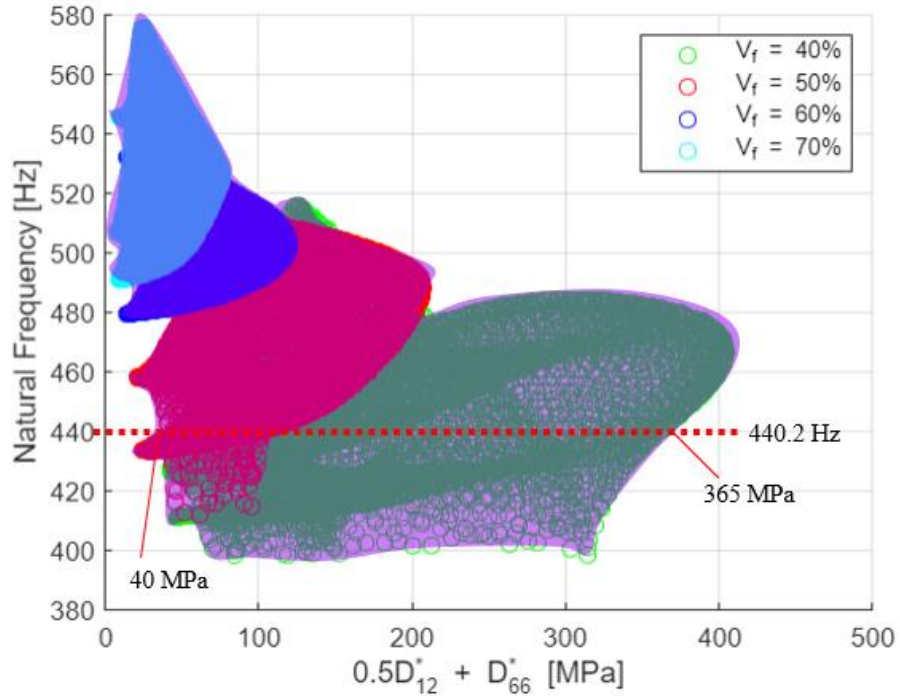


Figure 4.9 Estimated area for  $0.5D_{12}^* + D_{66}^*$  and the boundary values for the considered first natural frequency

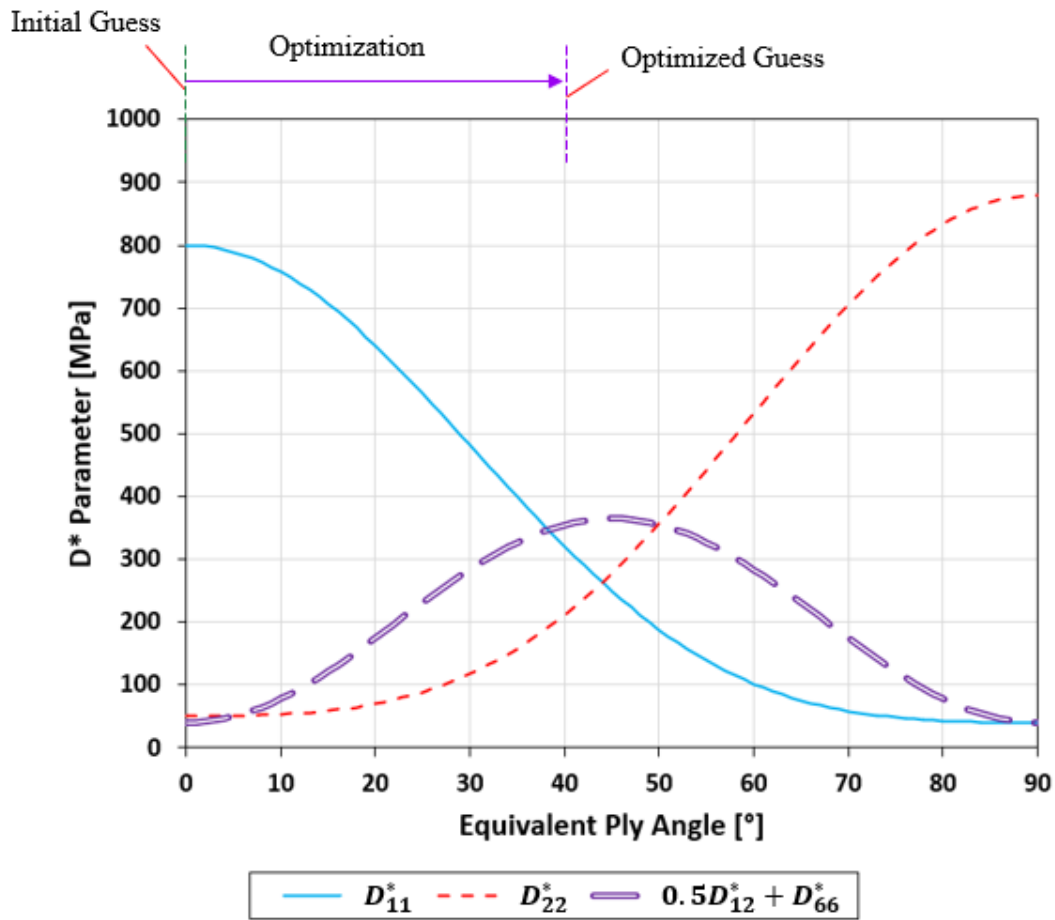


Figure 4.10 Optimization of  $D^*$  parameters given maximum and minimum values

Table 4.7 Pseudo-orientations and volume fractions obtained through the optimization process with consequently reduced search range ANN for C\_C10\_V40

Step Number	Ply Angle [°]	Volume Fraction
0	$[0]_2$	60%
1	$[\pm 55.2]$	62%
2	$[\pm 17.2]$	51%
3	$[\pm 12.9]$	48%
4	$[\pm 21.0]$	43%
5	$[\pm 41.1]$	41%
6	$[\pm 35.5]$	40%

Table 4.8 Pseudo-orientations and final ply orientations obtained for each optimization run for C\_C10\_V40

Optimization Run	Pseudo-orientations	Volume Fraction	Laminate Thickness [mm]
1	[±35.5]	40%	0.45
2	[±32.5]	42%	0.43
3	[±29.2]	41%	0.44
4	[±47.8]	37%	0.49
5	[±37.6]	41%	0.44
Average	[±36.5]	40%	0.45
Target Layup	[±40]	40%	0.45

Table 4.9 Pseudo-orientations and final ply orientations obtained for each optimization run for C\_C11\_V70

Optimization Run	Pseudo-orientations	Volume Fraction	Laminate Thickness [mm]
1	[±89.3]	68%	0.26
2	[±92.7]	73%	0.25
3	[±93.6]	71%	0.25
4	[±96.8]	65%	0.28
5	[±88.7]	69%	0.26
Average	[±92.2]	69%	0.26
Target Layup	[90] <sub>2</sub>	70%	0.26

### 4.3.3 Numerical Simulation Based Validation for Pressure Vessel Structures

Similar to the previous considered geometries, validation of the method for pressure vessel structures is presented in this section. Two pressure vessels are considered for validation, whose geometrical dimensions are given in Figure 3.20. Details about

these vessels are given in Table 4.10. For the numerical simulation of these cases, the same model presented in chapter 3 for pressure vessels is used with altered material properties.

Table 4.10 Considered configurations for pressure vessel geometry

Name	Ply Configuration	Size	Boundary Condition	Volume Fraction
PV_C12_V70	XX	Figure 3.20	FFFF	70%
PV_C13_V40	XXO			40%

The results for PV\_C12\_V70 are shown explicitly below. For the other configuration, only the final results will be presented in a similar fashion to the previous sections for validation. The first three natural frequencies of PV\_C12\_V70 are 1035 Hz, 1426 Hz, and 1844 Hz with the same mode shapes as shown in Figure 3.21. Then, the first natural frequency can be used to obtain the  $D^*$  parameters range, whose natural frequencies were obtained through finite element analysis. This process is shown in Figure 4.11, Figure 4.12, and Figure 4.13. Then, the found range for  $D^*$  parameters can be optimized as shown in Figure 4.14.

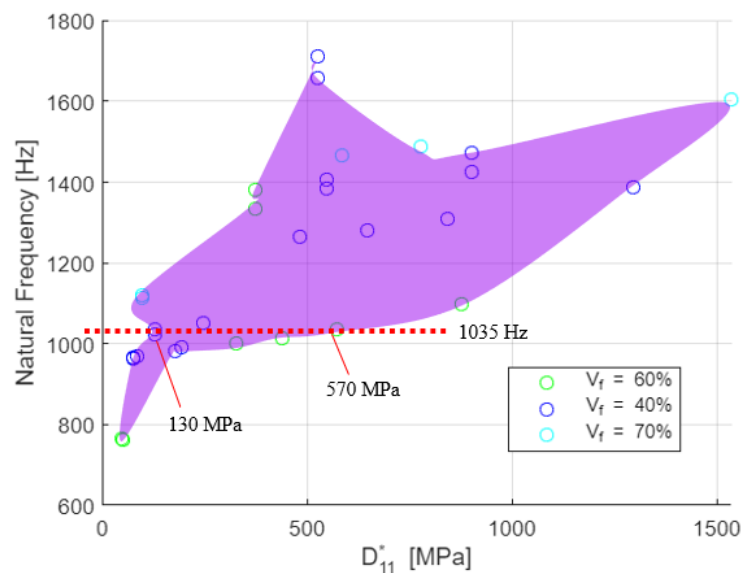


Figure 4.11 Estimated area for  $D_{11}^*$  and the boundary values for the considered first natural frequency

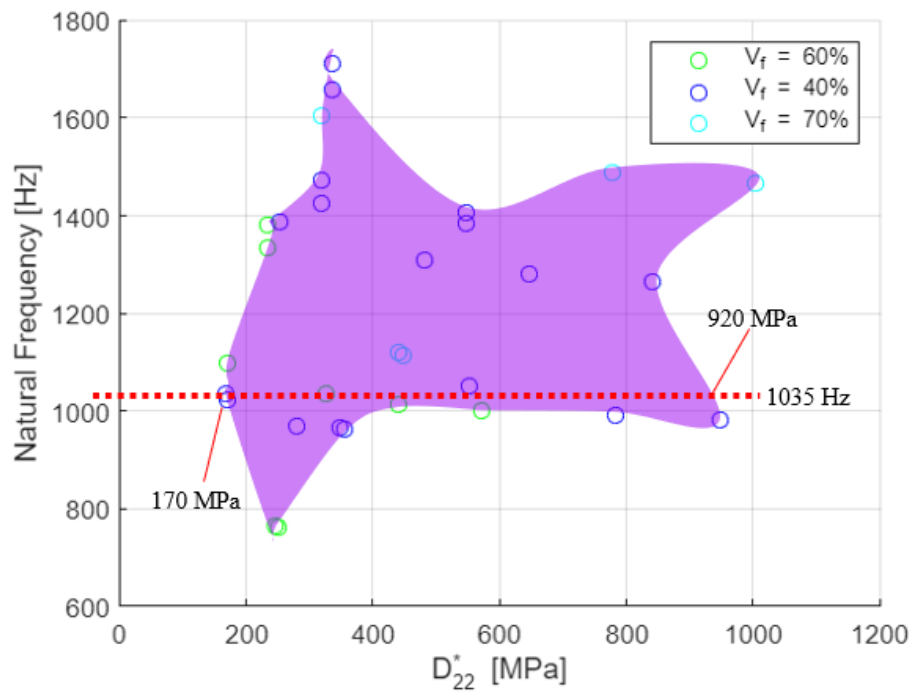


Figure 4.12 Estimated area for  $D_{22}^*$  and the boundary values for the considered first natural frequency

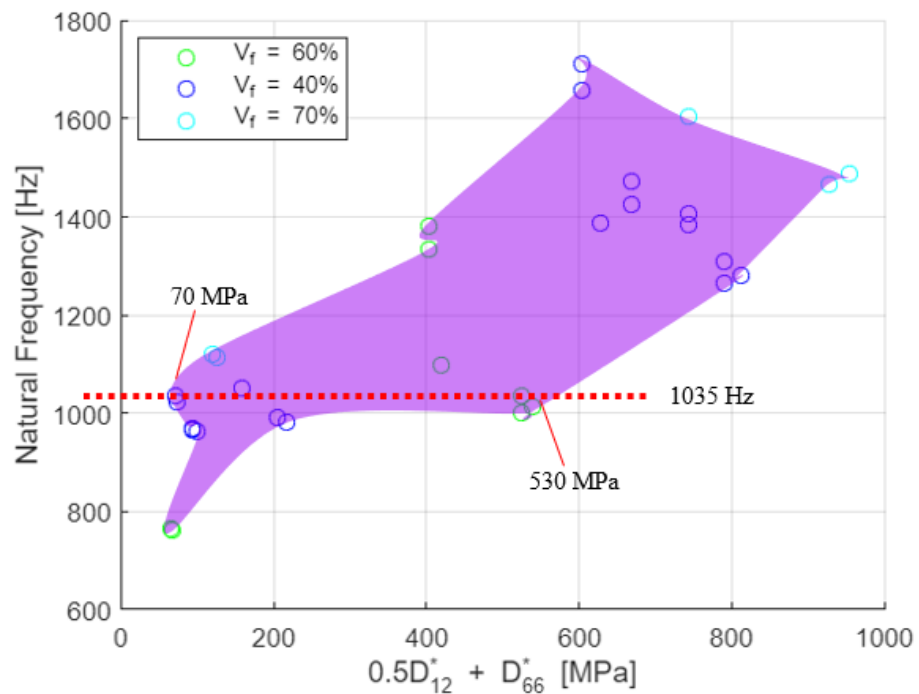


Figure 4.13 Estimated area for  $0.5D_{12}^* + D_{66}^*$  and the boundary values for the considered first natural frequency

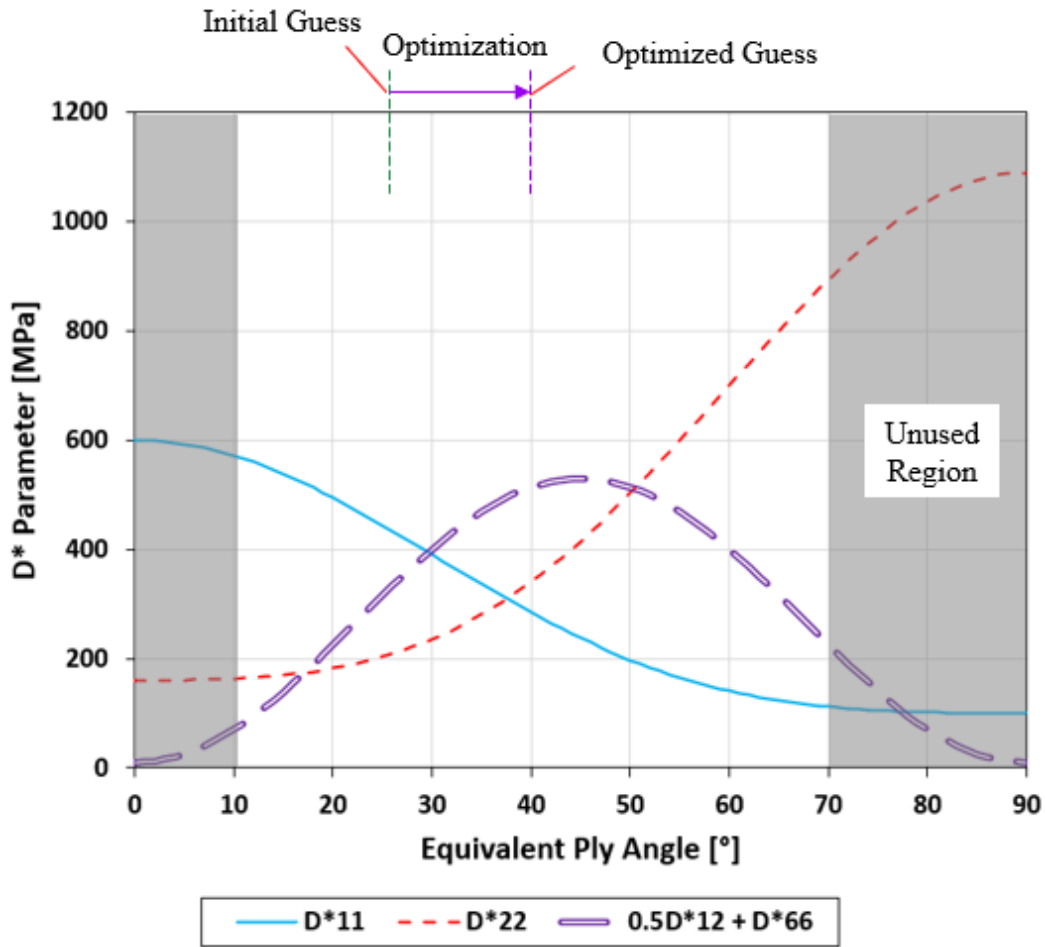


Figure 4.14 Optimization of  $D^*$  parameters given maximum and minimum values

Notice that in Figure 4.11, Figure 4.12, and Figure 4.13, there are no longer separable regions depending on if the layup contains hoop windings. This is mainly because results of the other volume fractions start to interfere with each other. Hence, similar to plate and cylindrical structures, only one region is considered. Also, notice that in Figure 4.14, a wider region is used compared to the one in Figure 3.23. This was to account for the variety of volume fraction. If the process may continue with the step 4 presented in Figure 4.1, then the region presented in Figure 3.23 should be used to account for the possible winding angle range.

When the optimized  $D^*$  parameters are obtained, ANN can be used to generate the pseudo-orientations and volume fractions like the previous sections for validation.



The iterations of ANN for prediction of these variables are shown in Table 4.11. Volume fractions, laminate thickness, and final pseudo-orientations obtained for each considered case is presented in Table 4.12 and Table 4.13.

Table 4.11 Pseudo-orientations and volume fractions obtained through the optimization process with consequently reduced search range ANN for PV\_C12\_V70

Step Number	Section 1	Section 2	Volume Fraction
0	[±25]	[±25]	60%
1	[±35.9]	[±11.2]	67%
2	[±52.5]	[±24.1]	71%
3	[±48.2]	[±27.1]	72%

Table 4.12 Pseudo-orientations and final ply orientations obtained for each optimization run for PV\_C12\_V70

Optimization Run	Pseudo-orientations	Volume Fraction	Laminate Thickness [mm]
1	[±48.2/±27.1]	72%	0.50
2	[±50.7/±37.8]	70%	0.51
3	[±28.8/±31.9]	71%	0.51
4	[±27.3/±41.7]	69%	0.52
5	[±39.7/±46.0]	71%	0.51
Average	[±38.9/±36.9]	71%	0.51
Target Layup	[±40] <sub>2</sub>	70%	0.51

Table 4.13 Pseudo-orientations and final ply orientations obtained for each optimization run for PV\_C13\_V40

Optimization Run	Pseudo-orientations	Volume Fraction	Laminate Thickness [mm]
1	$[\pm 38.5/\pm 29.0/78.8]$	44%	1.03
2	$[\pm 52.4/\pm 53.6/85.8]$	42%	1.08
3	$[\pm 38.8/\pm 28.0/74.4]$	37%	1.22
4	$[\pm 36.4/\pm 37.1/84.3]$	39%	1.16
5	$[\pm 48.4/\pm 38.1/78.7]$	38%	1.19
Average	$[\pm 42.9/\pm 37.2/80.4]$	40%	1.14
Target Layup	$[\pm 40_2/90]$	40%	1.13

#### 4.4 Experiment Based Validation for Identification of Average Thickness and Volume Fraction

Although the proposed method is validated through numerical methods priorly, for the completeness it is elementary that it must also be validated experimentally. Therefore, in this section, an experimental validation similar to that of the chapter 3 is presented. Natural frequencies from structures are obtained experimentally through impact hammer modal tests as shown in section 3.4. Results of the experimental validation based on each considered geometry is given below.

##### 4.4.1 Experiment Based Validation for Plate Structures

Previously, various cases for plate structures were considered under the validation of the proposed method with numerical methods in section 4.3.1 and section 3.3.1. In this section, a few of these cases will be validated experimentally. Considered cases for the experimental validation are presented in Table 4.14. Although P\_C2\_S2\_B2 case was previously validated through the previous method, in this section it will be considered that the volume fraction of the laminate is unknown.

Specimen P\_C2\_V70 is shown in Figure 4.15 under the free-free boundary impact hammer modal test configuration. Natural frequencies obtained experimentally are shown in Table 4.15.

Table 4.14 Considered cases for the experimental validation of the method for plate geometries

Name	Ply Configuration	Size [mm x mm]	Boundary Condition	Volume Fraction
P_C2_V70	$[\pm 45]_3$	225x225	FFFF	70%
P_C2_S2_B2	$[\pm 45]_4$	100x100		60%

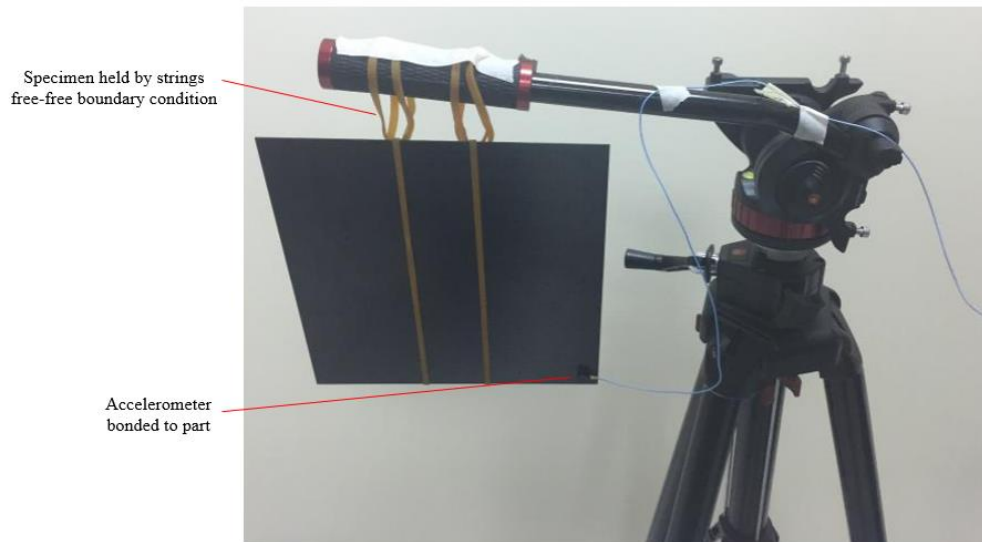


Figure 4.15 Composite plate subjected to impact hammer modal test

Table 4.15 Experimentally obtained natural frequencies for the considered plate geometries

Name	1 <sup>st</sup> Natural Frequency [Hz]	2 <sup>nd</sup> Natural Frequency [Hz]	3 <sup>rd</sup> Natural Frequency [Hz]
P_C2_V70	48.6	76.8	99.1
P_C2_S2_B2	786	1228	1611

Then, by employing the natural frequencies given in Table 4.15, one can use the proposed method to obtain the pseudo-orientations, volume fractions, and the

average thickness. For both cases, these quantities are presented in Table 4.16 and Table 4.17.

Table 4.16 Results of the optimization runs for ply orientation identification for P\_C2\_V70 case employing experimentally obtained natural frequencies

Optimization Run	Pseudo-orientations	Volume Fraction	Laminate Thickness [mm]
5 Run Average	$[\pm 37.2/\pm 65.3/\pm 32.7]$	71%	0.82
Target Layup	$[\pm 45]_3$	70%	0.83

Table 4.17 Results of the optimization runs for ply orientation identification for P\_C2\_S2\_B2 case employing experimentally obtained natural frequencies

Optimization Run	Pseudo-orientations	Volume Fraction	Laminate Thickness [mm]
5 Run Average	$[\pm 65.1/\pm 44.0/\pm 23.9/\pm 52.4]$	60%	2.59
Target Layup	$[\pm 45]_4$	60%	2.6

#### 4.4.2 Experiment Based Validation for Cylindrical Structures

Similar to the validation of plate structures, experimental validation of cylindrical structures of the proposed method is presented in this section. Considered geometries for the validation are presented in Table 4.18.

Table 4.18 Considered cases for the experimental validation of the method for cylindrical geometries

Name	Ply Configuration	Size [mm x mm]	Boundary Condition	Volume Fraction
C_C11_V70	$[90]_2$	R73x200	FFFF	70%
C_C11_S4_B2	$[90]_2$			60%

The specimen that was produced with a higher volume fraction, which is C\_C11\_V70, is shown in Figure 4.16. Experimentally obtained natural frequencies for the considered cases are presented in Table 4.19. Results of the applied proposed method for these cases are then shown in Table 4.20 and Table 4.21.



Figure 4.16 Composite cylinder subjected to impact hammer modal test

Table 4.19 Experimentally obtained natural frequencies for the considered cylindrical geometries

Name	1 <sup>st</sup> Natural Frequency [Hz]	2 <sup>nd</sup> Natural Frequency [Hz]	3 <sup>rd</sup> Natural Frequency [Hz]
C_C11_V70	45.4	46.3	131.0
C_C11_S4_B2	67.1	68.2	192.3

Table 4.20 Results of the optimization runs for ply orientation identification for C\_C11\_V70 case employing experimentally obtained natural frequencies

Optimization Run	Pseudo-orientations	Volume Fraction	Laminate Thickness [mm]
5 Run Average	[±82.1]	71%	0.26
Target Layup	[90] <sub>2</sub>	70%	0.26

Table 4.21 Results of the optimization runs for ply orientation identification for C\_C11\_S4\_B2 case employing experimentally obtained natural frequencies

Optimization Run	Pseudo-orientations	Volume Fraction	Laminate Thickness [mm]
5 Run Average	$[\pm 77.9]$	58%	0.31
Target Layup	$[90]_2$	60%	0.30

#### 4.4.3 Experiment Based Validation for Pressure Vessel Structures

In this section, the validation of the proposed method on composite pressure vessels is presented in a similar fashion to the plate and cylindrical geometries. Considered pressure vessels for this validation is presented in Table 4.22. Experimentally obtained natural frequencies for these geometries is given in Table 4.23. Results of the applied method for these cases are presented in Table 4.24 and Table 4.25.

Table 4.22 Considered cases for the experimental validation of the method for pressure vessel geometries

Name	Ply Configuration	Size [mm x mm]	Boundary Condition	Volume Fraction
PV_C13_V40	<i>XXO</i>	Figure 3.20	FFFF	40%
PV_C14_S4_B2	<i>XXO</i>			60%

Table 4.23 Experimentally obtained natural frequencies for the considered pressure vessel geometries

Name	1 <sup>st</sup> Natural Frequency [Hz]	2 <sup>nd</sup> Natural Frequency [Hz]	3 <sup>rd</sup> Natural Frequency [Hz]
PV_C13_V40	1080	1469	1739
PV_C14_S4_B2	1366	1856	2235

Table 4.24 Results of the optimization runs for ply orientation identification for PV\_C13\_V40 case employing experimentally obtained natural frequencies

Optimization Run	Pseudo-orientations	Volume Fraction	Laminate Thickness [mm]
5 Run Average	$[\pm 42.8/\pm 56.0/88.1]$	40%	1.14
Target Layup	$[\pm 45_2/90]$	40%	1.13

Table 4.25 Results of the optimization runs for ply orientation identification for PV\_C14\_S4\_B2 case employing experimentally obtained natural frequencies

Optimization Run	Pseudo-orientations	Volume Fraction	Laminate Thickness [mm]
5 Run Average	$[\pm 48.9/\pm 27.9/73.6]$	59%	0.76
Target Layup	$[\pm 45_2/90]$	60%	0.75

#### 4.5 Evaluation of the Performance of Proposed Method for Average Thickness and Volume Fraction

In this chapter, the novel method presented in chapter 3 is extended to cover the average volume fraction and thickness. To account for these effects, initial search range and a pseudo ply orientation optimization is employed. The outcome of this method proposes accurate volume fractions, but the ply orientations cannot be assessed. Once the volume fraction is obtained through the proposed method, and optional step may be added to assess the ply orientations as well.

The method works with high accuracy for all considered geometries in both numerical and experimental validation. Validated cases considered several different boundary conditions, sizes, ply orientations, volume fractions, and thicknesses.

Although the method works very well for average quantities, parts may have variable volume fractions in regions. This may lead to waviness over the parts surface, where

the thickness alters. The method does not cover such effects and can only assess the parts on a global scale.

Another weakness of the method is the requirement of a micromechanical model. As discussed, priorly, with different manufacturing techniques or environmental variables employed, different micromechanical models may be more suitable to obtain the micromechanical properties of a composite laminate. Without extensive testing on the part at hand the best micromechanical model may not be chosen, which will lead to more errors in volume fraction. However, as can be seen from the sections for validation, the method has high precision on volume fraction. Therefore, the use of another micromechanical model will most likely present accuracy error and not precision error, which can be either calibrated or used to quickly identify which micromechanical model must be used.



## CHAPTER 5

### IDENTIFICATION OF DELAMINATION

Delaminations are a unique manufacturing error that may easily be encountered when there exists little know-how on the manufacturing techniques used, mainly during the manufacturing of a new laminate or composite structure. As the complexity of geometry, layup, and manufacturing technique increases, the chance to encounter delamination in the structure also increases. These delaminations may either be localized that will not present a major effect on the structure, or they may reach the sizes that may cover almost the entire structure, heavily affecting the mechanical properties such as stiffness. Therefore, the existence of such aggressive delaminations may be tracked by examining the mechanical behavior change of the structure at hand.

As opposed to the other manufacturing errors considered, the change in mechanical behavior of the structure may be smaller, and even undetectable with a simple modal test. As presented in literature survey, delamination in structures can be identified by dynamic & vibration based techniques when the delamination covers at least 10-15% of the area of the structure. Therefore, the change in mechanical behavior must be amplified so that it may be detected. In literature, this amplification has been employed on a beam type structure with an added mass [83]. Due to the reduced stiffness of the region with delamination, the added mass helps amplify modes affected by this region which can be detected. However, this method has a downside that it can only assess the delaminations locally. Therefore, the mass must be applied to several places in the structure to assess it completely.

Therefore, the mentioned mass addition method can be used to detect the delaminations in more complex structures such as plates, cylinders, and pressure vessels, as shown below.

## 5.1 Employed Method for Identification of Delamination

As described before, delaminations in a structure will cause a gap between the layers in the laminate, causing an alteration in stiffness and damping for the structure. Therefore, the effect of delamination on the structure may be tracked by the change in stiffness, whose modal characteristics may be amplified by the addition of a local mass at the delamination area. This amplification effect is shown in Figure 5.1.

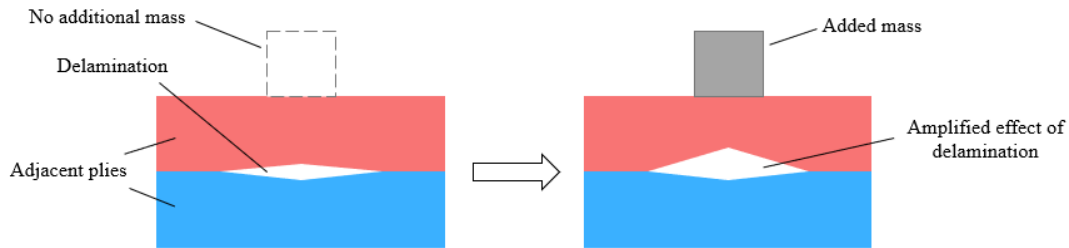


Figure 5.1 Amplification of the effects of delamination by the added mass

Consider a delaminated structure who has a stiffness matrix  $[k]$  and mass matrix  $[m]$ . Then, for the structure one can write

$$([k] - \omega^2[m])\{\phi\} = \{0\} \quad (5.1)$$

Where  $\{\phi\}$  are the mode shape vectors and  $\omega$  is the natural frequency.

From equation (5.1) one can obtain the modal mass and stiffness matrices as

$$[K] = [\phi]^T [k] [\phi] \quad (5.2)$$

$$[M] = [\phi]^T [m] [\phi] \quad (5.3)$$

Then, consider a local mass addition of  $m_0$  to the structure at position  $x_0$ . Assume that the addition of a local mass does not alter the stiffness of the structure, but only contributes to the total mass. Then, the new modal mass and stiffness for the  $i^{\text{th}}$  mode can be defined as

$$\bar{K}_i = \{\bar{\phi}_i\}^T [k] \{\bar{\phi}_i\} \quad (5.4)$$

$$\bar{M}_i = \{\bar{\phi}_i\}^T [m] \{\bar{\phi}_i\} + m_0 \bar{\phi}_i^2(x_0) \quad (5.5)$$

Where  $\bar{K}_i$  and  $\bar{M}_i$  are the new modal stiffness and mass elements for the  $i^{\text{th}}$  mode, and  $\{\bar{\phi}_i\}$  is the new mode shape for the  $i^{\text{th}}$  mode.

Then, the natural frequency of the modified structure can be calculated using equations (5.1), (5.4), and (5.5) as

$$\omega_i = \sqrt{\frac{\{\bar{\phi}_i\}^T [k] \{\bar{\phi}_i\}}{\{\bar{\phi}_i\}^T [m] \{\bar{\phi}_i\} + m_0 \bar{\phi}_i^2(x_0)}} \quad (5.6)$$

From equation (5.6) it is visible that if the mode shapes alter in the structure, a major change in natural frequency will occur. Therefore, it will be easy to detect such a change. However, to affect the modes to such degree a very high amount of mass must be added to the structure which is not practical. Therefore, the case where the mode shapes do not alter significantly needs to be considered as well. Then, the equation (5.6) becomes

$$\omega_i = \sqrt{\frac{\{\phi_i\}^T [k] \{\phi_i\}}{\{\phi_i\}^T [m] \{\phi_i\} + m_0 \phi_i^2(x_0)}} \quad (5.7)$$

However, for the structure that was not modified with an added mass, the natural frequencies could also be calculated using equations (5.1 – 5.3) in a similar fashion. Then, a ratio of natural frequencies for the modified and unmodified structure may be defined as

$$\left(\frac{\omega_{modified}}{\omega_{original}}\right)_i = \sqrt{\frac{\{\phi_i\}^T [m] \{\phi_i\}}{\{\phi_i\}^T [m] \{\phi_i\} + m_0 \phi_i^2(x_0)}} \quad (5.8)$$

Where  $\omega_{modified}$  is the natural frequency of the mass modified structure and  $\omega_{original}$  is the natural frequency of the original structure that only features a delamination.

From equation (5.8) two insights can be obtained. Firstly, if the added mass location corresponds to a part of the mode where the magnitude of the mode shape is low, then the effect of the added mass will also be low. This practically means that several modes must be checked so that problems related to the mode shape may be

eliminated. Secondly, the added mass should not be negligible compared to the structure so that the addition effects can be observed. The amount of added mass may be reduced depending on how large the magnitude of the mode shape is depending on the location on the structure.

Although the above calculations are correct for an added point mass, in reality, the added mass will be bonded to the surface, which may implement an added stiffness. Such an addition of stiffness may be included in equation (5.6) to obtain

$$\omega_i = \sqrt{\frac{\{\bar{\phi}_i\}^T [k] \{\bar{\phi}_i\} + k_0 \bar{\phi}_i^2(x_0)}{\{\bar{\phi}_i\}^T [m] \{\bar{\phi}_i\} + m_0 \bar{\phi}_i^2(x_0)}} \quad (5.9)$$

Where  $k_0$  is the local stiffness introduced by the bonded mass to the surface.

Inclusion of such a stiffness will lead an alternate form of the equation (5.8) as

$$\begin{aligned} & \left( \frac{\omega_{modified}}{\omega_{original}} \right)_i \\ &= \sqrt{\frac{\{\phi_i\}^T [m] \{\phi_i\} \quad \{\bar{\phi}_i\}^T [k] \{\bar{\phi}_i\} + k_0 \bar{\phi}_i^2(x_0)}{\{\phi_i\}^T [m] \{\phi_i\} + m_0 \phi_i^2(x_0) \quad \{\bar{\phi}_i\}^T [k] \{\bar{\phi}_i\}}} \end{aligned} \quad (5.10)$$

Notice that in equation (5.10) both the stiffness and mass are increasing in opposite ways. Therefore, it should be aimed to add the most mass while adding the least stiffness to the structure so that the adversary effect of the added stiffness may be diminished easily.

In the upcoming sections, the application of the added mass method will be validated through numerical simulations, and later, with modal test data.

## 5.2 Simulation Based Validation for Delamination Identification

In this section, the method described under this chapter will be validated through finite element simulations. The construction of the finite element model and its details have been explained priorly in chapter 3 and shall be used as is in this chapter as well. However, a mass and delamination must be added to the structure. The mass

is added as a steel cube, which is bonded to the surface of the composite material. Bonded in this context means that inner and outer plies do not have any relative displacement between each other, they move as one in the finite element analysis. The delamination is created by employing two different composite parts. These two composite parts are bonded to each other throughout the entire structure except for the delamination area. Hence, by alternating the plies on each individual composite structure, delamination may be created at any point in the laminate. This way of adding delamination in a structure is shown in Figure 5.2.

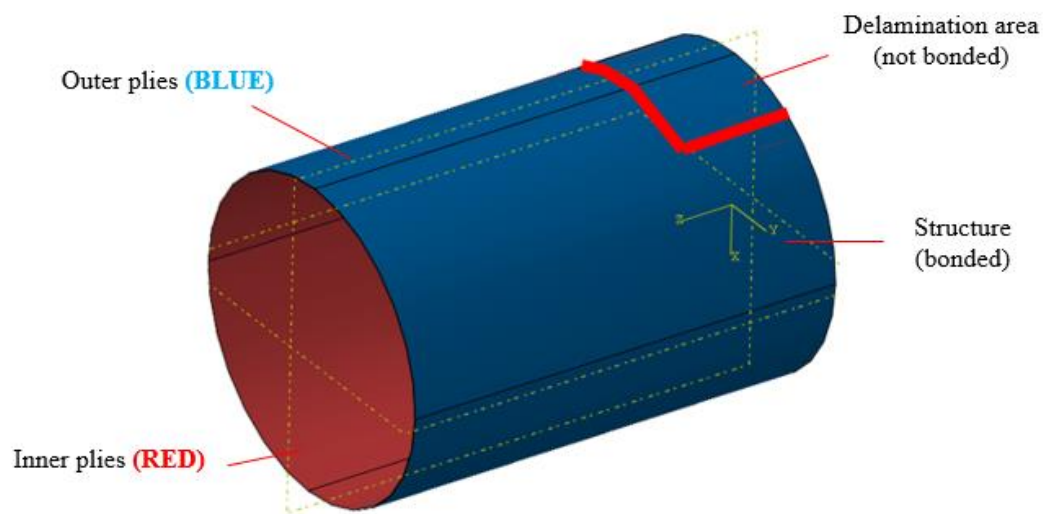


Figure 5.2 Finite element model of added delamination to a composite structure

Therefore, as shown in Figure 5.2, inner and outer plies can move without restriction with each other in the delamination area, and have to move together at the rest of the structure. Due to this modelling technique, nonlinearities such as the friction in the gap, closing and reopening of the gap, sliding, contact, impact cannot be included. Hence, it is expected that the numerical simulations will yield an exaggerated response compared to the real structure. Due to the free movement of inner and outer plies, it may also yield to mode shapes that do not exist in reality.

Under the assumptions and modelling techniques stated above, the effect of the added mass is studied on the previously considered geometries, and is presented below.

### 5.2.1 Numerical Simulation Based Validation of Plate Structures

In this section, the effect of place of delamination, the place of the applied mass, and the delamination size will be investigated on composite plate structures. Considered cases for these effects are given in Table 5.1 and Figure 5.3. The naming convention is similar to validation sections discussed before, “P” prefix denoting plate and “D” denoting the case is for delamination.

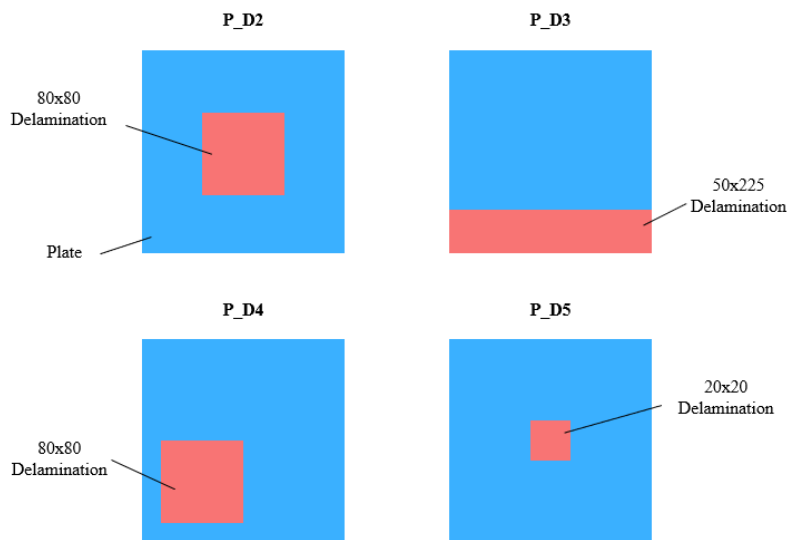


Figure 5.3 Considered cases for the validation of employed method for plate geometries

Table 5.1 Considered cases for the validation of plate geometries

Name	Ply Configuration	Size [mm x mm]	Delamination [mm x mm]
P_D1			-
P_D2			80x80 in middle
P_D3	[0/90] <sub>s</sub>	225x225	50x225 at edge
P_D4			80x80 with one corner of delamination in middle
P_D5			20x20 in middle

Case P\_D1 is a healthy structure with no delamination, hence it is taken as the baseline. P\_D2 has a delamination in the middle of the plate, covering 12.5% of the

structure's entire area. P\_D3 is an edge delamination that covers 22.2% of the structure's area. P\_D4 is the same case as P\_D2 but the delamination location shifts in such a manner that one edge of the delamination is now in the center. Case P\_D5 is the same case as P\_D2 only with a smaller delamination, covering less than 1% of the structure's entire area.

In consideration of the defect, several cases must be checked for validation. First, the base structure and the structure with delamination will be considered. The results of these cases will provide a baseline that we can consider without the application of additional mass. Then, the mass will be applied on both the baseline and the delaminated structure at the same location. The natural frequencies of these two cases will be considered, and the absolute difference in the natural frequencies will be compared to the absolute difference of the structures without the added mass. The employed method expects that this absolute difference will be amplified.

For all the considered cases, the applied additional mass is modelled as a steel cube with a side of 20 mm. The cube is directly bonded to the surface of the composite structure. Modal analysis of the structures is computed for free – free boundary condition for all considered cases.

For P\_D2, the mass is applied directly at the center of the delamination and the laminate. Calculated natural frequencies through finite element analysis and their absolute differences are presented in Table 5.2.

In Table 5.2, it is seen that a maximum of 6.8% absolute difference in natural frequencies are obtained for the case with no additional mass. However, when an additional mass is applied to the delamination region, the absolute difference grew to be as large as 30.1%. Without the mass, for most of the cases, the absolute difference in natural frequencies is below 1%, while for the majority of the cases with added mass, the absolute difference is in the order of 10%.

A similar analysis is conducted for P\_D3, and the results are presented in Table 5.3. In this table, while absolute differences around 7.5% are expected for cases with no

additional mass, the absolute difference jumps to 46% with the additional mass. This increase in absolute difference was expected since edge delamination is a more aggressive case for delaminations. Since the plate has majorly bending modes, the edge delaminations can be exaggerated even further.

Table 5.2 Natural frequencies of P\_D2 case compared to P\_D1.

<u>No Added Mass</u>			<u>Added Mass</u>		
P_D1	P_D2	Abs. Dif.	P_D1	P_D2	Abs. Dif.
[Hz]	[Hz]	[%]	[Hz]	[Hz]	[%]
43.3	45.5	5.1	49.0	46.2	5.7
102.4	102.3	0.1	85.0	77.5	8.8
135.0	137.3	1.7	132.6	129.0	2.7
229.9	227.8	0.9	196.1	157.1	19.9
245.3	246.8	0.6	230.5	161.2	30.1
282.8	263.5	6.8	254.9	180.2	29.3
308.4	309.4	0.3	277.8	248.2	10.7
310.9	311.8	0.3	318.6	259.1	18.7

Table 5.3 Natural frequencies of P\_D3 case compared to P\_D1.

<u>No Added Mass</u>			<u>Added Mass</u>		
P_D1	P_D3	Abs. Dif.	P_D1	P_D3	Abs. Dif.
[Hz]	[Hz]	[%]	[Hz]	[Hz]	[%]
43.3	41.3	4.6	48.1	40.5	15.8
102.4	99.2	3.1	83.7	45.2	46.0
135.0	124.9	7.5	132.5	106.7	19.5

For P\_D4, two different cases are considered since the delamination is not centered. The first one is similar to the previous cases, where the mass is attached to the center of the delamination. The results for this case are presented in Table 5.4. The second case is the mass being attached at a wrong location, directly opposite to the delamination with respect to the center. The results for this case are presented in



Table 5.5. Configuration of the mass attachment for these cases are presented in Figure 5.4.

Table 5.4 Natural frequencies of P\_D4 case compared to P\_D1, with added mass on delamination

<u>No Added Mass</u>			<u>Added Mass</u>		
P_D1	P_D4	Abs. Dif.	P_D1	P_D4	Abs. Dif.
[Hz]	[Hz]	[%]	[Hz]	[Hz]	[%]
43.3	45.3	4.6	46.5	44.6	4.1
102.4	101.3	1.1	95.6	88.9	7.0
135.0	136.9	1.4	136.0	130.9	3.8
229.9	216.3	5.9	199.9	144.7	27.6
245.3	243.3	0.8	241.8	172.3	28.7
282.8	278.0	1.7	254.4	201.0	22.1
308.4	303.9	1.5	295.5	241.0	18.9
310.9	311.4	0.2	302.9	260.6	14.4

Table 5.5 Natural frequencies of P\_D4 case compared to P\_D1, with added mass at the opposite side of the delamination

<u>No Added Mass</u>			<u>Added Mass</u>		
P_D1	P_D4	Abs. Dif.	P_D1	P_D4	Abs. Dif.
[Hz]	[Hz]	[%]	[Hz]	[Hz]	[%]
43.3	45.3	4.6	46.5	47.8	2.8
102.4	101.3	1.1	95.6	93.8	1.9
135.0	136.9	1.4	136.0	136.5	0.4
229.9	216.3	5.9	199.9	195.5	2.2
245.3	243.3	0.8	241.8	228.3	5.6
282.8	278.0	1.7	254.4	254.5	1.4
308.4	303.9	1.5	295.5	293.3	1.3
310.9	311.4	0.2	302.9	303.1	0.4

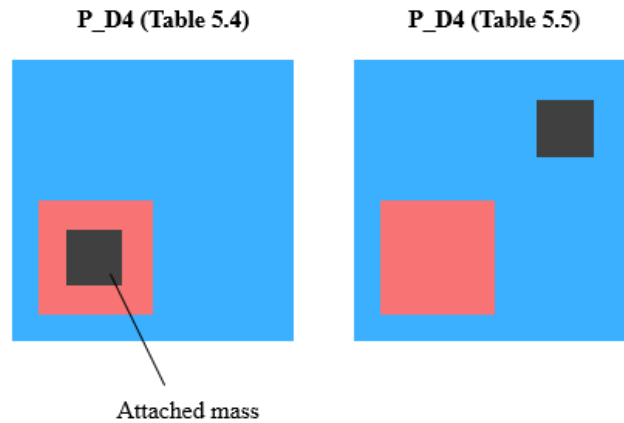


Figure 5.4 Considered cases with different added mass locations for P\_D4

As evident from Table 5.4 and Table 5.5, although the absolute difference in natural frequencies is amplified when the mass is applied to the delamination location, when it is applied elsewhere the order of absolute difference falls down to the case with no delamination applied at all. This further validates the argument that the mass has to be applied within the region of delamination so that the delamination may be detected.

Table 5.6 Natural frequencies of P\_D5 case compared to P\_D1

<u>No Added Mass</u>			<u>Added Mass</u>		
P_D1	P_D5	Abs. Dif.	P_D1	P_D4	Abs. Dif.
[Hz]	[Hz]	[%]	[Hz]	[Hz]	[%]
43.3	43.3	0.1	49.0	49.0	0.0
102.4	102.4	0.1	85.0	85.1	0.1
135.0	135.1	0.1	132.6	132.6	0.0
229.9	229.9	0.0	196.1	196.1	0.0
245.3	245.4	0.0	230.5	230.6	0.0
282.8	282.8	0.0	254.9	254.9	0.0
308.4	308.4	0.0	277.8	277.9	0.0
310.9	310.9	0.0	318.6	318.6	0.0

Finally, the results for P\_D5 is presented in Table 5.6. Since the delamination is too small for this case, the results are barely affected. This shows that the delamination must have a global size impact on the structure so that it may be detected.

### 5.2.2 Numerical Simulation Based Validation of Cylindrical Structures

Similar to the plate geometries, numerical simulation-based validation results for cylindrical structures are presented in this section. Considered cases are shown in Table 5.7 and Figure 5.5. Similar to previous validation cases, “C” denotes the structure is a cylinder and “D” denotes the case is for delamination.

Table 5.7 Considered cases for the validation of cylindrical geometries

Name	Ply Configuration	Size [mm x mm]	Delamination [mm x mm]
C_D1			-
C_D2	$[30/-30]_s$	R73x200	100x100 in middle
C_D3			50x360° in middle

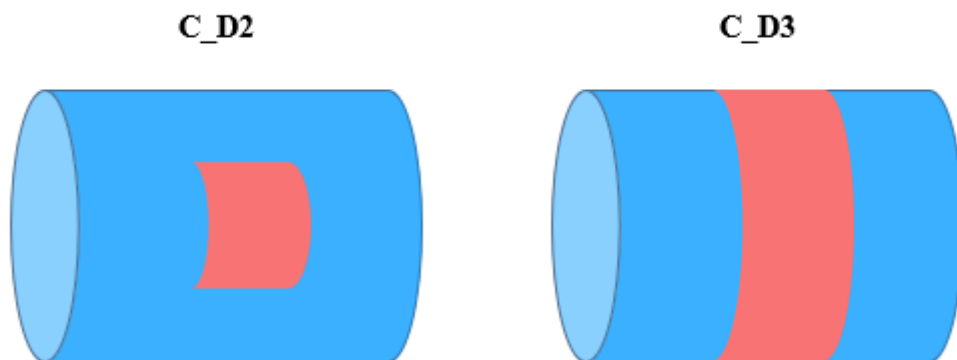


Figure 5.5 Considered cases for the validation of employed method for cylindrical geometries

Just like the previous section, case C\_D1 is the baseline with no delamination. C\_D2 employs a square delamination in the middle of the cylinder which covers 11% of the entire area, and C\_D3 employs a delamination that fully wraps around the cylinder, covering 25% of the entire area. For comparison purposes, a cubic steel

mass of 20 mm side will be employed on the delamination in the free – free boundary condition modal analysis.

Results for C\_D2 compared to C\_D1 with and without the added mass are presented in Table 5.8. As present from this table, the amplification increased the maximum absolute difference from 2% to 10.9% in natural frequencies. However, this absolute difference magnification is lower compared to the plate cases. This lower magnification can be attributed to the total mass added to the structure, as will be discussed later in this section, increasing the mass for cylinders will also increase this magnification of absolute difference.

Table 5.8 Natural frequencies of C\_D2 case compared to C\_D1

<u>No Added Mass</u>			<u>Added Mass</u>		
C_D1	C_D2	Abs. Dif.	C_D1	C_D2	Abs. Dif.
[Hz]	[Hz]	[%]	[Hz]	[Hz]	[%]
52.7	51.8	1.7	46.1	43.4	5.9
89.6	87.9	1.9	88.6	85.2	3.8
149.1	147.3	1.2	143.9	136.9	4.9
204.7	200.7	2.0	194.7	179.4	7.9
284.6	282.3	0.8	255.6	227.8	10.9
348.1	342.1	1.7	316.0	300.0	5.1

For C\_D3 configuration, two different cases are considered. In the first case, similar to previous configurations, the same mass is attached at the delamination location. The results for this case are shown in Table 5.9. Secondly, a higher mass is used which has the size 100mm x 20mm x 20mm and is steel like the previous validation cases. The results for this second case are presented in Table 5.10.

Table 5.9 Natural frequencies of C\_D3 case compared to C\_D1

<u>No Added Mass</u>			<u>Added Mass</u>		
C_D1	C_D3	Abs. Dif.	C_D1	C_D3	Abs. Dif.
[Hz]	[Hz]	[%]	[Hz]	[Hz]	[%]
52.7	50.8	3.6	46.1	41.7	9.5
89.6	85.4	4.7	88.6	82.9	6.4
149.1	143.6	3.7	143.9	131.9	8.3
204.7	194.4	5.0	194.7	175.1	10.1
284.6	275.0	3.4	255.6	215.1	15.8
348.1	332.4	4.5	316.0	293.8	7.0

Table 5.10 Natural frequencies of C\_D3 case compared to C\_D1, with a larger added mass of size 100mm x 20mm x 20mm

<u>No Added Mass</u>			<u>Added Mass</u>		
C_D1	C_D3	Abs. Dif.	C_D1	C_D3	Abs. Dif.
[Hz]	[Hz]	[%]	[Hz]	[Hz]	[%]
52.7	50.8	3.6	28.4	22.9	19.4
89.6	85.4	4.7	61.2	54.1	11.6
149.1	143.6	3.7	96.5	88.0	8.8
204.7	194.4	5.0	114.2	90.7	20.6
284.6	275.0	3.4	192.2	177.9	7.4
348.1	332.4	4.5	225.1	204.5	9.2

For the case with the previously considered added mass, the maximum absolute difference in natural frequencies increased from 5% to 15.8% as shown in Table 5.9. The increase in absolute difference is larger than the square delamination case which is expected since the delamination for this case is more aggressive. However, when a larger mass is used, this absolute difference increased to 20.6%, and on average the absolute difference in natural frequencies seemed to increase. Therefore, even on cylindrical structures, the increase in mass increases the magnification of the absolute difference.

### 5.2.3 Numerical Simulation Based Validation of Pressure Vessel Structures

Similar to the previous sections, validation of the employed method on pressure vessel type structures is presented in this section. The considered cases are presented in Table 5.11.

Table 5.11 Considered cases for the validation of pressure vessel geometries

Name	Ply Configuration	Size [mm x mm]	Delamination [mm x mm]
PV_D1	<i>XXO</i>	Figure 3.20	-
PV_D2			40x40 in middle

A similar naming convention is used in Table 5.11 where “PV” denotes the structure is a pressure vessel and “D” denotes that the case is considered for delamination identification. PV\_D1 is chosen as the baseline and PV\_D2 is the case with the delamination.

The results for these cases are presented in Table 5.12, in a similar fashion to previous sections. A cubic steel mass of 20 mm edge length is used in the free – free boundary condition analysis of the structure. The added mass for the pressure vessel causes a huge amplification in the absolute difference of natural frequencies, increasing the maximum absolute difference from 4.4% to 22.3%. However, the main cause of this is the existence of the local modes, which were not mainly present prior. For the previously considered geometries, the structures were still exhibiting their global mode shapes whereas for pressure vessels, all three first modes are local modes around the added mass. These mode shapes are shown in Figure 5.6.

Table 5.12 Natural frequencies of PV\_D2 case compared to PV\_D1

<u>No Added Mass</u>			<u>Added Mass</u>		
PV_D1	PV_D2	Abs. Dif.	PV_D1	PV_D2	Abs. Dif.
[Hz]	[Hz]	[%]	[Hz]	[Hz]	[%]
1309	1252	4.4	578	471	18.5
1801	1808	0.4	721	560	22.3
2370	2304	2.8	1010	787	22.1

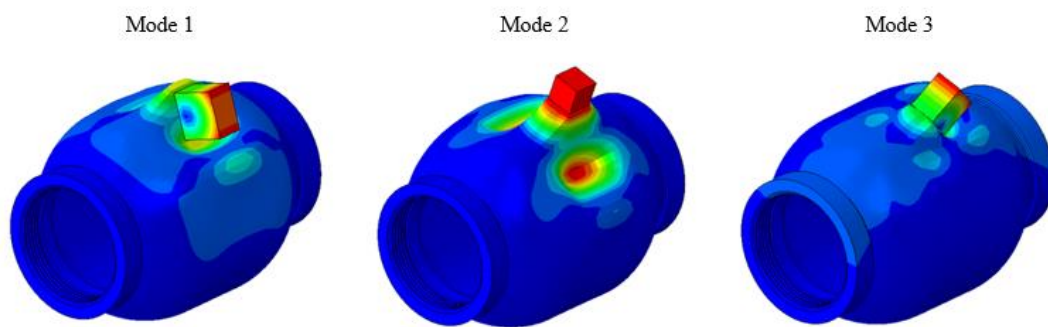


Figure 5.6 Mode shapes of the considered pressure vessels with added mass

### 5.3 Experiment Based Validation for Delamination Identification

Similar to the validation methodology presented in chapters 3 and 4, an experiment-based validation is also conducted on the delamination identification method and the results are presented in this section, divided per considered geometries below.

To introduce delamination in the structure, a Teflon film is used. Some of the delaminations created this way are shown in Figure 5.7. Then, these delaminations are inserted during the filament winding process, so that they create a gap between the layers, as shown in Figure 5.8. Using this method, the created gaps are visible in an ultrasonic C-scan. A calibration specimen was prepared with several delaminations as shown in Figure 5.9 for a pressure vessel to assess if the method can successfully prepare delaminations.



Figure 5.7 Teflon films employed to create delamination on structures

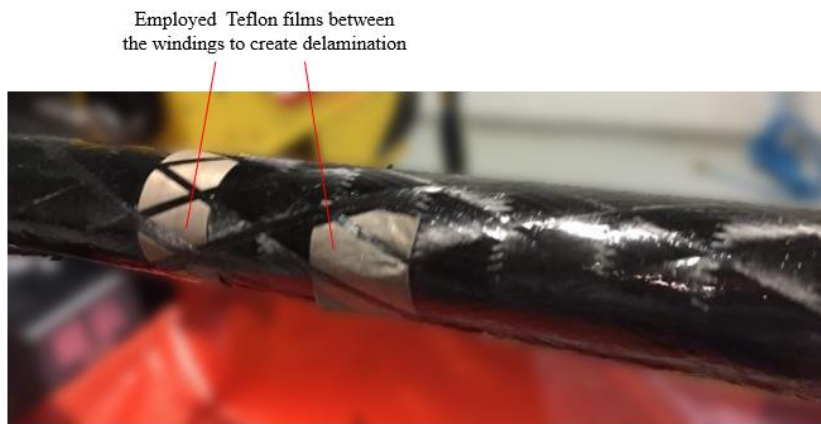


Figure 5.8 Insertion of teflon films during the filament winding process to create delamination

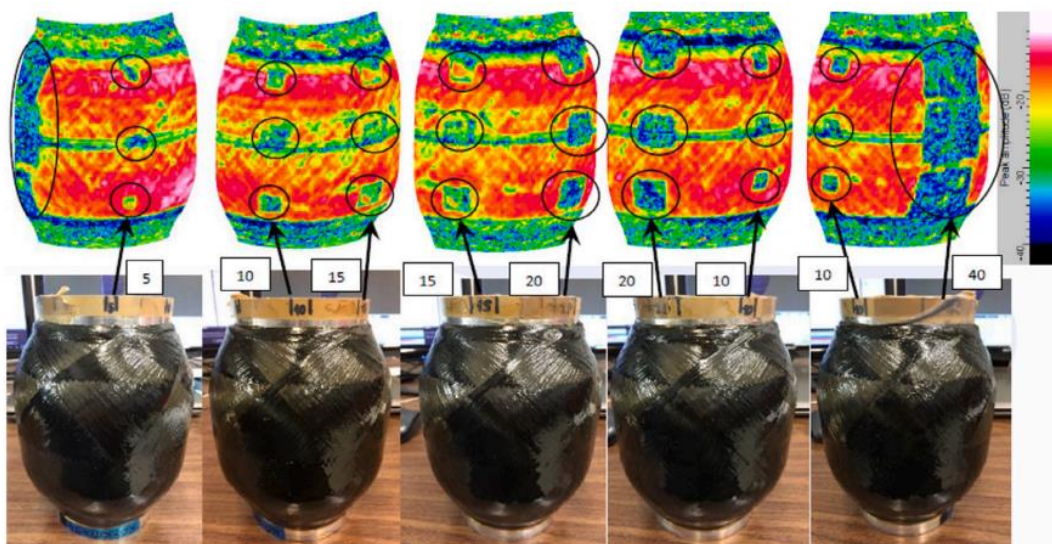


Figure 5.9 Ultrasonic C-scan results for a pressure vessel with various sized added delaminations [76]



### 5.3.1 Experiment Based Validation of Plate Structures

Previously, various cases for the plate geometries were considered under numerical-based validation in section 5.2.1. In this section, P\_D1, P\_D2, P\_D4, and P\_D5 from Table 5.1 will be validated experimentally. The employment of the attached steel cube mass of 20 mm edge length is shown in Figure 5.10. Experimentally obtained results for the plate structures are presented in Table 5.13, Table 5.14, and Table 5.15.

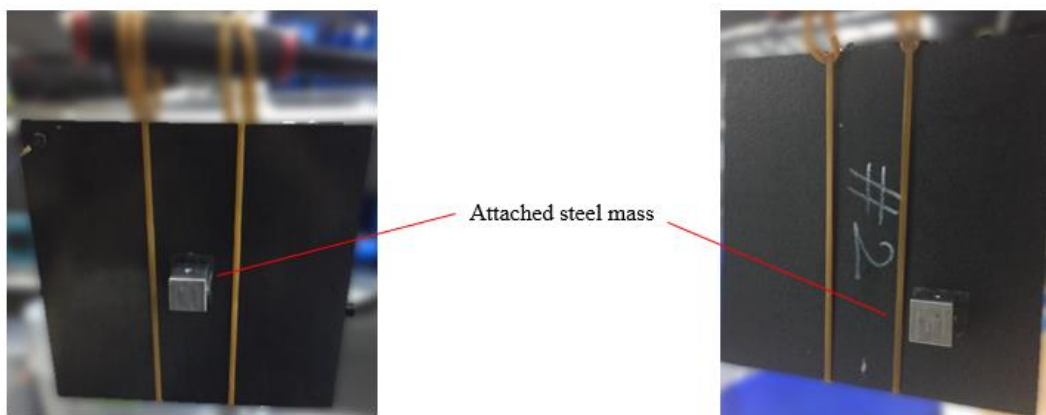


Figure 5.10 Attached steel mass to the structure

Table 5.13 Experimentally obtained natural frequencies for P\_D2 and P\_D1

<u>No Added Mass</u>			<u>Added Mass</u>		
P_D1	P_D2	Abs. Dif.	P_D1	P_D2	Abs. Dif.
[Hz]	[Hz]	[%]	[Hz]	[Hz]	[%]
43.3	43.4	0.2	49.1	48.2	1.8
102.5	102.5	0.0	85.0	83.1	2.2
135.1	135.3	0.1	132.8	132.7	0.1
230.2	230.8	0.3	196.2	181.4	7.5
245.5	246.2	0.3	231.2	217.9	5.8

Table 5.14 Experimentally obtained natural frequencies for P\_D4 and P\_D1

<u>No Added Mass</u>			<u>Added Mass</u>		
P_D1	P_D4	Abs. Dif.	P_D1	P_D4	Abs. Dif.
[Hz]	[Hz]	[%]	[Hz]	[Hz]	[%]
43.3	43.4	0.2	46.5	45.1	3.0
102.5	102.5	0.0	95.5	93.1	2.5
135.1	135.3	0.1	136.1	130.0	4.5
230.2	230.8	0.3	200.1	178.2	10.9
245.5	246.2	0.3	242.1	213.0	12.0

Table 5.15 Experimentally obtained natural frequencies for P\_D5 and P\_D1

<u>No Added Mass</u>			<u>Added Mass</u>		
P_D1	P_D5	Abs. Dif.	P_D1	P_D4	Abs. Dif.
[Hz]	[Hz]	[%]	[Hz]	[Hz]	[%]
43.3	43.4	0.2	49.1	49.1	0.0
102.5	102.5	0.0	85.0	85.1	0.1
135.1	135.3	0.1	132.8	132.8	0.0
230.2	230.8	0.3	196.2	196.1	0.1
245.5	246.2	0.3	231.2	231.3	0.0

When compared to the numerical results, the amplification caused by the added mass is lower. However, the effect of delamination itself is also lower on the natural frequencies. This is mainly due to the unconsidered nonlinear effects in the analysis. However, adding a mass still amplifies the absolute difference, and while the case without the mass is almost unseparable from each other, with the added mass the absolute difference in natural frequency increases to the orders of 10%. For P\_D5, the case with the smallest delamination, since the delamination did not affect the structure majorly, the added mass did not help the amplification of this effect.

Lastly, to identify the effect of the added mass that is not applied to a delamination region, P\_D4 is subjected to modal tests again but this time with the added mass in

the opposite side of the plate, as shown in Figure 5.4. Results for this case are presented in Table 5.16. As expected, for this case, the delamination cannot be detected since the magnification of the delamination region does not occur. The absolute difference in natural frequencies are similar to the case with no added mass.

Table 5.16 Experimentally obtained natural frequencies for P\_D4 and P\_D1 with added mass on the opposite side of the plate

<u>No Added Mass</u>			<u>Added Mass</u>		
P_D1	P_D4	Abs. Dif.	P_D1	P_D4	Abs. Dif.
[Hz]	[Hz]	[%]	[Hz]	[Hz]	[%]
43.3	43.4	0.2	46.5	46.5	0.0
102.5	102.5	0.0	95.5	95.4	0.1
135.1	135.3	0.1	136.1	135.9	0.1
230.2	230.8	0.3	200.1	199.7	0.2
245.5	246.2	0.3	242.1	241.4	0.3

### 5.3.2 Experiment Based Validation of Cylindrical Structures

Similar to the plate structures, experimental validation of the cylindrical structures is presented in this section. For this, C\_D1 and C\_D3 cases are considered from Table 5.7. Attached mass for this case on the cylinder is shown in Figure 5.11.

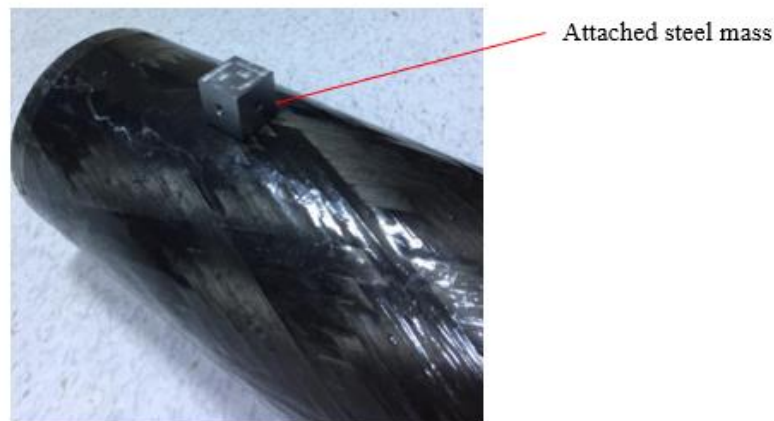


Figure 5.11 Attached steel mass to the cylinder

The results of the experiments are presented in Table 5.17. Similar to the plates, the absolute difference in natural frequencies are less prominent than the numerical simulation cases. However, contrary to the plate cases, the added mass has very low magnification on the absolute difference in natural frequencies. Although cylindrical case had the lowest magnification effect for all considered geometries in numerical simulations, the experimental results barely present a 1% difference in natural frequencies compared to a no additional mass case.

The mentioned small magnification may be caused by several effects. Firstly, in the numerical analysis the nonlinear effects weren't considered, presenting some absolute difference. Secondly, although a teflon film is inserted in the structure, matrix material may still generate weak bonds with the Teflon film, hence limiting the delamination.

To combat the second reason, the tests are repeated with 2 steel masses attached at the same location, which should provide a larger magnification. Results of this case is presented in Table 5.18. In this table, the maximum absolute difference has increased to 4% as opposed to the previous 1.8%. As expected, the magnification of the absolute difference in natural frequencies increased. This means that the layers have not bonded to the Teflon film, and a delamination exists as otherwise the absolute difference would have stayed at a similar level. Therefore, the main reason behind the small magnification in absolute difference must be the unconsidered nonlinear effects.

Table 5.17 Experimentally obtained natural frequencies for C\_D3 and C\_D1

<u>No Added Mass</u>			<u>Added Mass</u>		
C_D1	C_D3	Abs. Dif.	C_D1	C_D3	Abs. Dif.
[Hz]	[Hz]	[%]	[Hz]	[Hz]	[%]
52.7	52.5	0.4	46.1	45.8	0.7
89.7	89.4	0.3	88.7	88.1	0.7
149.1	148.7	0.3	144.0	142.9	0.8
204.8	203.9	0.4	194.9	192.4	1.3
284.7	282.8	0.7	256.1	251.4	1.8

Table 5.18 Experimentally obtained natural frequencies for C\_D3 and C\_D1 with two steel masses added

<u>No Added Mass</u>			<u>Added Mass</u>		
C_D1	C_D3	Abs. Dif.	C_D1	C_D3	Abs. Dif.
[Hz]	[Hz]	[%]	[Hz]	[Hz]	[%]
52.7	52.5	0.4	46.1	45.4	1.5
89.7	89.4	0.3	88.7	87.3	1.6
149.1	148.7	0.3	144.0	141.0	2.1
204.8	203.9	0.4	194.9	190.8	2.1
284.7	282.8	0.7	256.1	245.8	4.0

### 5.3.3 Experiment Based Validation of Pressure Vessel Structures

In this section, PV\_D1 and PV\_D2 presented in Table 5.11 will be validated experimentally. The attached steel mass on the pressure vessel is shown in Figure 5.12.

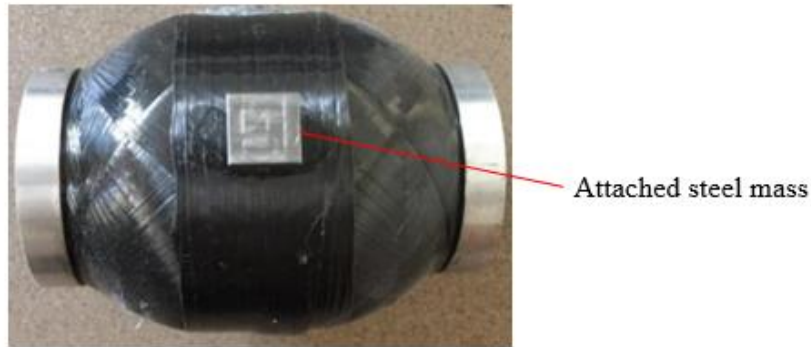


Figure 5.12 Attached steel mass to the pressure vessel

Results of the experiments for the considered pressure vessels are presented in Table 5.19. Similar to the other geometries, although the difference in natural frequencies is lower, the added mass helps the magnification of it. This leads to the maximum of 3% absolute difference in natural frequency going up to 10.9%.

Table 5.19 Experimentally obtained natural frequencies for PV\_D2 and PV\_D1

<u>No Added Mass</u>			<u>Added Mass</u>		
PV_D1	PV_D2	Abs. Dif.	PV_D1	PV_D2	Abs. Dif.
[Hz]	[Hz]	[%]	[Hz]	[Hz]	[%]
1257	1238	1.5	547	501	8.4
1728	1682	2.7	699	628	10.2
2147	2082	3.0	952	848	10.9

#### 5.4 Evaluation of the Performance of Employed Method for Identification of Delamination

In this chapter, a previously considered method generated for beam structures is applied to several other geometries such as plates, cylinders, and pressure vessels, in order to determine the delaminations on the structure. A mass is added to the delamination region to amplify the effects of the delamination on the modal properties. The difference in the natural frequency was chosen as the main parameter to determine the existence of a delamination.

For quite sizable delaminations compared to the structure, the method works as expected on all the geometries considered. Compared to experimental results, numerical results showed a higher magnification of absolute difference in natural frequencies. The lowest magnification was encountered on cylindrical geometries, where an additional mass was required to increase the amplification of the absolute difference in natural frequencies.

The main downside of this method is that it can assess the delaminations locally, as demonstrated with an example on plate structures. If the mass is applied to a region that does not have delamination, then the structure will behave as if it had no delamination. Therefore, the attached mass needs to be applied at several spots of interest in the structure to assess it completely. Also, for comparison purposes, a healthy structure free of delamination is required as baseline for comparison. In the absence of such structure, the numerical results for the healthy structure may be used, as they are very close to the results obtained experimentally.

Another weakness of this method lies within the bonding of the attached mass. Since to assess the structure entire the mass has to be applied several times over the structure, a weaker bondage agent might be preferred. However, when such an agent is employed with a structure that has high natural frequencies, it may interfere with the results, as the quality of the bonding might affect the natural frequencies obtained experimentally. Therefore, a strong bonding element that can be released without harming the composite material must be chosen in this application.





## CHAPTER 6

### CONCLUSION

In this thesis, several manufacturing errors have been identified by either proposed novel methods or previously applied methods in the literature for different geometries. The considered manufacturing defects were errors in ply orientations, errors in volume fraction and hence the average thickness, and delamination. All of these defects were identified successfully and non-destructively by applying the proposed and employed methods in both numerical simulations and in modal test-based experiments. The manufacturing effects were considered individually, and different methods were proposed or employed in order to assess them.

For identification of ply orientation errors in the structure, a novel method was proposed. This method employs the natural frequencies of the unknown structure, and then estimates a range for the  $D^*$  parameters from the first natural frequency. Then, these parameters are optimized considering the physicality of the relationship between each  $D^*$  parameters and using the rest of the measured natural frequencies. This final set of  $D^*$  parameters are then employed with an ANN in order to identify each ply orientation. A singular ANN was not enough to solely identify all the ply orientations, so an algorithm was generated in which the search range of the ANN was reduced with each output, until convergence of the ply orientations was achieved.

For identification of volume fraction and average thickness, the novel method proposed for the identification of ply orientations were extended to include the effects of volume fraction. This led to the method not determining the ply orientations correctly, as it only determines pseudo-orientations which do not correlate to the real ones. However, it was able to identify the volume fraction and average thickness with very good accuracy. An additional optional step was

considered at the end of the method, where parameters were calculated at the newly found volume fraction, and then the method proposed for identification of ply orientations could be applied on top. This way, both the volume fractions and ply orientations could be obtained.

For identification of delamination, a previously considered method for beam structures was extended and applied to several other geometries. This method employs an additional mass on the structure to amplify the effects caused by the delamination. Effect of increased mass and location of the mass were also considered in application of this method.

Aside from the general summary presented above, there are specific remarks that should be emphasized as the result of this thesis. These remarks are presented below for each considered manufacturing defect.

## 6.1 Concluding Remarks

In application of the proposed method for identification of ply orientations, several outcomes were attained. These outcomes can be summarized as below.

- The method is sensitive to the estimated area for  $D^*$  parameters. Therefore, a more accurate estimation of the area for  $D^*$  parameters will increase the accuracy of the method even further.
- Although an optimization scheme based on the physicality of the  $D^*$  parameters were applied in order to find the singular quantity that represents the laminate entire, other optimization methods may also be considered in order to obtain these quantities. In fact, a cross-check mechanism with several methods might yield better results, as the later stage of the proposed method is very sensitive to the optimized  $D^*$  parameters obtained.
- The employment of an ANN with reduced search range for each consequent step works excellently to identify the ply orientations. However, due to the requirement of several search range reductions leading to training of new

ANNs, especially for laminates with a large number of plies this process can be slow, resulting in order of minutes and maybe hours for large laminates.

- Due to the nonlinearity of the entire process with multiple different optimizations, several repetitions of the last step of the method to obtain the ply orientations is necessary to eliminate any outlier solutions and improve precision.
- Both the accuracy of the ANN and the estimated area for  $D^*$  parameters depend on the previously generated dataset for different ply configurations. Hence, increasing this dataset will help the method's accuracy. Although cumbersome, it only has to be done a single time for a structure, which can then be used readily.
- It is of most importance to feed the ANN with a dataset that contains little false-positive information. As due to the ply configuration and geometry, the same setup may be identified as two different setups and be introduced into the ANN, which will reduce its accuracy.
- If any additional information is present for the structure at hand that might limit the possible orientations, it should be used to provide better and faster estimates.

The outcomes of the proposed method for identification of volume fraction and average thickness are presented below.

- Outcomes for the identification of ply orientation are also applicable to this method, as they are sharing the same principles.
- Due to the consideration of many different volume fractions, the newly estimated area for  $D^*$  parameters now result in pseudo-orientations. This can later be eliminated by the inclusion of an additional step.
- The method assesses the structure as a whole, so local variations in the volume fraction may not be detected by this method, unless such cases are considered individually as the input for both estimated area of  $D^*$  parameters and ANN.

- The method is also dependent on the micromechanical model used. If a single micromechanical model may not represent all the possible scenarios for your manufacturing standards, a proper set employing either a different micromechanical model or several models should be used.

The outcomes of the employed method for identification of delamination are presented below.

- Delaminations may be identified successfully if the mass is attached at the delamination region, regardless of the geometry of the structure.
- Different geometries, sizes of delamination or ply layups may require different amounts of added mass to the delamination region in order to amplify the error in natural frequencies.
- Very small delaminations that do not cause any impact on modal properties of the structure cannot be detected through this method.
- Due to not knowing if a delamination is present in the structure prior, the added mass must be applied at several regions, or the key regions in the structure.
- The effect of added mass is also either reduced or amplified by the mode shape. If the delamination exists in a place where the mode shapes are relatively low in magnitude, more mass is required to assess the region accurately.

Considering the outcomes and remarks above, proposed and employed methods are strong contenders to currently used error identification methods in the industry. However, there is always more room for improvement. Several improvements have been encountered during this research for specific cases but ultimately was not used for the final results. In the following section, these encountered issues are discussed.

## 6.2 Future Work

Most of the improvements foreseen for the work were encountered for the proposed methods for identification of ply orientations or volume fractions and average thicknesses. These issues may be summarized as below.

- When considering very basic structures such as plates, due to the ease of equations it may be considered in a more analytical approach. For the case of such basic structures, it was shown by the author that the stiffness matrix may directly be obtained through manipulations on the equations describing modal characteristics [84]. Since the geometry of the structure is known, this stiffness matrix can then be directly turned into the optimized  $D^*$  parameters. This eliminates any need for previous consideration of different ply orientations or the optimization scheme to obtain the parameters to be fed into the ANN, which speeds up the process a lot. The process described may even be altered to weaken the form and make it more flexible to apply to other structures as well.
- During the optimization step of ply orientations, an ANN was employed in this work. However, prior to this, different optimization schemes were also used. Genetic algorithm was the best contender to the use of ANN, but it only worked accurately for small ranges of ply orientations. Another plus on the size of the genetic algorithm was its speed, as it was several orders of magnitude times faster than the ANN for a single solution. Hence, the range reduction may be employed with ANN and the final search may be conducted with a genetic algorithm, eliminating the last ANN step to speed up the process, and also eliminating the need for several runs of the ANN step, as genetic algorithm always provided unique and accurate solutions.



## REFERENCES

- [1] Park D.-W., Oh G.-H., Kim H.-S., 2019, Predicting the stacking sequence of E-glass fiber reinforced polymer (GFRP) epoxy composite using terahertz time-domain spectroscopy (THz-TDS) system, *Composites Part B*, 177, doi: 10.1016/j.compositesb.2019.107385
- [2] Nelson L, Smith R, Mienczakowski M. Ply-orientation measurements in composites using structure-tensor analysis of volumetric ultrasonic data. *Compos Part A: Appl Sci Manuf* 2018;104:108–19, doi: 10.1016/j.compositesa.2017.10.027
- [3] Katunin A., Przystalka P., 2014, Damage assessment in composite plates using fractional wavelet transform of modal shapes with optimized selection of spatial wavelets, *Engineering Applications of Artificial Intelligence*, Vol. 30, p. 73-85
- [4] Gholizadeh S., 2016, A review of non-destructive testing methods of composite materials, *Procedia Structural Integrity*, 1, doi: 10.1016/j.prostr.2016.02.008
- [5] Quanjin M., Rejab M.R.M., Idris M.S., Zhang B., Kumar N.M., 2019, Filament Winding Technique: SWOT Analysis and Applied Favorable Factors, *SCIREA Journal of Mechanical Engineering*, Vol. 3
- [6] Zou Y., Tong L., Steven G.P., 1999, Vibration-Based Model-Dependent Damage (Delamination) Identification and Health Monitoring for Composite Structures - A Review, *Journal of Sound and Vibration*, Vol. 230, p. 357- 378
- [7] Carden E.P., Fanning P., 2004, Vibration Based Condition Monitoring: A Review, *Structural Health Monitoring*, Vols. 3-4, p. 355-377

- [8] Fan W., Qiao P., 2010, Vibration-based Damage Identification Methods: A Review and Comparative Study, *Structural Health Monitoring*, Vol. 10, p. 83-129
- [9] Salawu O.S., 1995, Detection of structural damage through changes in frequency: a review, *J. Engineering Structures*, Vol. 19, p. 718-723
- [10] Dolinski L., Krawczuk M., Zak A., 2018, Detection of Delamination in Laminate Wind Turbine Blades Using OneDimensional Wavelet Analysis of Modal Responses, *Shock and Vibration*, Vol. 2018
- [11] Gadelrab R.M., 1996, The Effect of Delamination on the Natural Frequencies of a Laminated Composite Beam, *Journal of Sound and Vibration*, Vol. 197, p. 283-292
- [12] Cawley P. Adams R.D., 1979, A Vibration Technique for Non-Destructive Testing of Fibre Composite Structures, *J. Composite Materials*, Vol. 13, p. 161
- [13] Cawley P., Adams R.D., 1978, The Predicted and Experimental Natural Modes of Free-Free CFRP Plates, *J. Composite Materials*, Vol. 12, p. 336
- [14] Ullah I., Sinha J.K., 2013, A Novel Method for Delamination Detection in Composites, *International Journal of Innovation and Applied Studies*, Vol. 2, p. 34-42
- [15] Dawood T.A., Shenoï R.A., Veres S.M., Şahin M., Gunning M.J., 2003, Damage detection in a sandwich composite beam using wavelet transforms, *Smart Structures and Materials*, Vol. 5049, pp. 706-717
- [16] Dawood T., Shenoï A.R., Veres S.M., Şahin M., Gunning M.J., 2004, Damage Characterization in FRP Sandwich Beams using a Wavelet based Multifractal Approach
- [17] Dawood T., Shenoï A.R., Veres R.A., Şahin M., 2004, Low Level Damage Characterisation in FRP Sandwich Beams using the



- Lipschitz Exponent, Second European Workshop on Structural Health Monitoring, 7, pp. 661-668
- [18] Friswell M.I., Penny J.E.T., Garvey S.D., 1998, A combined genetic and eigensensitivity algorithm for the location of damage in structures, *Computers and Structures*, Vol. 69, p. 547-556
- [19] Hamey C.S., Lestari W., Qiao P., Song G., 2004, Experimental Damage Identification of Carbon/Epoxy Composite Beams Using Curvature Mode Shapes, *Structural Health Monitoring*, Vols. 3-4, p. 333-353
- [20] Shams S., Torabi A.R., Narab M.F., Atashgah M.A.A., 2021, Free vibration analysis of a laminated beam using dynamic stiffness matrix method considering delamination, *Thin-Walled Structures*, Vol. 166
- [21] Lestari W., Qiao P., Hanagud S., 2007, Curvature Mode Shape-based Damage Assessment of Carbon/Epoxy Composite Beams, *Journal of Intelligent Material Systems and Structures*, Vol. 18
- [22] Ratcliffe C.P., Bagaria W.J., 1998, Vibration Technique for Locating Delamination in a Composite Beam, *AIAA Journal*, Vol. 36
- [23] Vo-Duy T., Nguyen-Minh N., Dang-Trung H., Tran-Viet A., Nguyen-Thoi T., 2015, Damage assessment of laminated composite beam structures using damage locating vector (DLV) method, *Front. Struc. Civ. Eng.* Vol. 9, p. 457
- [24] Aoki Y., Byon O., 2001, Damage detection of CFRP pipes and shells by using localized flexibility method, *Adv. Composite Mater.*, Vol. 10, p. 189-198
- [25] Pandey A.K., Biswas M., 1991, Damage Detection in Structures Using Changes in Flexibility, *Journal of Sound and Vibration*, Vol. 169, p. 3-17

- [26] Kessler S.S., Spearing S.M., Atalla M.J., Cesnik C.E.S., Soutis C., 2001, Damage detection in composite materials using frequency response methods, *Composites: Part B*, Vol. 33, p. 87-95
- [27] Zak A., Krawczuk M., Ostachowicz W., 2000, Numerical and experimental investigation of free vibration of multilayer delaminated composite beams and plates, *Computational Mechanics*, Vol. 26, p. 309-315
- [28] Yang C., Oyadiji S.O., 2021, A new delamination making technique for cured glass/epoxy samples and validation using vibration characteristics, *Composite Structures*, Vol. 257
- [29] Kumar M., Shenoj R.A., Cox S.J., 2009, Experimental validation of modal strain energies based damage identification method for a composite sandwich beam, *Composites Science and Technology*, Vol. 69, p. 1635-1643
- [30] Hu H., Wang B., Lee C., 2006, Damage Detection of Surface Crack in Composite Quasi-isotropic Laminate using Modal Analysis and Strain Energy Method, *Key Engineering Materials*, Vols. 306-308, p. 757-762
- [31] Vo-Duy T., Ho-Huu V., Dang-Trung H., Dinh-Cong, D., Nguyen-Thoi T., 2016, Damage Detection in Laminated Composite Plates Using Modal Strain Energy and Improved Differential Evolution Algorithm, *Procedia Engineering*, Vol. 142, p. 182-189
- [32] Arumugam V., Kumar C.S., Santulli C., Sarasini F., Stanley A.J., n.d., Identification of Failure Modes in Composites from Clustered Acoustic Emission Data Using Pattern Recognition and Wavelet Transformation, *Arab J. Sci. Eng.*, Vol. 38, p. 1087-1102
- [33] Sung D., Kim C., Hong C., 2001, Monitoring of impact damages in composite laminates using wavelet transform, *Composites: Part B*, Vol. 33, p. 35-43

- [34] Smith R.A., n.d., Composite Defects and Their Detection, Materials Science and Engineering, Vol. 3
- [35] Mahmud M.F., Bakar E.A., Othman A.R., 2016, Defect Detection of Fiberglass Composite Laminates (FGCL) with Ultrasonic A-Scan Signal Measurement, IOP Conf. Series: Materials Science and Engineering, Vol. 114
- [36] Ng S.C., Ismail N., Aidy A., Sahari B., Yusof J.M., 2013, Ultrasonic NDE for Internal Defect Detection in Multilayered Composite Materials by Multiresolution Signal Decomposition, Journal of Applied Sciences, Vol. 13, p. 87-94
- [37] Hudson T.B., Hou T., Grimsley B.W., Yuan F., 2019, Detection of CFRP Composite Manufacturing Defects Using a Guided Wave Approach, NASA Langley Research Center, Advanced Materials and Processing Branch
- [38] Taheri H., Hassen A.A., 2019, Nondestructive Ultrasonic Inspection of Composite Materials: A Comparative Advantage of Phased Array Ultrasonic, Applied Sciences, Vol. 9
- [39] Wang X., Zhou Y., 2018, System of ultrasonic non-destructive testing of carbon fiber composite defects, Functional Materials, Vol. 25, p. 180-183
- [40] Su Z., Ye L., Lu Y., 2006, Guided Lamb waves for identification of damage in composite structures: A review, Journal of Sound and Vibration, Vol. 295, p. 753-780
- [41] Kirikera G.R., Schulz M.J., Sundaresan M.J., 2007, Multiple Damage Identification on a Wind Turbine Blade using Structural Neural System, SPIE, Sensor Systems and Networks: Phenomena, Technology, and Applications for NDE and Health Monitoring, Vol. 6530
- [42] Waghulde K.B., Kumar B., 2014, Vibration Analysis for Damage Detection in Composite Plate by Using Piezoelectric Sensors,

International Journal of Mechanical Engineering and Technology (IJMET), Vol 5., pp. 27-35

- [43] Gamier C., Pastor M., Emya F., Lorrain B., 2011, The detection of aeronautical defects in situ on composite structures using Non Destructive Testing
- [44] Ramos da Silva A.J., 2016, Detection and Characterization of Defects in Composite Materials Using Thermography, Faculdade de Engenharia da Universidade do Porto
- [45] Beattie A.G., Rumsey M., n.d., Nondestructive Evaluation of Wind Turbine Blades Using an Infrared Camera, American Institute of Aeronautics and Astronautics
- [46] Pastor M.L., Pescay C., Garnier C., n.d., Comparison of two Nondestructive Tests in Carbon/Epoxy Composites, Journal of Materials Science and Engineering, Vol. 4
- [47] Soete J., Badoux B., Swolfs Y., Gorbatiikh L., Wevers M., 2019, Defect Detection in 3D printed carbon fibre composites using X-ray Computed Tomography, 9 th Conference on Industrial Computed Tomography
- [48] Meitzler T.J., Franks L.P., Ellingston W.A., Koehl E.R., Steckenrider J.S., 2010, Identification of NDE Methods for Inspection of Multi-Layer Ceramic Composite Armor
- [49] Hung Y.Y., 1999, Applications of digital shearography for testing of composite structures, Composites: Part B, Vol. 30, p. 765-773
- [50] Katunin A., Danczak M., Kostka P., 2014, Automated Identification of internal defects in composite structures using computed tomography and 3D wavelet analysis, Archives of Civil and Mechanical Engineering, Vol. 15, p. 436- 448
- [51] Foss P.H., Tseng H.-C., Snawerdt J., Chang Y.-J., Yang W.-H., Hsu C.-H., 2014, Prediction of Fiber Orientation Distribution in Injection Molded Parts Using Moldex3D Simulation

- [52] Tseng H.-C., Chang R.-Y., Hsu C.-H., 2017, Numerical predictions of fiber orientation and mechanical properties for injection-molded long glass-fiber thermoplastic composites, *Composites Science and Technology*, doi: 10.1016/j.compscitech.2017.07.026
- [53] Tseng H.-C., Chang R.-Y., Hsu C.-H., 2017, Improved fiber orientation predictions for injection molded fiber composites, *Composites: Part A*, 99, doi: 10.1016/j.compositesa.2017.04.004
- [54] Tseng H.-C., Goto M., Chang R.-Y., Hsu C.-H., 2017, Accurate Predictions of Fiber Orientation and Mechanical Properties in Long-Fiber-Reinforced Composite With Experimental Validation, *Polymer Composites*, DOI 10.1002/pc.24361
- [55] Song Y., Gandhi U., Pérez C., Osswald T., Vallury S., Yang A., 2017, Method to account for the fiber orientation of the initial charge on the fiber orientation of finished part in compression molding simulation, *Composites: Part A*, doi: 10.1016/j.compositesa.2017.05.021
- [56] Baranowski T., Dobrovolskij D., Dremel K., Hölzing A., Lohfink G., Schladitz K., Zabler S., 2019, Local fiber orientation from X-ray region-of-interest computed tomography of large fiber reinforced composite components, *Composites Science and Technology*, 183, doi: 10.1016/j.compscitech.2019.107786
- [57] Quintana M.C., Frontini P.M., Arriaga A., Plank B., Major Z., 2020, Fiber Orientation Distribution Predictions for an Injection Molded Venturi-Shaped Part Validated Against Experimental Micro-Computed Tomography Characterization. *Front. Mater.* 7:169. doi: 10.3389/fmats.2020.00169
- [58] Kratmann K.K., Sutcliffe M.P.F., Lilleheden L.T., Pyrz R., Thomsen O.T., 2009, A novel image analysis procedure for measuring fibre misalignment in unidirectional fibre composites, *Composites Science and Technology*, 69

- [59] Creighton C.J., Sutcliffe M.P.F., Clyne T.W., 2001, A multiple field image analysis procedure for characterisation of fibre alignment in composites, *Composites: Part A*, 32
- [60] Sabiston T., Inal K., Lee-Sullivan P., 2020, Application of Artificial Neural Networks to predict fibre orientation in long fibre compression moulded composite materials, *Composites Science and Technology*, 190, doi: 10.1016/j.compscitech.2020.108034
- [61] Bleiziffer P., Hofmann J., Zboray R., Wiege T., Herger R., 2021, Predicting the fiber orientation in glass fiber reinforced polymers using the moment of inertia and convolutional neural networks, *Engineering Applications of Artificial Intelligence*, Vol. 104
- [62] Zhang Z., Pan J., Luo W., Ramakrishnan K.R., Singh H.K., 2019, Vibration-based delamination detection in curved composite plates, *Composites Part A*, Vol 119
- [63] Şahin M., Sheno A.R., 2002, Damage Detection in FRP Laminated Beams Using Neural Networks, *First European Workshop on Structural Health Monitoring*, 10-12, pp. 726-733
- [64] Şahin M., R.A., Sheno, 2003, Quantification and localisation of damage in beam-like structures by using artificial neural networks with experimental validation, *Engineering Structures*, Vol. 25, pp. 1785-1802
- [65] Şahin M., Sheno R.A., 2003, Vibration-based damage identification in beam-like composite laminates by using artificial neural networks, *Proceedings of the Institution of Mechanical Engineers, Part C*, Vol. 217
- [66] Şahin M., 2010, Vibration-based Damage Identification in Sandwich Beams using Artificial Neural Networks, *Proceedings of the Tenth International Conference on Computational Structures Technology*, doi:10.4203/ccp.93.47

- [67] Mook G., Lange R., Koeser O., 2001, Non-destructive characterisation of carbon-fibre-reinforced plastics by means of eddy-currents, *Composites Science and Technology*, 61, doi: 10.1016/s0266-3508(00)00164-0
- [68] Wu D., Cheng F., Yang F., Huang C., 2019, Non-destructive testing for carbon-fiber-reinforced plastic (CFRP) using a novel eddy current probe, *Composites Part B*, 177, doi: 10.1016/j.compositesb.2019.107460
- [69] Wu D., Cheng F., Yang J., Yang F., 2020, Self-resonance eddy-current testing method in noncontact detection of carbon fiber reinforced plastics, *Composite Structures*, doi: 10.1016/j.compstruct.2020.113247
- [70] Kollar L.P., Springer G.S., 2003, *Mechanics of Composite Structures*, Cambridge University Press
- [71] Mathworks, 2021, Matlab
- [72] Dassault Systèmes, 2020, Abaqus CAE
- [73] Vasiliev V.V., Krikanov A.A., Razin A.F., 2003, New generation of filament-wound composite pressure vessels for commercial applications, *Composite Structures*, Vol. 62, doi: 10.1016/j.compstruct.2003.09.019
- [74] Zu L., Koussios S., Beukers A., 2011, Integral Design for Filament-Wound Composite Pressure Vessels, *Polymers & Polymer Composites*, Vol. 19
- [75] Wang R., Jiao W., Liu W., Yang F., 2011, Dome Thickness Prediction of Composite Pressure Vessels by a Cubic Spline Function and Finite Element Analysis, *Polymers & Polymer Composites*, Vol. 19
- [76] Yurdakul K., 2022, The Influence of manufacturing defects on structural performance of composite overwrapped pressure vessels, METU

- [77] Jing Z., Sun Q., Zhang Y., Liang K., Li X., 2021, Stacking sequence optimization of composite cylindrical panels by sequential permutation search and Rayleigh-Ritz method, *European Journal of Mechanics / A Solids*, 88, doi: 10.1016/j.euromechsol.2021.104262
- [78] Vignoli L.L., Savi M.A., Pacheco P.M.C.L., Kalamkarov A.L., 2019, Comparative analysis of micromechanical models for the elastic composite laminae, *Composites Part B*, Vol. 174, doi: 10.1016/j.compositesb.2019.106961
- [79] Chamis C.C., 1987, Simplified Composite Micromechanics For Predicting Microstresses, *Journal of Reinforced Plastics and Composites*, Vol.6
- [80] Chang C., Zhang Y., Wang H., 2019, Micromechanical modeling of unidirectional composites with random fiber and interphase thickness distributions, *Arch. Appl. Mech.*, doi: 10.1007/s00419-019-01595-0
- [81] Heidari-Rarani M., Bashandeh-Khodaei-Naeini K., Mirkhalaf S.M., 2018, Micromechanical modeling of the mechanical behavior of unidirectional composites – A comparative study
- [82] Bacarreza O., Abe D., Aliabadi M.H., Ragavan N.K., 2013, Micromechanical Modelling of Advanced Composites, *Journal of Multiscale Modelling*, doi: 10.1142/S1756973712500059
- [83] Yang C., Oyadiji S.O., 2016, Damage detection using modal frequency curve and squared residual wavelet coefficients-based damage indicator, *Mechanical Systems and Signal Processing*, doi: 10.1016/j.ymsp.2016.06.021
- [84] Talebi C., Acar B., Özgen G.O., 2020, Manufacturing Error Detection in Plate and Cylindrical Composite Structures, *IMECE 2020 Proceedings*, doi: 10.1115/IMECE2020-23602



## APPENDICES

### A. Obtaining Natural Frequencies for Composite Structures

To obtain natural frequencies of composite materials, many different analytical, semi-analytical, and numerical methods are present in literature. Therefore, these existing methods can be applied to establish the relationship between natural frequencies and  $D^*$  parameters, so that the optimization process can be realized. In the following section modelling strategies to obtain natural frequencies for different geometries and their constraints are given.

#### A.1 Analytical Modelling

For long, symmetrical plates, the natural frequencies are calculated analytically [70]. Generally, it is described as:

$$\omega_n = \sqrt{\frac{D_{11} \mu^2}{\rho L^2}} \quad (\text{A.1})$$

Where  $\rho$  is the density of the composite laminate,  $L$  is the length of the longer edge, and  $\mu$  is a constant that depends on the boundary conditions on the plate.

Therefore, equation (A.1) describes a beam type structure that does not have any bending-extension coupling. For general rectangular plates this equation fails. In case of rectangular plates, only simply supported boundary conditions on all ends of the plate are given, described by:

$$\omega_n = 2 \sqrt{\frac{\lambda_{ij}}{\rho L_x L_y}} \quad (\text{A.2})$$

$$\lambda_{ij} = \frac{L_x L_y \pi^4}{4} \left[ D_{11} \left( \frac{i}{L_x} \right)^4 + 2(D_{12} + 2D_{66}) \left( \frac{i}{L_x} \right)^2 \left( \frac{j}{L_y} \right)^2 + D_{22} \left( \frac{j}{L_y} \right)^4 \right] \quad (\text{A.3})$$

Where  $L_x$  and  $L_y$  are the edge lengths of the plate in two directions  $x$  and  $y$ ,  $i$  and  $j$  are the number of half waves occurring for the mode shape  $i, j$ .

Due to their limitations, these analytical models cannot be applied to complex geometries or other boundary conditions. Therefore, other methods must be considered to eliminate these limitations.

## A.2 Continuous System Modelling

In most general sense, the total strain energy and kinetic energy stored in the composite laminate undergoing any deformation can be shown as:

$$SE = \frac{1}{2} \int (\{\varepsilon_0\}^T [A] \{\varepsilon_0\} + \{\kappa\}^T [B] \{\varepsilon_0\} + \{\varepsilon_0\}^T [B] \{\kappa\} + \{\kappa\}^T [D] \{\kappa\}) dV \quad (\text{A.4})$$

$$KE = \frac{1}{2} \int \rho (\{\ddot{u}\}^T \{\ddot{u}\}) dV \quad (\text{A.5})$$

Where  $SE$  is the total strain energy,  $KE$  is the total kinetic energy, and  $\{\ddot{u}\}$  is the vector containing second order time derivatives of the displacements, which are accelerations.

Nominal strains and curvatures shown on equations (A.4) and (A.5) must be defined as derivatives of displacements with respect to a coordinate system. A general form of the displacement vector can be assumed as:

$$\{\bar{u}\} = \begin{Bmatrix} u \\ v \\ w \end{Bmatrix} = \begin{Bmatrix} \sum_{i=0} \sum_{j=0} U_{ij} \phi_i \varphi_j \sin \omega t \\ \sum_{i=0} \sum_{j=0} V_{kl} \phi_k \varphi_l \sin \omega t \\ \sum_{i=0} \sum_{j=0} W_{mn} \phi_m \varphi_n \sin \omega t \end{Bmatrix} \quad (\text{A.6})$$

Where  $\phi$  and  $\varphi$  are functions satisfying the kinematic boundary conditions,  $U_{ij}$ ,  $V_{kl}$ , and  $W_{mn}$  are unknown arbitrary constants,  $u$ ,  $v$ , and  $w$  are displacements in  $x$ ,  $y$ , and  $z$  directions. These directions are shown in Figure 3.2.

Generally, for the functions satisfying the kinematic boundary conditions, Legendre polynomial functions may be used [77].

$$\phi_i = \xi^i (\xi + 1)^{E1} (\xi - 1)^{E2} \quad (\text{A.7})$$

$$\varphi_j = \eta^j (\eta + 1)^{E3} (\eta - 1)^{E4} \quad (\text{A.8})$$

Where  $\xi$  and  $\eta$  are dimensionless coordinates on in-plane directions of the laminate, obtaining values between -1 and 1 to describe the laminate edge to opposite edge.  $E1$ ,  $E2$ ,  $E3$ , and  $E4$  are selected to satisfy the kinematic boundary conditions of the structure accordingly.

Then, Rayleigh-Ritz method may be applied using equations (A.4 – A.6), defining:

$$\frac{\partial(KE_{max} - SE_{max})}{\partial U_{ij}} = \frac{\partial(KE_{max} - SE_{max})}{\partial V_{kl}} = \frac{\partial(KE_{max} - SE_{max})}{\partial W_{mn}} = 0 \quad (\text{A.9})$$

Where  $KE_{max}$  and  $SE_{max}$  are the maximum values of kinetic and strain energies for the structure.

Equation (A.9) will yield a set of equations that can be used for eigenvalue extraction to obtain the natural frequencies of the structure.

In the next two sections, application of the Rayleigh-Ritz method to plate and cylindrical structure types are presented.

### A.2.1 Continuous System Modelling of Plates

For plates, it can be assumed that strain energy mainly occurs due to the displacement out of plane to the laminate. This significantly simplifies the stress and strain energies to

$$SE = \frac{1}{2} \int \{\kappa\}^T [D^*] \{\kappa\} dV \quad (\text{A.10})$$

$$KE = \frac{1}{2} \int \rho h_{tot} \dot{w}^2 dA \quad (\text{A.11})$$

Where  $h_{tot}$  is the total thickness of the laminate, and  $dA$  implies integration over surface area of the laminate. The curvatures can be defined as

$$\kappa_{xx} = -w_{,xx} \quad (A.12)$$

$$\kappa_{yy} = -w_{,yy} \quad (A.13)$$

$$\kappa_{xy} = -2w_{,xy} \quad (A.14)$$

Where comma denotes differentiation with respect to variable.

Similarly, equation (A.6) will reduce to a single dimension as shown

$$w = \sum_{i=0} \sum_{j=0} W_{ij} \phi_i \varphi_j \sin \omega t \quad (A.15)$$

Using equations (A.9 – A.15) one can define the stiffness and mass tensors as follows

$$\begin{aligned} K_{ijmn} = & \frac{1}{2} \int_0^{L_y} \int_0^{L_x} \{ D_{11}^* \phi_{i,xx} \varphi_j \phi_{m,xx} \varphi_n + D_{22}^* \phi_i \varphi_{j,yy} \phi_m \varphi_{n,yy} \\ & + 4D_{66}^* \phi_{i,x} \varphi_{j,y} \phi_{m,x} \varphi_{n,y} \\ & + D_{12}^* (\phi_{i,xx} \varphi_j \phi_m \varphi_{n,yy} + \phi_i \varphi_{j,yy} \phi_{m,xx} \varphi_n) \\ & + 2D_{16}^* (\phi_{i,xx} \varphi_j \phi_{m,x} \varphi_{n,y} + \phi_{i,x} \varphi_{j,y} \phi_{m,xx} \varphi_n) \\ & + 2D_{26}^* (\phi_i \varphi_{j,yy} \phi_{m,x} \varphi_{n,y} + \phi_{i,x} \varphi_{j,y} \phi_m \varphi_{n,yy}) \} dx dy \end{aligned} \quad (A.16)$$

$$M_{ijmn} = \frac{1}{2} \int_0^{L_y} \int_0^{L_x} \{ \rho h_{tot} \phi_i \varphi_j \phi_m \varphi_n \} dx dy \quad (A.17)$$

However, to solve the eigenvalue problem for the defined stiffness and mass matrices, they must be reduced from 4<sup>th</sup> order to 2<sup>nd</sup> order. This can be done by a change of indices defined by

$$q_1 = (i - 1)N_j + j \quad (A.18)$$

$$q_2 = (m - 1)N_n + n \quad (A.19)$$

Where  $N_j$  and  $N_n$  are the total number of elements considered for  $j$  and  $n$  indices.

Then, equations (A.16) and (A.17) can be reduced to 2<sup>nd</sup> order matrices using equations (A.18) and (A.19) as shown in Figure A.1.

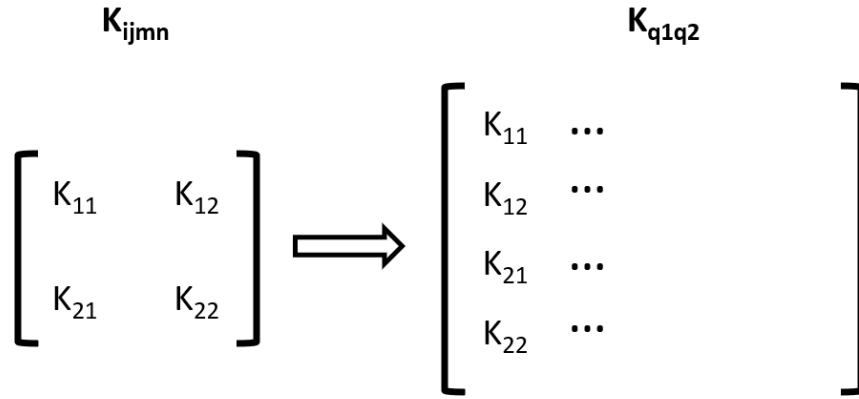


Figure A.1 Reduction of the 4<sup>th</sup> order matrix to 2<sup>nd</sup> order

In Figure A.1, the example is shown for a constant  $m$  and  $n$  index where the elements of  $i$  and  $j$  indices at these specific  $m$  and  $n$  index are shown. Therefore, this process must be repeated for all  $m$  and  $n$  indices. Once second order tensors for stiffness and mass are constructed, natural frequencies can be solved by the eigenvalue problem described below.

$$[K] - \omega_n^2[M] = \{0\} \quad (\text{A.20})$$

### A.2.2 Continuous System Modelling of Cylinders

Unlike plates, equations for cylindrical structures cannot be simplified thoroughly. Therefore, all three coordinates must be used for the equations. This means, energy equations given in (A.4) and (A.5) cannot be simplified further. Therefore, all nominal strains and curvatures have to be defined. Considering Figure A.2, these strains and curvatures can be defined as

$$\varepsilon_{0xx} = u_{,x} \quad (\text{A.21})$$

$$\varepsilon_{0yy} = \frac{1}{R}(v_{,\theta} + w) \quad (\text{A.22})$$

$$\varepsilon_{0xy} = \frac{1}{R}u_{,\theta} + v_{,x} \quad (\text{A.23})$$

$$\kappa_{xx} = -w_{,xx} \quad (\text{A.24})$$

$$\kappa_{yy} = -\frac{1}{R^2}(w_{,\theta\theta} - v_{,\theta}) \quad (\text{A.25})$$

$$\kappa_{xy} = -\frac{1}{R}(2w_{,x\theta} - v_{,x}) \quad (\text{A.26})$$

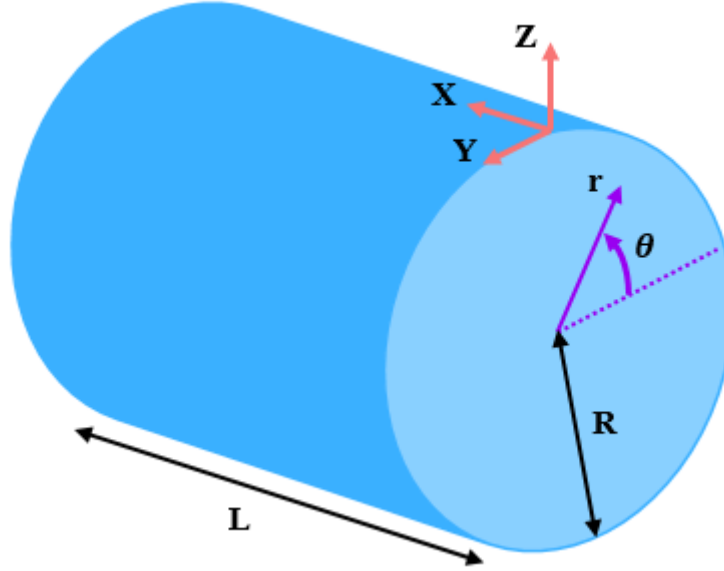


Figure A.2 Coordinate systems used for the cylinder and general dimensions of the cylinder

Therefore, combining equations (A.4 – A.6), one can define the set of equilibrium equations given below.

$$N_{xx,x} + \frac{1}{R}N_{xy,\theta} = \rho h_{tot}\ddot{u} \quad (\text{A.27})$$

$$\frac{1}{R}N_{yy,\theta} + N_{xy,x} - \frac{1}{R^2}M_{yy,\theta} + M_{xy,x} = \rho h_{tot}\ddot{v} \quad (\text{A.28})$$

$$M_{xx,xx} - \frac{2}{R}M_{xy,x\theta} + \frac{1}{R^2}M_{yy,\theta\theta} + N_{yy} = \rho h_{tot}\ddot{w} \quad (\text{A.29})$$

Where  $N$  and  $M$  were defined previously as the section forces and moments in equation (3.13).

Using equation (3.13) and equations (A.21 – A.26) one can define the forces and moment as:

$$N_x = A_{11}u_{,x} + \frac{A_{12}}{R}(v_{,\theta} + w) + A_{16}\left(\frac{1}{R}u_{,\theta} + v_{,x}\right) - B_{11}w_{,xx} - \frac{B_{12}}{R^2}(w_{,\theta\theta} - v_{,\theta}) - \frac{B_{16}}{R}(2w_{,x\theta} - v_{,x}) \quad (\text{A.30})$$

$$N_y = A_{12}u_{,x} + \frac{A_{22}}{R}(v_{,\theta} + w) + A_{26}\left(\frac{1}{R}u_{,\theta} + v_{,x}\right) - B_{12}w_{,xx} - \frac{B_{22}}{R^2}(w_{,\theta\theta} - v_{,\theta}) - \frac{B_{26}}{R}(2w_{,x\theta} - v_{,x}) \quad (\text{A.31})$$

$$N_{xy} = A_{16}u_{,x} + \frac{A_{26}}{R}(v_{,\theta} + w) + A_{66}\left(\frac{1}{R}u_{,\theta} + v_{,x}\right) - B_{16}w_{,xx} - \frac{B_{26}}{R^2}(w_{,\theta\theta} - v_{,\theta}) - \frac{B_{66}}{R}(2w_{,x\theta} - v_{,x}) \quad (\text{A.32})$$

$$M_x = B_{11}u_{,x} + \frac{B_{12}}{R}(v_{,\theta} + w) + B_{16}\left(\frac{1}{R}u_{,\theta} + v_{,x}\right) - D_{11}w_{,xx} - \frac{D_{12}}{R^2}(w_{,\theta\theta} - v_{,\theta}) - \frac{D_{16}}{R}(2w_{,x\theta} - v_{,x}) \quad (\text{A.33})$$

$$M_y = B_{12}u_{,x} + \frac{B_{22}}{R}(v_{,\theta} + w) + B_{26}\left(\frac{1}{R}u_{,\theta} + v_{,x}\right) - D_{12}w_{,xx} - \frac{D_{22}}{R^2}(w_{,\theta\theta} - v_{,\theta}) - \frac{D_{26}}{R}(2w_{,x\theta} - v_{,x}) \quad (\text{A.34})$$

$$M_{xy} = B_{16}u_{,x} + \frac{B_{26}}{R}(v_{,\theta} + w) + B_{66}\left(\frac{1}{R}u_{,\theta} + v_{,x}\right) - D_{16}w_{,xx} - \frac{D_{26}}{R^2}(w_{,\theta\theta} - v_{,\theta}) - \frac{D_{66}}{R}(2w_{,x\theta} - v_{,x}) \quad (\text{A.35})$$

Substituting equations (A.30 – A.35) into equations (A.27 – A.29), we obtain the following system of equations

$$\left( \begin{bmatrix} U1 & U2 & U3 \\ V1 & V2 & V3 \\ W1 & W2 & W3 \end{bmatrix} + \omega^2 \rho h_{tot} [I] \right) \begin{Bmatrix} u \\ v \\ w \end{Bmatrix} = \begin{Bmatrix} 0 \\ 0 \\ 0 \end{Bmatrix} \quad (\text{A.36})$$

Where  $[I]$  is the unit matrix of size 3x3. The differential operators in shown in equation (A.36) can be defined as:

$$U1 = A_{11} \frac{\partial^2}{\partial x^2} + \frac{2}{R} A_{16} \frac{\partial^2}{\partial x \partial \theta} + \frac{1}{R^2} A_{66} \frac{\partial^2}{\partial \theta^2} \quad (\text{A.37})$$

$$U2 = \left( A_{16} + \frac{1}{R} B_{16} \right) \frac{\partial^2}{\partial x^2} + \frac{1}{R} \left[ A_{12} + A_{66} + \frac{1}{R} (B_{12} + B_{66}) \right] \frac{\partial^2}{\partial x \partial \theta} + \frac{1}{R^2} (A_{26} + \frac{1}{R} B_{26}) \frac{\partial^2}{\partial \theta^2} \quad (\text{A.38})$$

$$U3 = \frac{1}{R} A_{12} \frac{\partial}{\partial x} + \frac{1}{R^2} A_{26} \frac{\partial}{\partial \theta} - B_{11} \frac{\partial^3}{\partial x^3} - \frac{3}{R} B_{16} \frac{\partial^3}{\partial x^2 \partial \theta} - \frac{1}{R^2} (B_{12} + 2B_{66}) \frac{\partial^3}{\partial x \partial \theta^2} - \frac{1}{R^3} B_{26} \frac{\partial^3}{\partial \theta^3} \quad (\text{A.39})$$

$$V1 = \left( A_{16} + \frac{1}{R} B_{16} \right) \frac{\partial^2}{\partial x^2} + \frac{1}{R} \left[ A_{12} + A_{66} + \frac{1}{R} (B_{12} + B_{66}) \right] \frac{\partial^2}{\partial x \partial \theta} + \frac{1}{R^2} (A_{26} + \frac{1}{R} B_{26}) \frac{\partial^2}{\partial \theta^2} \quad (\text{A.40})$$

$$V2 = \left( A_{66} + \frac{2}{R} B_{66} + \frac{1}{R^2} D_{66} \right) \frac{\partial^2}{\partial x^2} + \frac{2}{R} \left( A_{26} + \frac{2}{R} B_{26} + \frac{1}{R^2} D_{26} \right) \frac{\partial^2}{\partial x \partial \theta} + \frac{1}{R^2} \left( A_{22} + \frac{2}{R} B_{22} + \frac{1}{R^2} D_{22} \right) \frac{\partial^2}{\partial \theta^2} \quad (\text{A.41})$$

$$V3 = \frac{1}{R} \left( A_{26} + \frac{1}{R} B_{26} \right) \frac{\partial}{\partial x} + \frac{1}{R^2} \left( A_{22} + \frac{1}{R} B_{22} \right) \frac{\partial}{\partial \theta} - \left( B_{16} + \frac{1}{R} D_{16} \right) \frac{\partial^3}{\partial x^3} - \frac{1}{R} \left[ B_{12} + 2B_{66} + \frac{1}{R} (D_{12} + 2D_{66}) \right] \frac{\partial^3}{\partial x^2 \partial \theta} - \frac{3}{R^2} \left( B_{26} + \frac{1}{R} D_{26} \right) \frac{\partial^3}{\partial x \partial \theta^2} - \frac{1}{R^3} \left( B_{22} + \frac{1}{R} D_{22} \right) \frac{\partial^3}{\partial \theta^3} \quad (\text{A.42})$$

$$W1 = -\frac{1}{R} A_{12} \frac{\partial}{\partial x} - \frac{1}{R^2} A_{26} \frac{\partial}{\partial \theta} + B_{11} \frac{\partial^3}{\partial x^3} + \frac{3}{R} B_{16} \frac{\partial^3}{\partial x^2 \partial \theta} + \frac{1}{R^2} (2B_{66} + B_{12}) \frac{\partial^3}{\partial x \partial \theta^2} + \frac{1}{R^3} B_{26} \frac{\partial^3}{\partial \theta^3} \quad (\text{A.43})$$



$$\begin{aligned}
W2 = & -\frac{1}{R}\left(A_{26} + \frac{1}{R}B_{26}\right)\frac{\partial}{\partial x} - \frac{1}{R^2}\left(A_{22} + \frac{1}{R}B_{22}\right)\frac{\partial}{\partial \theta} \\
& + \left(B_{16} + \frac{1}{R}D_{16}\right)\frac{\partial^3}{\partial x^3} \\
& + \frac{1}{R}\left[B_{12} + 2B_{66} + \frac{1}{R}(D_{12} + 2D_{66})\right]\frac{\partial^3}{\partial x^2\partial\theta} \\
& + \frac{3}{R^2}\left(B_{26} + \frac{1}{R}D_{26}\right)\frac{\partial^3}{\partial x\partial\theta^2} + \frac{1}{R^3}\left(B_{22} + \frac{1}{R}D_{22}\right)\frac{\partial^3}{\partial\theta^3}
\end{aligned} \tag{A.44}$$

$$\begin{aligned}
W3 = & -\frac{1}{R^2}A_{22} + \frac{2}{R}B_{12}\frac{\partial^2}{\partial x^2} + \frac{4}{R^2}B_{26}\frac{\partial^2}{\partial x\partial\theta} + \frac{2}{R^3}B_{22}\frac{\partial^2}{\partial\theta^2} - D_{11}\frac{\partial^4}{\partial x^4} \\
& - \frac{4}{R}D_{16}\frac{\partial^4}{\partial x^3\partial\theta} - \frac{2}{R^2}(D_{12} + 2D_{66})\frac{\partial^4}{\partial x^2\partial\theta^2} \\
& - \frac{4}{R^3}D_{26}\frac{\partial^4}{\partial x\partial\theta^3} - \frac{1}{R^4}D_{22}\frac{\partial^4}{\partial\theta^4}
\end{aligned} \tag{A.45}$$

Then, the eigenvalue problem presented in (A.36) can be solved with the displacement vectors given in (A.6) to obtain the natural frequencies.

### A.3 Numerical Modelling

Despite the success of previously mentioned methods, they are not applicable for complex geometries such as pressure vessel. Therefore, other methods are necessary to assess parts of complex geometries.

Although many numerical modelling techniques are present, finite element method is the most commercially available and validated one. In this thesis, Abaqus [72] is used to model the structures at hand. In previous sections, calculations for relatively basic geometries such as beams, plates, and cylinders are given, but with finite element method any complex geometry can be analyzed. However, the downside of this method is that while the previous methods might present a calculation time on the order of fraction of a second, it may take several minutes for the finite element method. Hence, it is best to assess basic geometries with other methods instead of directly applying more sophisticated methods.

In later stages of this thesis, finite element models are constructed both as a necessity for the method for complex geometries and for validation of the proposed/employed methods. More information about the modelling process and other related glossary are presented in proper sections. Therefore, a detailed modelling procedure is not presented here.

Using finite element method, natural frequencies can be calculated by modal analysis, just like the objective of previously presented methods to obtain natural frequencies. Since the natural frequencies can be calculated given the material properties, namely  $D^*$  parameters and/or  $[ABD]$  matrix, it is only natural that these properties can be optimized to match the calculated and experimentally obtained natural frequencies.

## B. Numerical Validation Results for Identification of Ply Layup Configuration

In this section, results of the numerical validation for identification of ply layup configuration is presented for various cases. Below are the results divided into categories for geometries considered in this thesis.

### B.1 Numerical Validation Results for Plate Structures

Table B.1 Results of the optimization runs for ply orientation identification for P\_C1\_S2\_B1 case

Optimization Run	Section 1	Section 2	Section 3	Section 4
1	$[\pm 0.8]$	$[\pm 0.7]$	$[\pm 2.2]$	$[\pm 1.6]$
2	$[\pm 1.2]$	$[\pm 3.2]$	$[\pm 0.1]$	$[\pm 0.5]$
3	$[\pm 1.2]$	$[\pm 1.1]$	$[\pm 0.3]$	$[\pm 0.4]$
4	$[\pm 0.2]$	$[\pm 1.0]$	$[\pm 2.5]$	$[\pm 0.2]$
5	$[\pm 0.3]$	$[\pm 1.7]$	$[\pm 1.3]$	$[\pm 1.6]$
Average	$[\pm 0.7]$	$[\pm 1.5]$	$[\pm 1.3]$	$[\pm 0.9]$
Target Layup	$[0]_2$	$[0]_2$	$[0]_2$	$[0]_2$

Table B.2 Results of the optimization runs for ply orientation identification for P\_C1\_S1\_B2 case

Optimization Run	Section 1	Section 2	Section 3	Section 4
1	[±2.1]	[±1.7]	[±0.6]	[±0.4]
2	[±0.3]	[±1.2]	[±0.9]	[±1.5]
3	[±0.7]	[±0.3]	[±3.3]	[±0.1]
4	[±1.5]	[±1.4]	[±2.1]	[±0.7]
5	[0] <sub>2</sub>	[±2.8]	[±1.7]	[±0.6]
Average	[±0.9]	[±1.5]	[±1.7]	[±0.7]
Target Layup	[0] <sub>2</sub>	[0] <sub>2</sub>	[0] <sub>2</sub>	[0] <sub>2</sub>

Table B.3 Results of the optimization runs for ply orientation identification for P\_C2\_S1\_B1 case

Optimization Run	Section 1	Section 2	Section 3	Section 4
1	[±46.1]	[±44.8]	[±45.9]	[±44.7]
2	[±46.2]	[±46.6]	[±43.3]	[±43.9]
3	[±46.9]	[±46.7]	[±45.9]	[±46.3]
4	[±44.6]	[±46.4]	[±43.2]	[±44.4]
5	[±45.8]	[±45.1]	[±43.5]	[±46.4]
Average	[±45.9]	[±45.9]	[±44.4]	[±45.1]
Target Layup	[±45]	[±45]	[±45]	[±45]

Table B.4 Results of the optimization runs for ply orientation identification for P\_C3\_S1\_B1 case

Optimization Run	Section 1	Section 2	Section 3
1	[±17.9]	[±71.1]	[±18.2]
2	[±18.6]	[±70.1]	[±22.3]
3	[±14.5]	[±67.9]	[±20.4]
4	[±15.2]	[±68.6]	[±19.8]
5	[±18.7]	[±68.0]	[±20.2]
Average	[±17.0]	[±69.1]	[±20.1]
Target Layup	[±15]	[±75]	[±20]

Table B.5 Results of the optimization runs for ply orientation identification for P\_C4\_S1\_B1 case

Optimization Run	Section 1	Section 2	Section 3
1	[±0.5]	[±45.0]	[±86.5]
2	[±0.5]	[±49.2]	[±84.6]
3	[±0.7]	[±42.8]	[±91.6]
4	[±0.3]	[±40.3]	[±95.0]
5	[±0.8]	[±47.3]	[±90.7]
Average	[±0.6]	[±44.9]	[±89.7]
Target Layup	[0] <sub>2</sub>	[±45]	[90] <sub>2</sub>

Table B.6 Results of the optimization runs for ply orientation identification for P\_C5\_S1\_B1 case

Optimization Run	Section 1	Section 2	Section 3
1	[±21.7]	[±17.6]	[±18.6]
2	[±21.8]	[±15.9]	[±19.6]
3	[±20.0]	[±19.7]	[±20.9]
4	[±21.2]	[±18.2]	[±18.5]
5	[±20.4]	[±19.2]	[±19.9]
Average	[±21.0]	[±18.1]	[±19.9]
Target Layup	[±20]	[±20]	[±20]

Table B.7 Results of the optimization runs for ply orientation identification for P\_C6\_S1\_B1 case

Optimization Run	Section 1	Section 2	Section 3
1	[±25.5]	[±26.2]	[±27.6]
2	[±24.7]	[±23.2]	[±28.9]
3	[±25.9]	[±25.6]	[±27.3]
4	[±24.7]	[±25.9]	[±27.0]
5	[±25.5]	[±25.6]	[±27.6]
Average	[±25.3]	[±25.3]	[±27.7]
Target Layup	[±25]	[±27]	[±28]

Table B.8 Results of the optimization runs for ply orientation identification for P\_C2\_S2\_B2 case

Optimization Run	Section 1	Section 2	Section 3	Section 4
1	[±45.5]	[±43.2]	[±44.2]	[±44.4]
2	[±45.5]	[±46.5]	[±43.5]	[±46.7]
3	[±44.3]	[±43.2]	[±43.6]	[±46.4]
4	[±46.9]	[±44.4]	[±46.2]	[±44.3]
5	[±45.9]	[±44.5]	[±43.3]	[±46.7]
Average	[±45.6]	[±44.4]	[±44.2]	[±45.7]
Target Layup	[±45]	[±45]	[±45]	[±45]

Table B.9 Results of the optimization runs for ply orientation identification for P\_C7\_S2\_B2 case

Optimization Run	Section 1	Section 2	Section 3	Section 4
1	[±46.6]	[±4.9]	[±0.9]	[±44.4]
2	[±44.3]	[±2.8]	[±1.6]	[±45.3]
3	[±44.9]	[±3.0]	[±0.8]	[±46.1]
4	[±43.8]	[±3.4]	[±1.4]	[±45.8]
5	[±45.2]	[±0.4]	[±0.2]	[±46.9]
Average	[±44.9]	[±2.9]	[±1.0]	[±45.7]
Target Layup	[±45]	[0] <sub>2</sub>	[0] <sub>2</sub>	[±45]

Table B.10 Results of the optimization runs for ply orientation identification for P\_C8\_S2\_B2 case

Optimization Run	Section 1	Section 2	Section 3	Section 4
1	[±0.6]	[±42.2]	[±45.8]	[±6.7]
2	[±0.9]	[±42.4]	[±46.6]	[±4.6]
3	[±0.4]	[±44.9]	[±45.5]	[±6.2]
4	[±4.4]	[±47.1]	[±47.8]	[±2.6]
5	[±2.9]	[±45.1]	[±48.7]	[±0.5]
Average	[±1.9]	[±44.3]	[±46.9]	[±4.1]
Target Layup	[0] <sub>2</sub>	[±45]	[±45]	[0] <sub>2</sub>

Table B.11 Results of the optimization runs for ply orientation identification for P\_C9\_S2\_B2 case

Optimization Run	Section 1	Section 2	Section 3	Section 4
1	[±2.7]	[±46.0]	[±0.8]	[±48.3]
2	[±2.7]	[±42.1]	[±0.3]	[±45.4]
3	[±2.8]	[±44.7]	[±0.2]	[±48.8]
4	[±2.4]	[±44.1]	[±0.7]	[±48.9]
5	[±3.8]	[±47.1]	[±0.2]	[±46.3]
Average	[±2.9]	[±44.8]	[±0.4]	[±47.5]
Target Layup	[0] <sub>2</sub>	[±45]	[0] <sub>2</sub>	[±45]



## B.2 Numerical Validation Results for Pressure Vessel Structures

Table B.12 Results of the optimization runs for ply orientation identification for PV\_C13\_S4\_B2 case

Optimization Run	Section 1	Section 2	Section 3
1	[±42.1]	[87.4]	[±37.3]
2	[±38.5]	[93.5]	[±43.4]
3	[±46.4]	[85.6]	[±42.6]
4	[±37.0]	[90.5]	[±38.8]
5	[±37.8]	[91.2]	[±38.7]
Average	[±40.4]	[89.6]	[±40.2]
Target Layup	[±40]	[90]	[±40]

Table B.13 Results of the optimization runs for ply orientation identification for PV\_C14\_S4\_B2 case

Optimization Run	Section 1	Section 2	Section 3
1	[±43.7]	[±42.7]	[89.1]
2	[±45.2]	[±39.5]	[90.5]
3	[±43.5]	[±39.2]	[85.2]
4	[±43.9]	[±44.0]	[85.6]
5	[±37.8]	[±37.3]	[87.3]
Average	[±42.8]	[±40.5]	[87.5]
Target Layup	[±40]	[±40]	[90]

### C. Experimentally Obtained FRFs Through Impact Hammer Modal Tests

In this appendix, sample FRFs (Accelerance) obtained through modal test for various cases are presented. In all presented FRFs, only the magnitude is presented, i.e. not real or complex parts. All FRFs obtained throughout this work are similar, and are not used extensively by any means for the content of the thesis except for the fact of obtaining resonance frequencies. For a plate geometry, a sample point FRF is presented in Figure C.1.

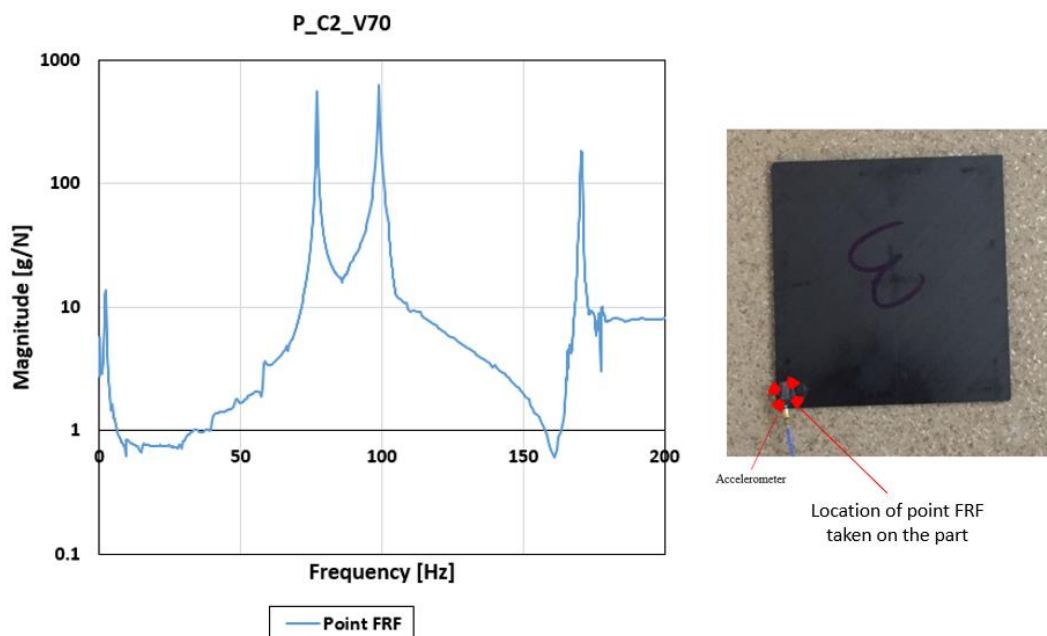


Figure C.1 Point Accelerance taken from P\_C2\_V70, on the corner of the specimen

In Figure C.1, the free body mode of the structure can be seen at around 2 Hz, which is significantly smaller than the first observed resonance frequency, which is 48.6 Hz. However, in the presented FRF, the first resonance frequency cannot be observed, as the point FRF is taken on the part of the structure where a modal line appears for the first mode shape. Hence, the later frequencies are present as peaks.

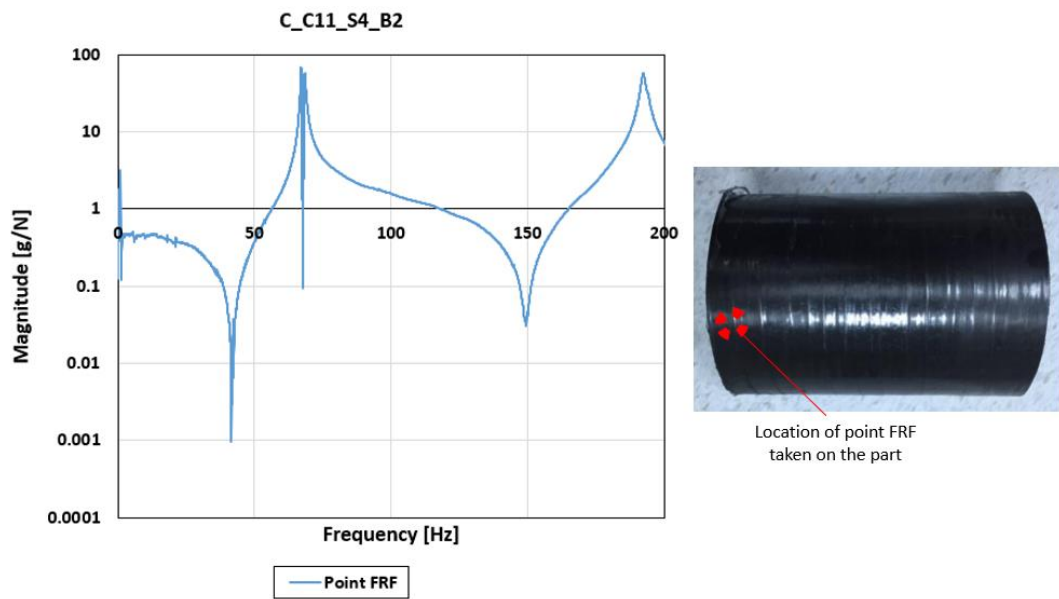


Figure C.2 Point Accelerance taken from C\_C11\_S4\_B2, on the edge of the specimen

In Figure C.2, a point FRF taken from the cylinder is presented. In this figure, the free body modes can be observed around 1 Hz. All resonance frequencies could be identified from this FRF as the point FRF taken on this specimen does not lie on any modal point, line or plane for the first few modes considered in the thesis.

#### D. Numerical Validation Results for Identification of Thickness & Volume Fraction for Plate Structures

In this section, results of the numerical validation for identification of thickness & volume fraction is presented for various cases. Below are the results divided into categories for geometries considered in this thesis.

Table D.14 Pseudo-orientations, volume fraction, and laminate thickness results of the optimization runs for P\_C2\_V60

Optimization Run	Pseudo-orientations	Volume Fraction	Laminate Thickness [mm]
1	$[\pm 50.0/\pm 31.8/\pm 50.3]$	66%	0.89
2	$[\pm 43.3/\pm 39.5/\pm 52.6]$	64%	0.92
3	$[\pm 40.4/\pm 47.9/\pm 39.4]$	57%	1.03
4	$[\pm 35.1/\pm 56.6/\pm 38.6]$	56%	1.05
5	$[\pm 50.0/\pm 40.6/\pm 45.2]$	58%	1.01
Average	$[\pm 43.8/\pm 43.3/\pm 45.2]$	61%	0.98
Target Layup	$[\pm 45]_3$	60%	0.98

Table D.2 Pseudo-orientations, volume fraction, and laminate thickness results of the optimization runs for P\_C3\_V40

Optimization Run	Pseudo-orientations	Volume Fraction	Laminate Thickness [mm]
1	$[\pm 0.1/\pm 61.0/\pm 23.5]$	40%	1.46
2	$[\pm 13.3/\pm 81.3/\pm 20.2]$	43%	1.36
3	$[\pm 4.4/\pm 10.6/\pm 11.4]$	39%	1.50
4	$[\pm 12.4/\pm 82.6/\pm 33.2]$	44%	1.32
5	$[\pm 14.8/\pm 62.3/\pm 26.8]$	47%	1.25
Average	$[\pm 9.8/\pm 59.6/\pm 23.0]$	43%	1.38
Target Layup	$[\pm 15/\pm 70/\pm 20]$	40%	1.46

Table D.3 Pseudo-orientations, volume fraction, and laminate thickness results of the optimization runs for P\_C4\_V70

Optimization Run	Pseudo-orientations	Volume Fraction	Laminate Thickness [mm]
1	[±9.5/±39.9/±62.4]	71%	0.82
2	[±25.2/±55.8/±80.2]	69%	0.84
3	[±8.9/±35.6/±75.2]	66%	0.88
4	[±1.4/±41.5/±102.0]	68%	0.85
5	[±2.1/±31.0/±99.0]	69%	0.84
Average	[±9.4/±40.8/±83.8]	69%	0.85
Target Layup	[0 <sub>2</sub> /±45/90 <sub>2</sub> ]	70%	0.83

Table D.4 Pseudo-orientations, volume fraction, and laminate thickness results of the optimization runs for P\_C5\_V55

Optimization Run	Pseudo-orientations	Volume Fraction	Laminate Thickness [mm]
1	[±20.1/±19.8/±22.9]	57%	1.02
2	[±18.6/±14.8/±14.0]	54%	1.08
3	[±39.4/±7.3/±19.7]	59%	0.99
4	[±19.3/±21.3/±19.4]	54%	1.08
5	[±23.2/±5.9/±17.9]	55%	1.06
Average	[±23.5/±28.9/±21.1]	56%	1.05
Target Layup	[±20] <sub>3</sub>	55%	1.06

Table D.5 Pseudo-orientations, volume fraction, and laminate thickness results of the optimization runs for P\_C6\_V50

Optimization Run	Pseudo-orientations	Volume Fraction	Laminate Thickness [mm]
1	[±31.6/±27.1/±34.0]	50%	1.17
2	[±34.9/±15.3/±32.0]	50%	1.17
3	[±26.5/±31.4/±26.1]	54%	1.08
4	[±22.2/±37.2/±29.1]	51%	1.15
5	[±25.8/±17.9/±28.0]	48%	1.22
Average	[±28.2/±25.8/±29.8]	51%	1.16
Target Layup	[±25/±27/±28]	50%	1.17

Table D.6 Pseudo-orientations, volume fraction, and laminate thickness results of the optimization runs for P\_C2\_V70

Optimization Run	Pseudo-orientations	Volume Fraction	Laminate Thickness [mm]
1	[±48.8/±41.7/±44.7]	67%	0.86
2	[±44.9/±45.1/±44.9]	71%	0.82
3	[±43.5/±31.4/±57.5]	66%	0.88
4	[±35.1/±42.2/±50.3]	70%	0.83
5	[±45.1/±47.0/±43.8]	69%	0.84
Average	[±43.5/±41.5/±48.2]	69%	0.85
Target Layup	[±45] <sub>3</sub>	70%	0.83